Chapter 4

CARPT Experiments

4.1 Operating Conditions

Experiments conducted as part of this study have been performed using air and tap water, under atmospheric conditions. Three columns of internal diameter 14 cm, 19 cm and 44 cm were used to study the effects of column diameter and gas velocity on liquid recirculation, the turbulent stress tensor and the turbulent eddy diffusivities. The data for each CARPT experiment was acquired over a sufficiently large period of time in order to obtain good statistics in each sampling compartment. The duration of each run is given in Table 4.1 along with a summary of the operating conditions of the experiments.

Two types of perforated plate distributors were used in the 14 cm column. The first distributor, referred to as distributor **6A** is similar to the perforated plate distributor used by Hills (1974). The second distributor, **6B**, is similar to that of Menzel et al. (1990), who used hot film anemometer probes to measure the time averaged velocities and the turbulent Reynolds shear stresses in a 15 cm diameter column. The objective of using this distributor is to compare the results from CARPT for the Reynolds shear stress τ_{rz} with the results of Menzel et al. (1990). The different gas superficial velocities for the experiments in the 14 cm diameter column were chosen to correspond with the operating conditions used by Menzel et al. (1990). Specific

Table 4.1: Operating Conditions and Experimental Details

D_c cm	Distr.	U_g cm/s	Static Liqd. Ht. cm	Dynamic Ht. cm	Gas Holdup	Duration of Expt. hr	L_{min} cm	L_{max} cm
14.0	**6A**	2.4	120.2	133.2	0.098	18.0	70.0	115.0
		4.8	98.0	120.4	0.186	18.0	50.0	95.0
		9.6	98.0	126.0	0.222	18.0	50.0	95.0
		12.0(1)	98.0	129.1	0.241	18.0	50.0	95.0
		12.0(2)	98.0	129.5	0.243	18.0	50.0	95.0
14.0	**6B**	2.4	98.0	105.0	0.067	18.0	45.0	80.0
		4.8	98.0	112.0	0.125	18.0	50.0	80.0
		9.6	98.0	123.0	0.203	18.0	50.0	90.0
		12.0	98.0	126.0	0.222	18.0	40.0	90.0
19.0	**8A**	2.0	104.0	114.7	0.093	18.0	80.0	100.0
		5.0	103.5	128.0	0.191	18.0	55.0	95.0
		12.0	95.5	124.0	0.230	18.0	40.0	90.0
	8B	12.0	95.5	118.0	0.191	18.0	50.0	90.0
	8C	12.0	95.5	117.0	0.184	18.0	50.0	90.0
44.0	**18A**	2.0	179.0	193.1	0.073	36.0	115.0	155.0
		5.0	179.0	209.8	0.147	36.0	90.0	160.0
		10.0	176.1	217.6	0.191	36.0	85.0	180.0

details of the distributors are provided in Figure 4.1. Although both the distributors for the 14 cm column are perforated plates, there is a large difference in the open area and hole size between the two distributors. This causes changes in the flow patterns for the two distributors, which will be discussed shortly.

Experiments in the 19 cm diameter column, to study the effect of superficial gas velocity, were conducted using a perforated plate distributor, **8A**, (Figure 4.1) at three superficial gas velocities, in the three flow regimes: the homogeneous bubbly flow regime, the transition regime and the heterogeneous churn-turbulent flow regime. In addition to these experiments, at the highest gas velocity investigated, $U_g = 12$ cm/s (which was the limit due to the existing air compressor during the time of these experiments), experiments were also conducted using a bubble cap sparger and a cone distributor, the details of which are shown in Figure 4.1. The objective of conducting these additional experiments is to study the effects of distributor on bubble sizes, and thereby on liquid recirculation and turbulence in the churn-turbulent flow regime. CARPT results for the mean liquid velocities in the 19 cm diameter column with distributor **8A** have been verified by independently conducting Heat Pulse Anemometer (HPA) experiments.

The 44 cm diameter column is the largest column that can be fitted into the current CARPT/CT experimental setup in CREL. Experiments in this column were conducted at three gas velocities, similar to the case of the 19 cm diameter column, using a perforated plate distributor, **18A**, shown in Figure 4.1.

Column Diameter: 14 cm (6")

Perforated plate distributor **(6A)**

Number of Holes: 61
Size of Holes: 0.4 mm
Layout: 3 concentric circles
1.5 cm apart
Porosity: 0.05 %

Perforated plate distributor **(6B)**

Number of Holes: 121
Size of Holes: 1.0 mm
Layout: 6 concentric circles
0.75 cm apart
Porosity: 0.62 %

Column Diameter: 19 cm (8")

Perforated plate distributor **(8A)**

Number of Holes: 166
Size of Holes: 0.33 mm
Layout: square pitch
of 1.25 cm
Porosity: 0.05 %

Bubble Cap Distributor **(8B)**

Cone Distributor **(8C)**

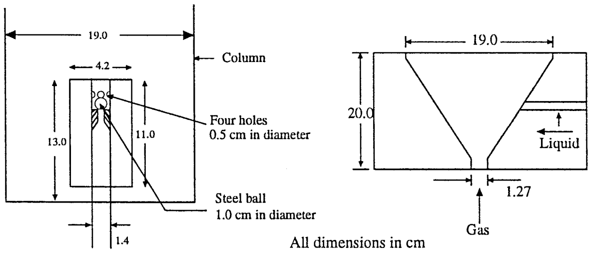

All dimensions in cm

Column Diameter: 44 cm (18")

Perforated plate distributor **(18A)**

Number of Holes: 301
Size of Holes: 0.7 mm
Layout: 14 concentric circles
of 1.5 cm apart
Porosity: 0.077 %

Figure 4.1: Details of Distributors

4.1.1 Distributor Operation Regime

The formation of bubbles at submerged orifices is influenced by many factors, such as the diameter of the orifice, the momentum of the incoming gas, viscosity and surface tension of the liquid, etc. The volume of the gas chamber below the sparger (referred to as the ante-chamber) also has an effect on the bubble formation. When the volume of the gas chamber is small, the so-called constant flow conditions exist at the orifice. When the volume of the chamber is large and the pressure of the inflowing gas is maintained constant (constant pressure condition), as the size of the bubble increases during bubble formation at the orifice, the pressure inside it decreases resulting in a higher flow rate of the gas to the bubble. Therefore, under such circumstances constant flow conditions are not maintained, and the rate of bubble growth varies. However, when the pressure drop across the orifice is very large (presence of very small holes) and the pressure variations occurring during the formation of the bubble are small compared to the total pressure drop, the gas flow rate does not change with bubble formation. To describe the various operating regimes of the distributor Hughes et al. (1955) defined a dimensionless capacitance number, N_c:

$$N_c = \frac{4V_{ch}g\rho_l}{\pi d_o^2 P_o} \tag{4.1}$$

For $N_c > 9$, they identified constant pressure conditions, in which pressure fluctuations exist at the orifice and the volume of the bubble formed depends on N_c. Based on model calculations and experimental data, Tsuge and Hibino (1983) showed that for $9 < N_c < 25$, the bubble volume increases with N_c. However for $N_c > 25$, the bubble volume no longer depends on N_c and thereby the chamber volume.

The dimensionless capacitance number, N_c, for the present operating conditions is always greater than 25 for all the perforated plate distributors considered (**6A**, **6B**, **8A**, **18A**). Therefore under these conditions, there is no effect of chamber volume on the volume of the bubbles formed at the distributor. For the bubble cap sparger and the inverted cone distributor, **8B** and **8C**, constant flow conditions exist due to zero capacitance.

Bubble formation at a single submerged orifice has been subject to extensive theoretical and experimental study by many researchers (Kumar and Kuloor 1970; Tsuge 1986). There are two regimes of bubble production at orifices submerged in a stagnant liquid: a) bubbling regime and b) jetting regime, which determine the size and nature of the bubbles formed. The size of the bubbles formed at the distributor is usually different from the average bubble size in bubble columns, due to coalescence and break-up, especially for high gas velocities. However, the initial bubble size formed can influence the interfacial area and the global gas holdup. The regime of bubbling, therefore, to some extent affects the behavior of the flow in gas-liquid dispersions.

Bubble Regime

The bubble regime is again classified into the single bubble regime and the intermediate bubble regime.

Single Bubble Regime

In the single bubble regime the bubbles are produced one at a time, their size being determined primarily by the orifice diameter, d_o, surface tension of the liquid, σ and the densities of the gas and liquid. The following expression is obtained for diameter of the bubbles, by balancing the buoyancy and surface tension forces:

$$d_b = [\frac{6\sigma d_o}{(\rho_l - \rho_g)g}]^{1/3} \tag{4.2}$$

The bubble size in this regime is independent of gas flow rate. The above equation typically holds for very low gas flow rates, $Re_o \leq 200$, where $Re_o = \rho_l u_o d_o / \mu_l$ is the orifice Reynolds number and u_o is the gas velocity at the orifice. For bubble column operations this regime is not of practical importance, since it applies only for very low superficial gas velocities, much lower than 1 cm/s.

Intermediate Bubble Regime

For higher orifice Reynolds numbers, in the range $200 < Re_o \leq 2200$, the bubble size becomes dependent on the viscous drag and inertial forces, in addition to buoyancy and surface tension. As the gas flow through the submerged orifice increases beyond the single bubble regime, the frequency of bubble formation increases slowly and the bubbles begin to grow in size. Most of the theoretical models used to evaluate the volume of the bubble formed, are based on a two stage spherical bubble growth model (Tsuge 1986). Another approach, which is more recent, has been to model the bubble formation based on a local force balance at the bubble interface using potential flow theory for the liquid. In such models the bubble growth and detachment are determined by calculating the shape of the bubble (which need not be spherical) during its formation (Tan and Harris 1986; Wilkinson 1991). Due to the complexities involved, there exists no closed form expression for the average bubble size in this regime. In this investigation the empirical expression developed by Leibson et al. (1956) is used to estimate the bubble size at the distributor in the intermediate bubble regime, given by

$$d_b = 0.19 d_o^{0.48} Re_o^{0.32} \qquad \text{(cgs units)} \tag{4.3}$$

Results using the above correlation are in agreement with the predictions of Kumar et al. (1976).

Jetting Regime

Further increase in the orifice Reynolds number, $Re_o > 2200$, marks the transition to the jetting regime, when turbulence occurs at the orifice and the gas stream approaches the appearance of a continuous jet. The condition for formation of the gas jet is given as (Wallis 1969):

$$\frac{u_o\sqrt{\rho_g}}{[g\sigma(\rho_l-\rho_g)]^{1/4}} > 3.0[\frac{\sigma}{g(\rho_l-\rho_g)d_o^2}]^{1/2} \qquad (4.4)$$

The above equation agrees well with the Reynolds number based criterion for transition from the bubbling regime to the jetting regime.

Using the above criterion the regime of bubbling for all the experimental conditions is calculated and tabulated in Table 4.2. This enables an estimation of the bubble size at the orifice (after detachment) in the bubbling regime. The calculations are based on the flow rate Q_o through each orifice for a given distributor (total flow rate / number of holes in the distributor). It is seen from Table 4.2 that for a given superficial gas velocity the regime of bubbling is strongly dependent on the distributor used. In the 14 cm diameter column the intermediate bubbling regime appears to persist at all gas velocities for distributor **6B**. For distributor **6A** the bubble formation is in the jetting regime for gas velocities greater than 2.4 cm/s.

Table 4.2: Regime of Bubble Formation for Different Operating Conditions

D_c cm	Distr.	Hole Size cm	Number of Holes	U_g cm/s	Re_o	Regime
14.0	**6A**	0.04	61	2.4	1260	Inter. Bubbling
				4.8	2520	Jetting
				9.6	5040	"
				12.0	6300	"
14.0	**6B**	0.1	121	2.4	258	Inter. Bubbling
				4.8	516	"
				9.6	1032	"
				12.0	1290	"
19.0	8A	0.033	161	2.0	883	Inter. Bubbling
				5.0	2208	"
				12.0	5299	Jetting
	8B	0.5	4	12.0	14514	"
	8C	1.25	1	12.0	22858	"
44.0	**18A**	0.077	301	2.0	1214	Inter. Bubbling
				5.0	3037	Jetting
				10.0	7288	"

The large number of holes in **6B** reduces the volumetric flow rate through each hole for a given superficial gas velocity, and hence lowers the orifice Reynolds number. The lower Reynolds number, implies that the bubble sizes are smaller for this distributor (**6B**). However, the above equations hold only for a single submerged orifice. Distributor **6B** has 121 holes distributed evenly in concentric circles. Therefore, the average spacing of the holes is 1 cm (lower near the center and higher near the wall), which is about half the spacing of distributor **6A**. The higher density of holes for **6B** increases the probability of bubble-bubble interaction at the distributor, possibly leading to coalescence of the bubbles immediately after formation at the orifice. This may explain the significant difference in the observed bubble sizes in this column for the two distributors, **6A** (3 to 5 mm) and **6B** (5 to 7 mm), at a gas velocity of 2.4 cm/s. The bubble sizes estimated using Equation 4.3 are 3.9 mm for **6A** and 3.7 mm for **6B** which do not match the visually observed values. Hence, although the regime of bubbling for distributor **6B**, based on single submerged orifice equations, is in the intermediate regime at all gas velocities (both bubbly flow and churn-turbulent flow regime), this may not reflect directly the influence of the bubbling regime on bubble sizes and fluid dynamics in the column.

The bubble size of 3.1 mm estimated for **8A** at 2 cm/s corresponds with observations. Similarly, the incipient bubble size for the 44 cm diameter column at 2 cm/s superficial gas velocity is estimated to be 5 mm and roughly agrees with observed bubbles near the wall of the column. It is noted that in the bubbly flow regime the presence of trace contaminants in the water, which changes the surface tension, considerably affects the size of the bubbles and thereby the fluid dynamics in the column. Such effects cannot be properly captured by Equation 4.3 and other such correlations for the intermediate bubbling regime.

4.1.2 Global Gas Holdup

Global gas holdup measurements were made in each column prior to the CARPT experiments, by measuring the bed expansion. The results are presented in Figure 4.2.

A difference is noted between the holdups in the 14 cm diameter column using the two different distributors. However, these differences diminish with increase in gas velocity, as is expected. No specific trend of the gas holdup with respect to the different column diameters is seen. This is in general agreement with observations in the literature. Quantitatively, the correlations of Hammer et al. (1984) and Reilly et al. (1986) yield the closest predictions, as shown in Chapter 2.

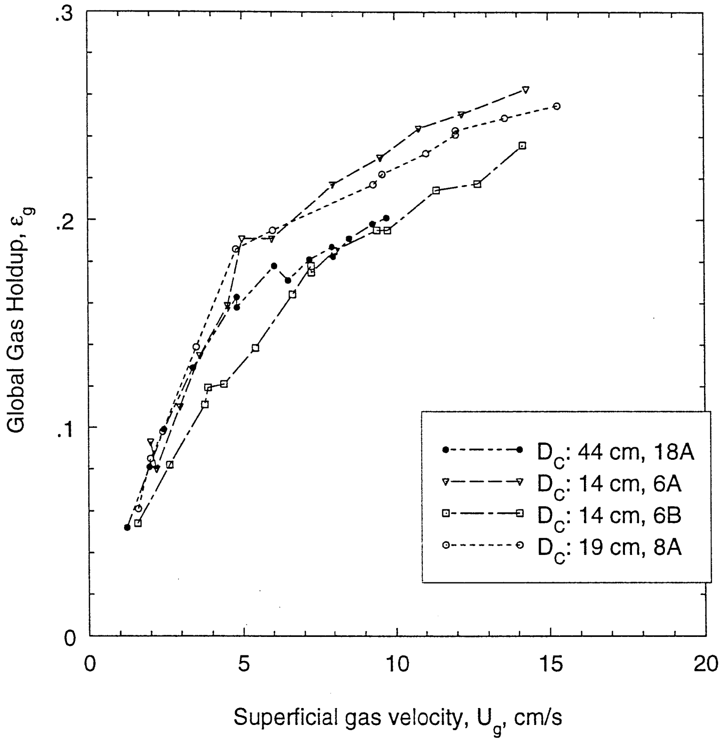

Figure 4.2: Global gas Holdup as a Function of Superficial Gas Velocity in the Different Columns Investigated

A feature that is observed while measuring the global gas holdup is that the gas holdup in the column is sensitive to the static height of the liquid in the column, for a given column diameter. This suggests the axially non-uniform distribution of gas holdup. Kumar (1994) has shown using computed tomography (CT) measurements of the cross-sectional gas holdup distribution, that in the middle section (lengthwise) of the column the gas holdup is uniform. This implies that at the end zones the gas holdup is quite different than in this middle section, and this causes the variation of global holdup measurements with static height. It is expected that for larger column aspect ratios (e.g. greater than 8) this difference becomes small and eventually disappears, since the contribution of the end zones to the overall gas holdup decreases with increase in aspect ratio. In the present study, the L/D ratio was maintained around 7 to 8 for the smaller columns (14 cm and 19 cm) and around 4.5 (due to height limitations in the present CARPT/CT setup) for the 44 cm column.

4.2 3-D Analysis of Time Averaged Flow Pattern and Liquid Velocity Profiles

In this section, CARPT results for the local time averaged liquid velocities, in cylindrical coordinates, are presented as velocity vector plots. Since with the CARPT technique it is possible to measure the time averaged flow pattern in the entire flow field, it is of interest to see if at all there exists a steady axisymmetric flow pattern in a fully three dimensional bubble column.

Based on the discussion in Chapter 3, the optimum manner of discretization of the column for interpretation of CARPT data is by method 'C' shown in Figure 3.8. Such a discretization, by maintaining an equal division in the radial direction, but by varying the angular divisions with radial location, results in a relatively more uniform distribution of compartment volumes. However, since this results in non-uniform azimuthal divisions, in order to facilitate the visualization of the results in a three dimensional domain, it is necessary to interpolate the results on a uniform azimuthal grid. The 3-D visualization of the data is performed using the TECPLOT software. Features of the software allow interpolation of the data onto a uniform grid to enable 3-D visualization. Once the data is plotted in a three dimensional domain, the domain is *sliced* with a two dimensional plane at different orientations and plotted as vector plots for the time averaged liquid velocities, in order to interpret the 3-D results. Longitudinal (vertical) sections and lateral (cross) sections are made to interpret all the three components of the velocity vectors. The longitudinal sections are made through the center of the column at four angles, 0-180, 90-270, 45-225 and

135-315. The resulting vector plots show the corresponding r and z components of the velocities, projected onto the slicing plane. The θ and r component of the velocity can be visualized from the cross-sectional *slices* made at several selected axial locations in the flow domain, depending on the individual case. The vector plots in the chosen longitudinal sections and cross-sections are shown in Figures 4.3 to 4.34 for all the experimental conditions investigated.

An analysis of the results with respect to the behavior of the time averaged flow pattern for the three column diameters and different distributors studied follows.

4.2.1 Flow Pattern in the 14 cm column

The results for the perforated plate distributor, **6A**, are considered first. Figures 4.3 and 4.4 show the longitudinal sections and cross-sections of the time averaged velocity vector plots at $U_g = 2.4$ cm/s, the lowest gas velocity investigated, in a 14 cm diameter column. From a height of about 50 cm the flow appears to be quite well developed with negligible radial and angular velocities (Figure 4.4 (c)). The flow pattern is also reasonably symmetric with respect to the column axis, although in Figures 4.3 (a) and (c) the downward velocities on one side of the wall are larger in magnitude. The reason for this is discussed shortly. However, this difference decreases with increase in axial position and from about 90 cm (axial position) the flow pattern looks symmetric about the axis with negligible angular and radial velocities, typically less than 1 cm/s (Figure 4.4 (c)). At the upper end of the column, near the disengagement zone, the flow reversal is symmetric about the column axis (Figure 4.4 (d)), resembling a fountain like pattern. Spanning the entire column is a single circulation cell, as observed by Devanathan (1991). At the bottom end of the column, close to the distributor, the time averaged flow pattern (circulation cell) is distorted and loses its axisymmetric appearance. In this region the liquid descends predominantly along one side of the column wall and rises along the opposite end. This can be seen in Figure 4.3 and Figure 4.4 (a) and (b), which are at an axial level of 5 cm and 20 cm, respectively.

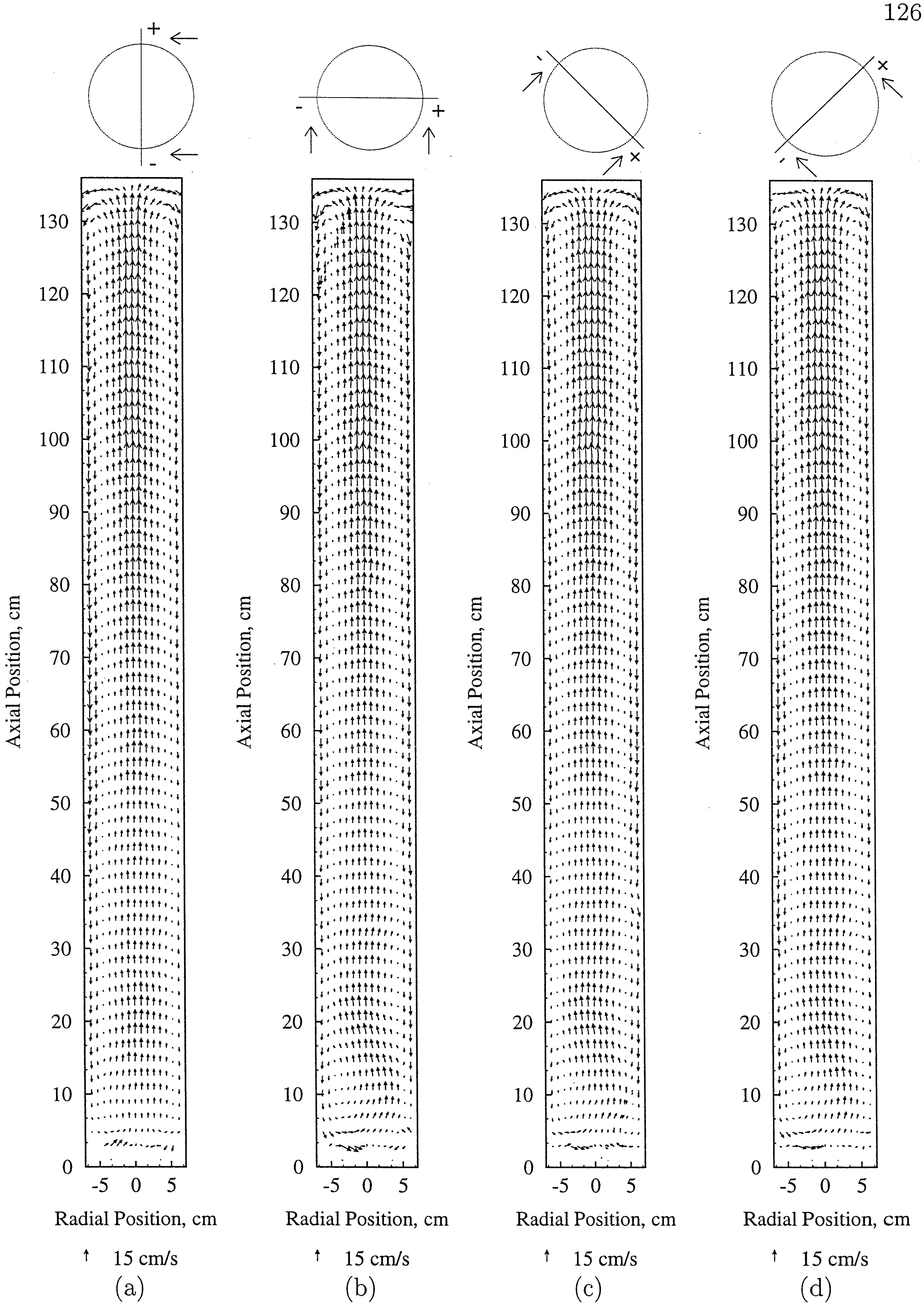

Figure 4.3: Velocity Vector Plots (Longitudinal Views) for Column Diameter 14 cm, Distributor: Perforated Plate **6A**, $U_g = 2.4$ cm/s

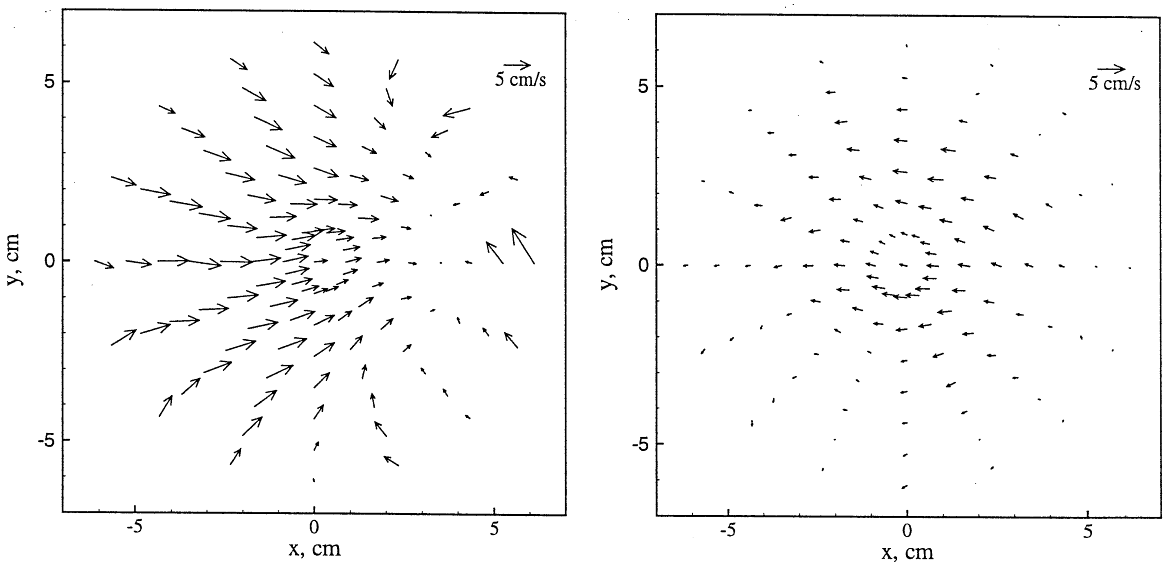

(a) z = 5 cm (b) z = 20 cm

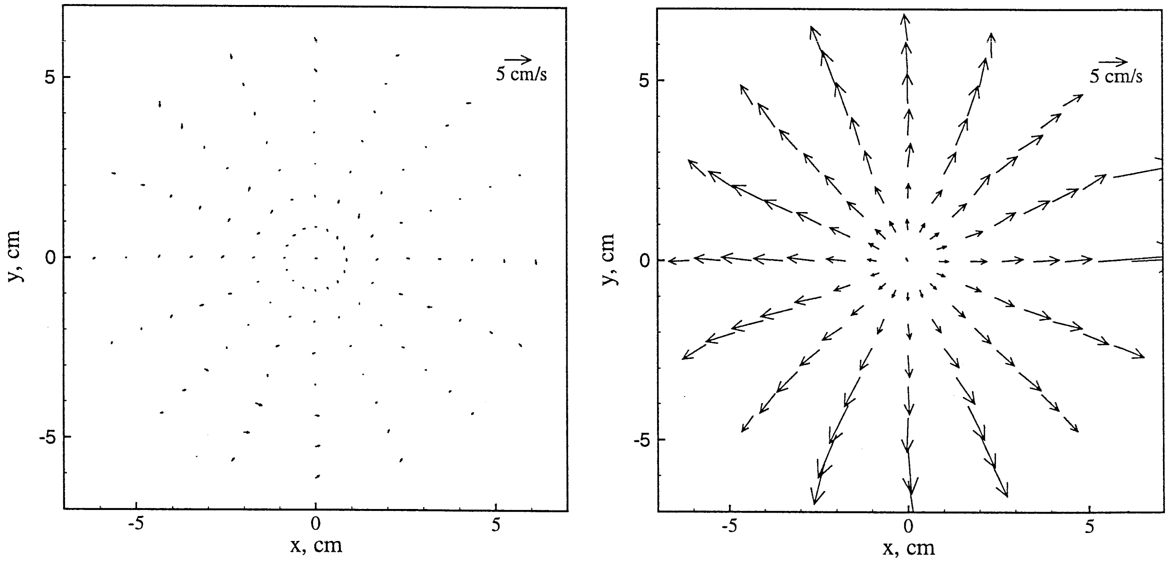

(c) z = 80 cm (d) z = 132 cm

Figure 4.4: Velocity Vector Plots (Cross-sectional Views) for Column Diameter 14 cm, Distributor: Perforated Plate (**6A**), $U_g = 2.4$ cm/s

The time averaged flow in this region forms a 'sheet' like structure that folds at the corners between the column wall and the distributor. Figures 4.4 (a) and (b) indicate that there is no vortical motion (swirl) of the liquid in this region. In other words, the time averaged flow has a two dimensional rather than a three dimensional character, with no rotational movement. Hence the above reference to a "sheet' like structure'. The liquid that rises initially at the wall on one side of the column, progressively makes its way to the center of the column. As a result, what appears as a symmetric structure, with respect to the column axis, in the middle and upper end of the column, becomes skewed near the distributor. It is important to remember that this asymmetric sheet like structure exists in the long time averaged sense and does not represent an instantaneous flow field. This implies that in the time averaged sense, there is a preferred direction for the flow near the distributor, which is not symmetric with respect to the column axis.

Visual observation of the flow in the column indicates the presence of uniform bubbles ranging between 3 to 5 mm in size, at the lowest gas velocity of 2.4 cm/s. Calculation of an initial bubble size using Equation 4.3 yields an average bubble diameter of 3.9 mm at the distributor. Although the gas bubbles appear to flow uniformly through all the holes of the distributor, the gas bubbles tend to form 'swarms' which follow a spiraling motion moving (or rocking) from one side of the wall to the other and gradually seem to get more evenly distributed at higher levels in the column. In the intermediate bubbling regime the inlet kinetic energy of the bubbles at the orifice is consumed in overcoming the surface tension and drag forces during bubble formation (Azbel 1981). Ideally, in a stagnant liquid column, the bubble formed at the orifice detaches and rises at its rise velocity. However, in bubble columns strong liquid currents prevail due to liquid recirculation and turbulence. Hence, the bubble as it detaches from the orifice is swept about by the liquid currents at the distributor. Even though the spiraling motion does not visually appear to have any preferential direction, it is possible that in a statistical sense, there is indeed a preference which is dictated by some non-uniformity in the distributor, e.g., blocking of some of the holes (0.4 mm in diameter for the present case). Permanent blocking of some holes is caused by chemical deposition due to contaminants present in the water. Therefore a perfectly uniformly aerated perforated plate distributor could not be achieved. However, it must be noted that the blocked holes were not concentrated in one area but were dispersed over the entire distributor plate. This strong asymmetry of the time averaged flow pattern near the distributor influences the flow behavior above the distributor zone, leading to large downward velocities near one side of the column, where the liquid flows down towards the distributor. These effects slowly disappear with height and the flow does become axisymmetric toward the upper end of the column.

A similar flow pattern behavior is observed at a gas velocity of 4.8 cm/s (Figures 4.5 and 4.6). The flow pattern in this case becomes well developed and axisymmetric beginning at a lower axial level than for the case of $U_g = 2.4$ cm/s. The asymmetry near the distributor is observed at this gas velocity as well (Figures 4.5 and 4.6). However, the direction of the asymmetry in this case is different from that at a gas velocity of 2.4 cm/s. This means that while the irregularities in the distributor may cause the asymmetry, the actual influence of these imperfections on the distributor affects the flow in different ways at different gas velocities. This asymmetry lasts for a height which is approximately between one to two times the column diameter. Beyond this level the velocities are symmetric with respect to the column axis and a one dimensional flow pattern is established with negligible azimuthal and radial velocities. The large magnitude of some of the vectors at the distributor, in Figure 4.5 (and other such figures, e.g. Figure 4.15), arise due to the poor statistics of the data at that particular compartment location and the higher magnitude of the error in particle location near the distributor, as discussed in Chapter 3. These large vectors near the distributor do not have any particular physical meaning.

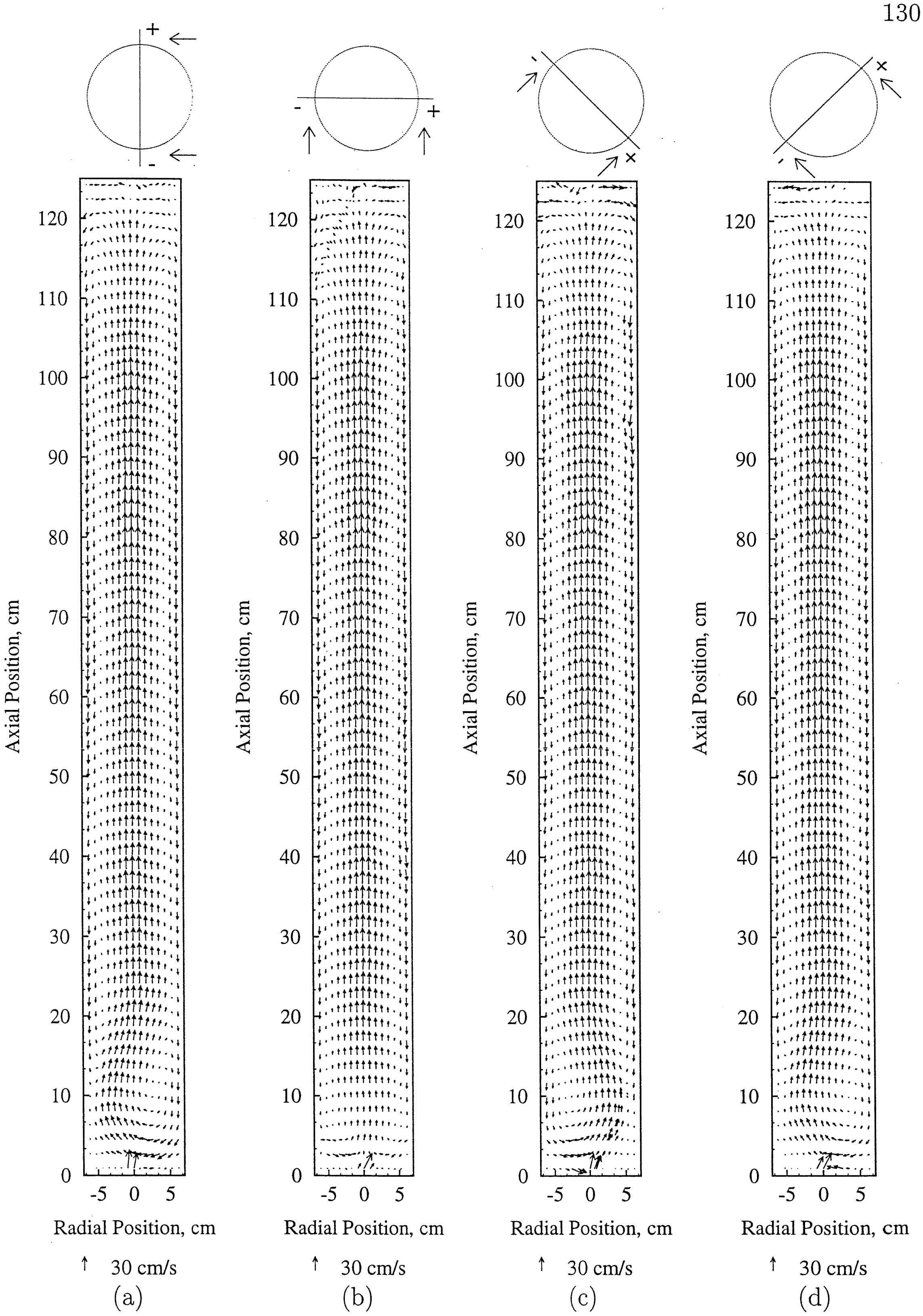

Figure 4.5: Velocity Vector Plots (Longitudinal Views) for Column Diameter 14 cm, Distributor: Perforated Plate **6A**, $U_g = 4.8$ cm/s

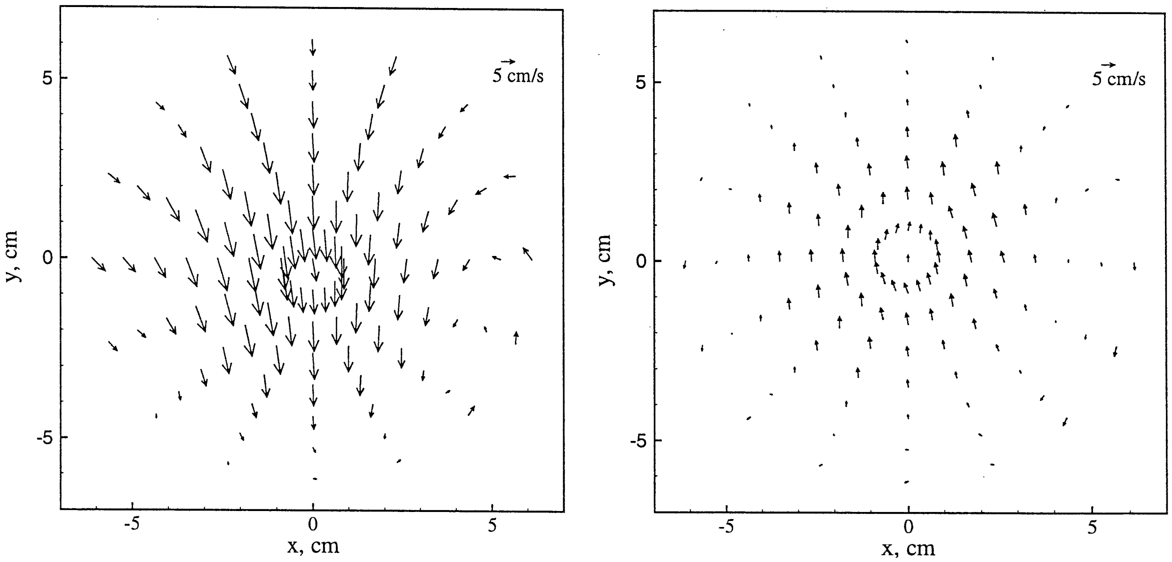

(a) z = 5 cm

(b) z = 20 cm

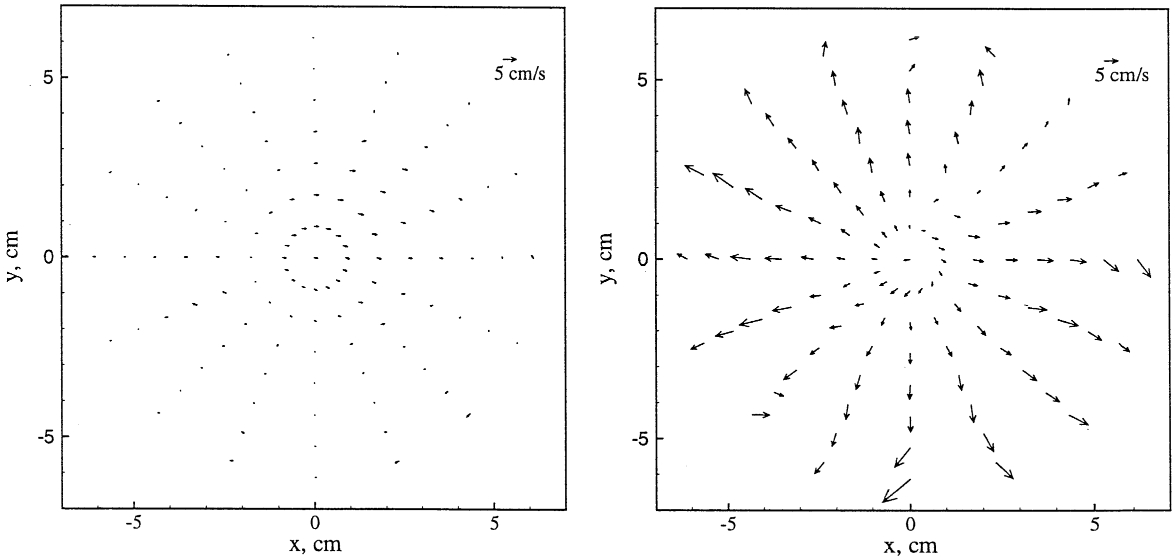

(c) z = 80 cm

(d) z = 120 cm

Figure 4.6: Velocity Vector Plots (Cross-sectional Views) for Column Diameter 14 cm, Distributor: Perforated Plate (**6A**), U_g = 4.8 cm/s

On further increasing the gas velocity, to 9.6 and 12 cm/s, the extent of the asymmetry at the distributor is reduced. The distinct folding of the sheet like structure at the distributor is not observed in Figures 4.7 to 4.10, as in the case of the lower gas velocities. Yet a symmetrical flow pattern, with liquid descending at the walls, progressing toward the center and rising in the center of the column (opposite to that of the disengagement zone) is not observed. Instead, the cross-sectional slice of the vector plot, near the distributor (Figures 4.8 (a) and 4.10 (a)), suggests that the liquid descending along the column wall tends to behave like two sheet like structures (facing each other) that are directed inward near the distributor. The liquid in these structures rises in a manner similar to that of two rollers, squeezing out the liquid in between the rollers. In Figure 4.8 (a), along the x axis, the vectors are all directed toward the center, x=0, while along the y axis (at x=0) the vectors are directed away from the center. This type of flow pattern is seen at both 9.6 and 12 cm/s, with the same directional preference. Other than this asymmetry at the distributor the results for the vector plots confirm that the flow in the middle and upper part of the column is symmetric.

For the experiments using the second distributor, **6B**, in the 14 cm diameter column the distinct asymmetry near the distributor is not observed for any of the gas velocities (Figures 4.11 to 4.18), including the lowest gas velocity of 2.4 cm/s. At U_g = 2.4 cm/s uniform bubbles of 5 to 7 mm exist in the column. The size of these bubbles are larger than the bubbles in the column with distributor **6A**, at U_g = 2.4 cm/s. As described earlier, the bubble sizes predicted (Equation 4.3) are lower than those visually observed, which suggests a possibility of coalescence of the bubbles very close to the distributor, due to the larger number of holes. Due to their larger size (in comparison with those in the column with distributor **6A**) the bubbles have a higher rise velocity. In addition, since the size of the holes are relatively bigger, there were no irregularities in the distributor, caused by blocking of some of the holes.

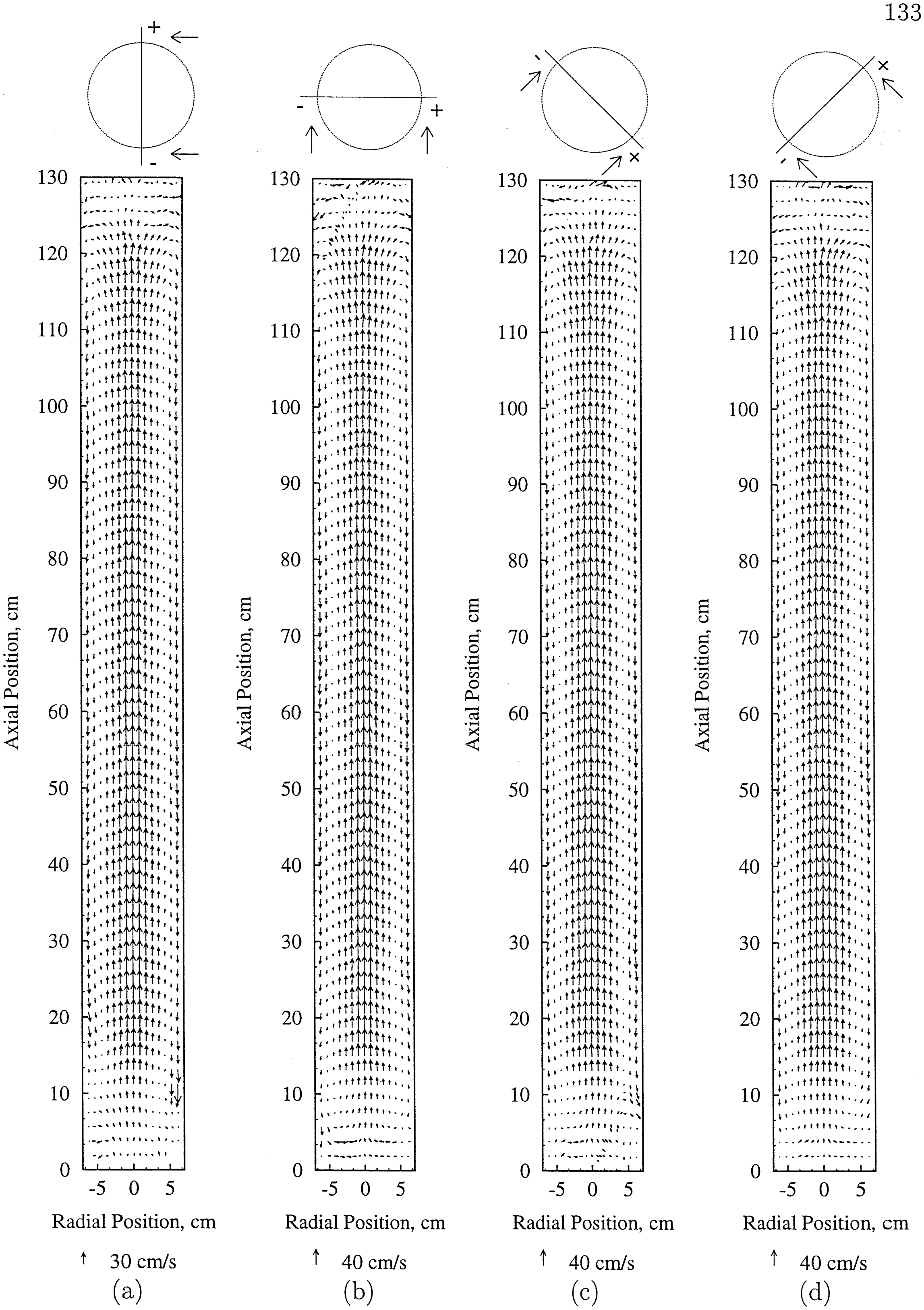

Figure 4.7: Velocity Vector Plots (Longitudinal Views) for Column Diameter 14 cm, Distributor: Perforated Plate **6A**, $U_g = 9.6$ cm/s

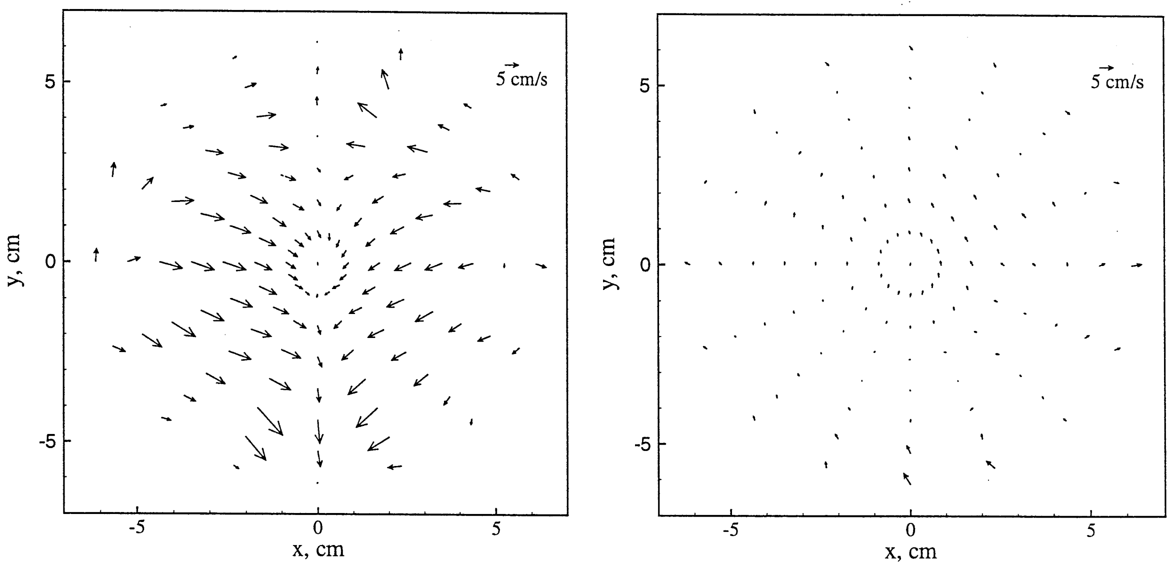

(a) z = 5 cm

(b) z = 20 cm

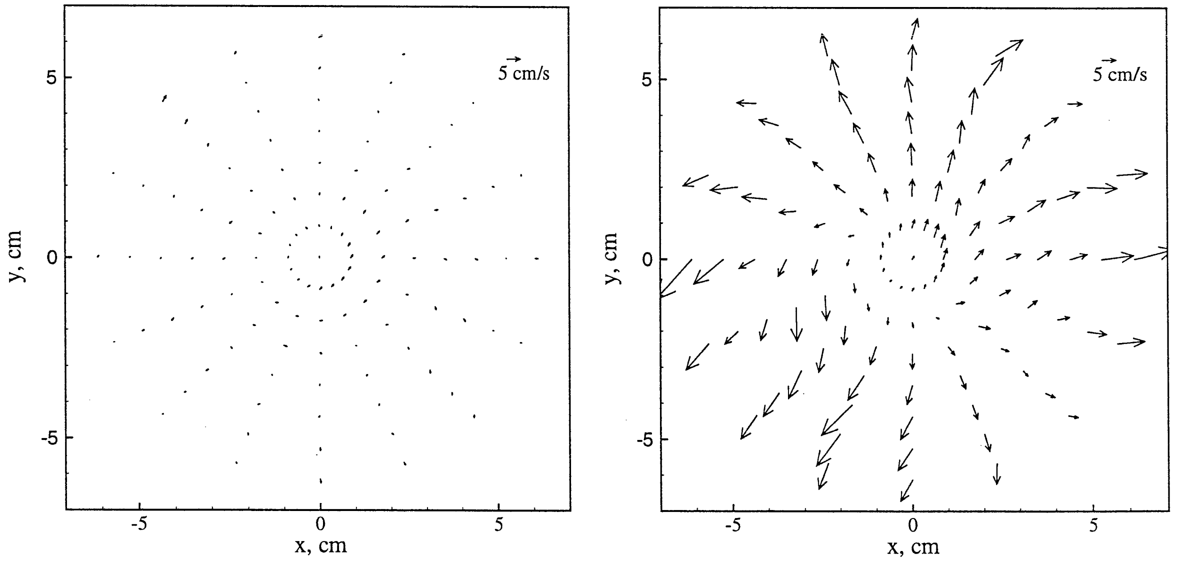

(c) z = 80 cm

(d) z = 125 cm

Figure 4.8: Velocity Vector Plots (Cross-sectional Views) for Column Diameter 14 cm, Distributor: Perforated Plate (**6A**), $U_g = 9.6$ cm/s

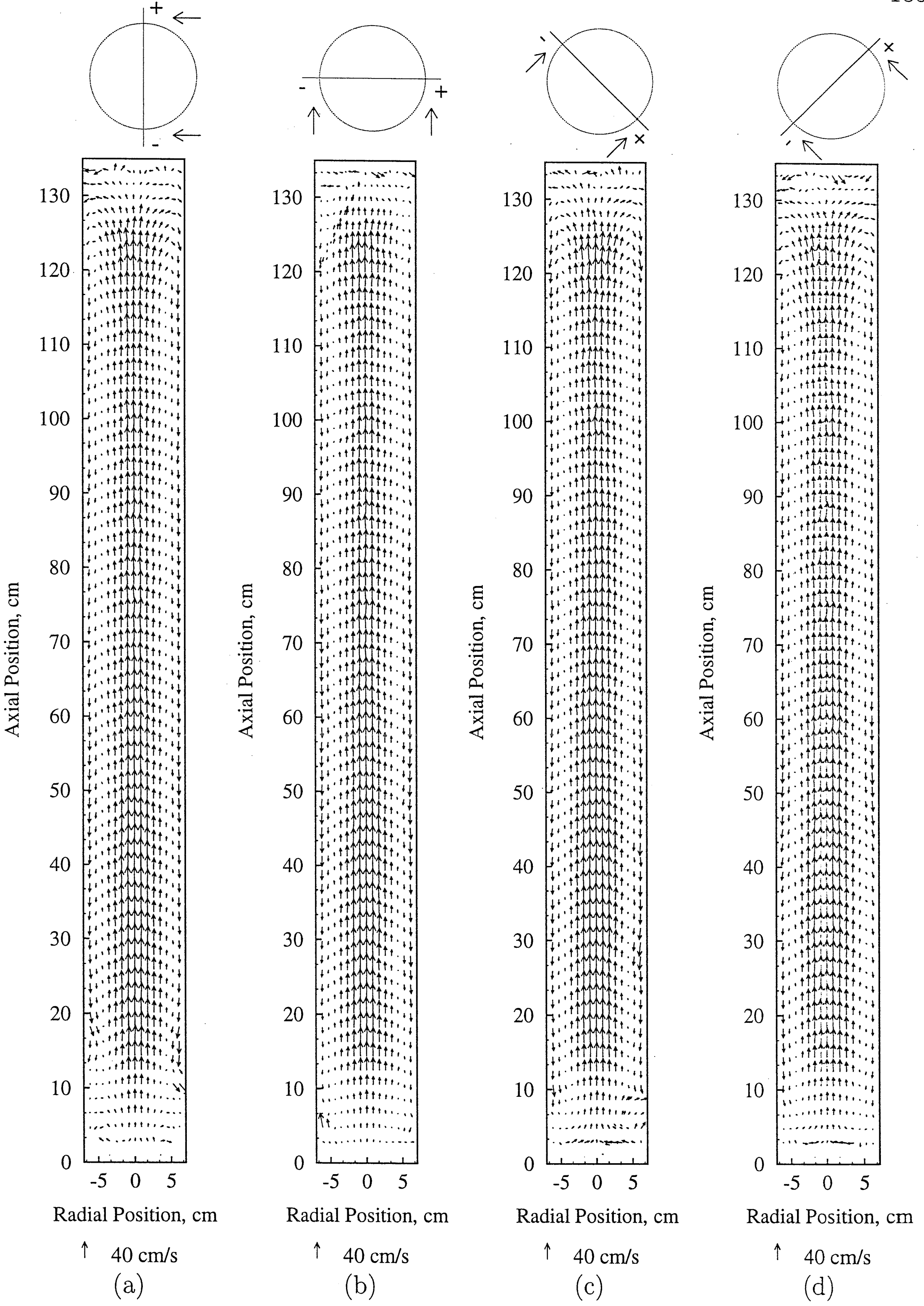

Figure 4.9: Velocity Vector Plots (Longitudinal Views) for Column Diameter 14 cm, Distributor: Perforated Plate **6A**, $U_g = 12.0$ cm/s

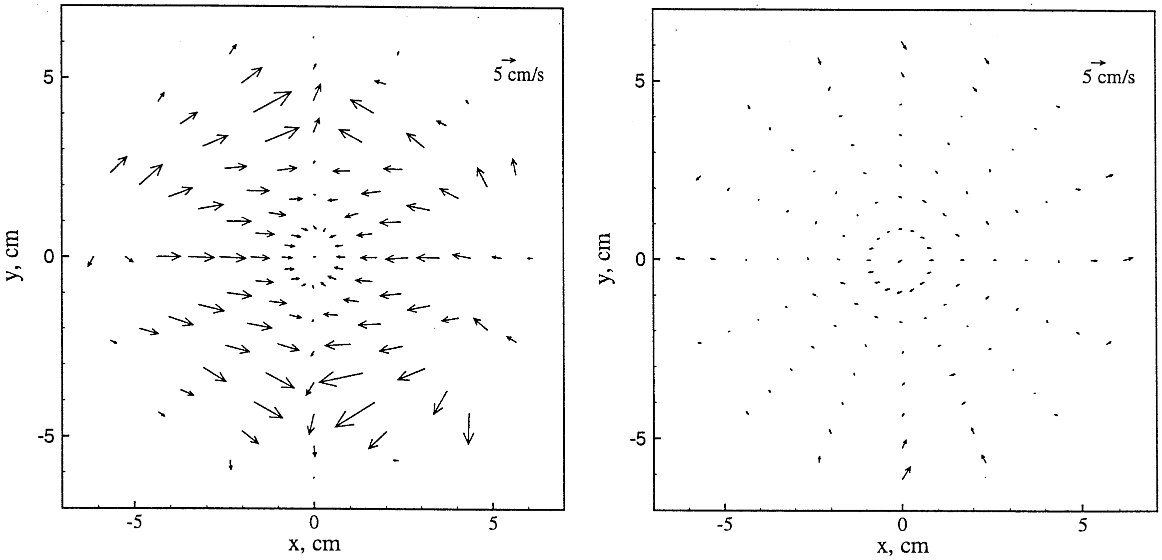

(a) z = 5 cm

(b) z = 20 cm

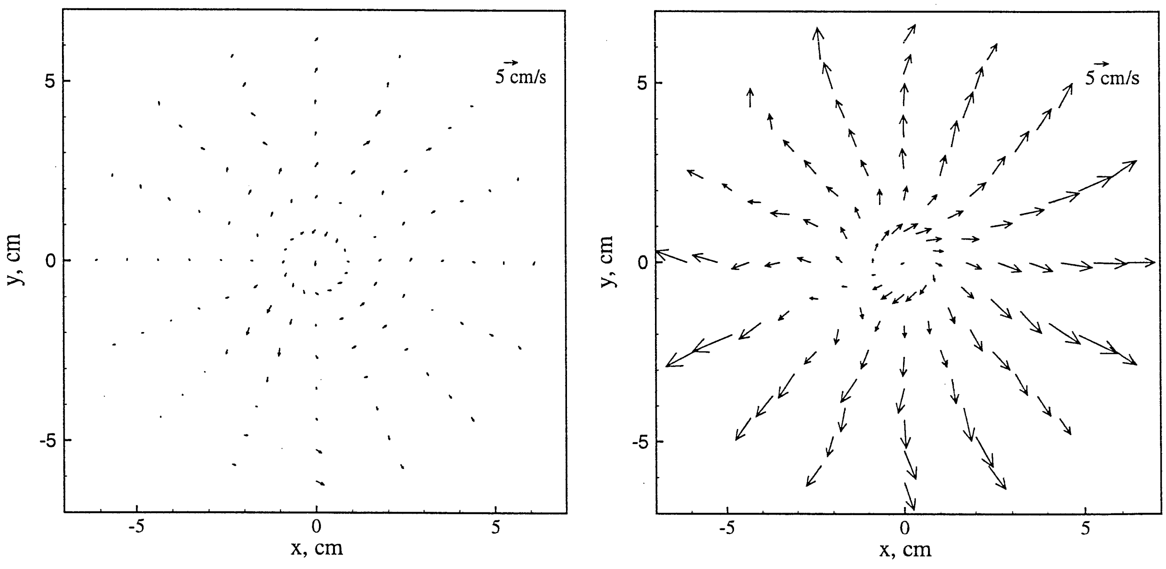

(c) z = 80 cm

(d) z = 130 cm

Figure 4.10: Velocity Vector Plots (Cross-sectional Views) for Column Diameter 14 cm, Distributor: Perforated Plate (**6A**), $U_g = 12.0$ cm/s

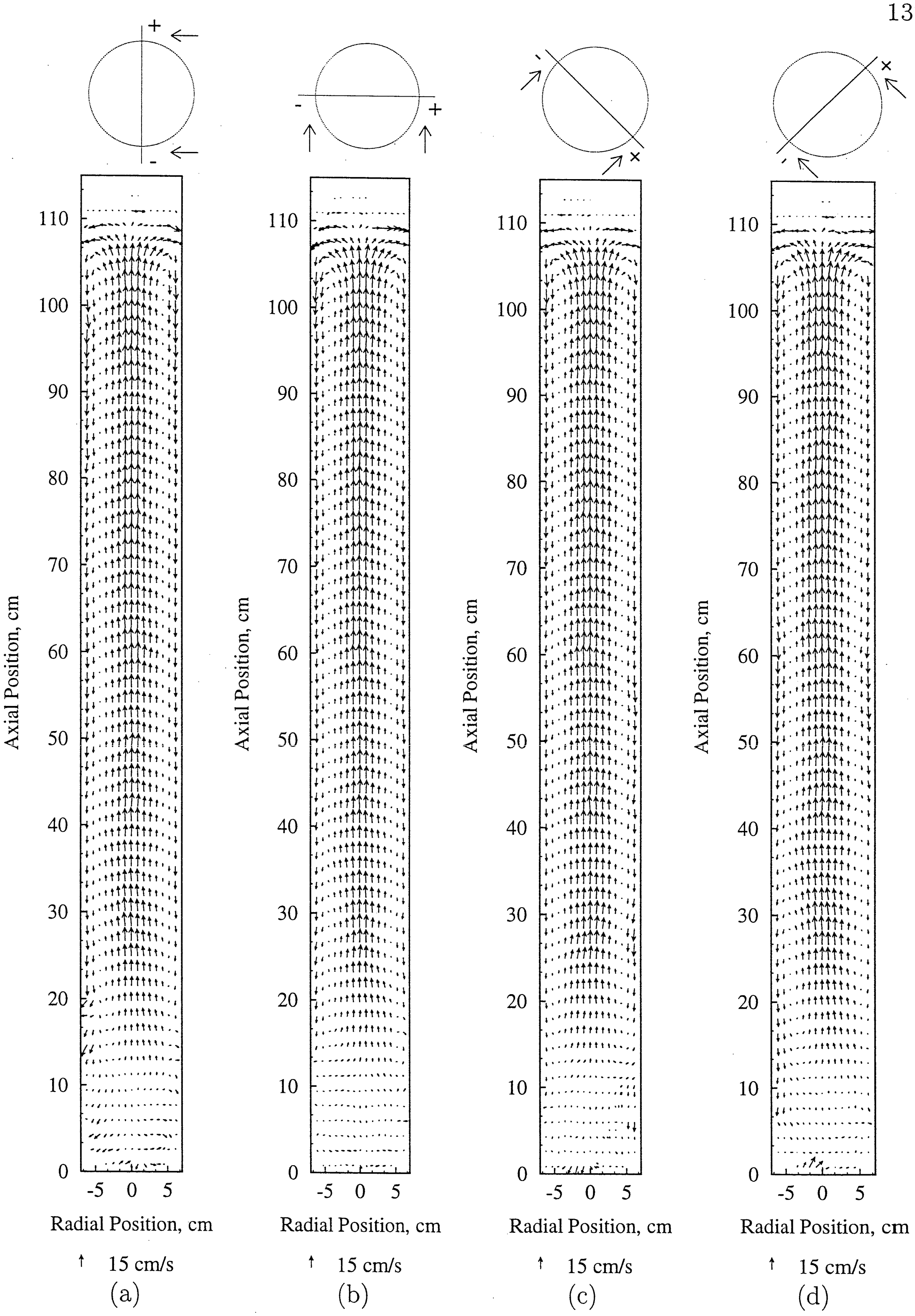

Figure 4.11: Velocity Vector Plots (Longitudinal Views) for Column Diameter 14 cm, Distributor: Perforated Plate **6B**, $U_g = 2.4$ cm/s

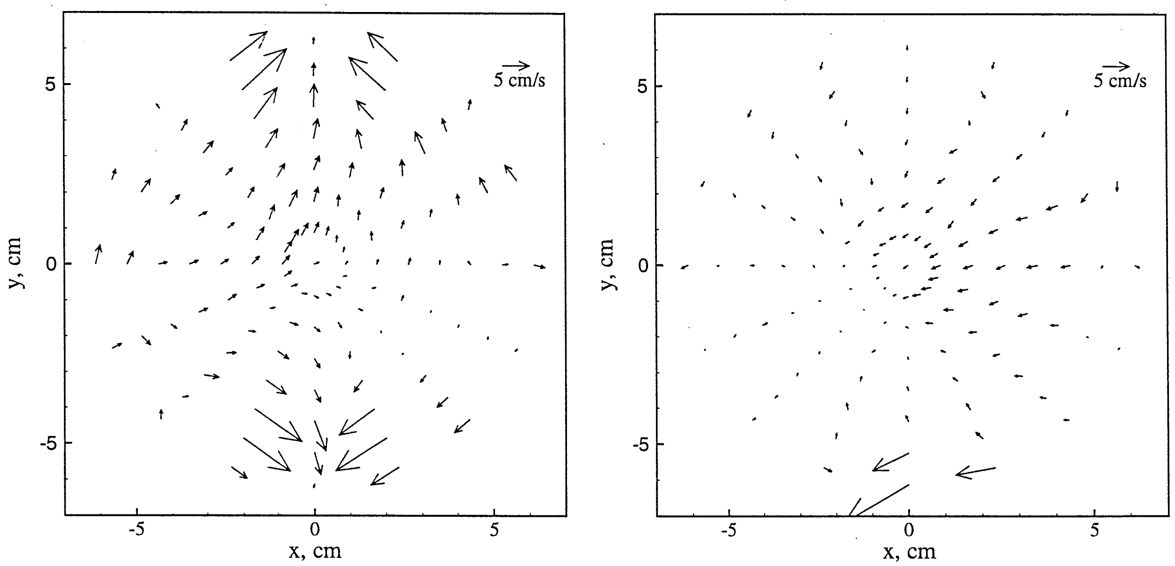

(a) z = 5 cm

(b) z = 20 cm

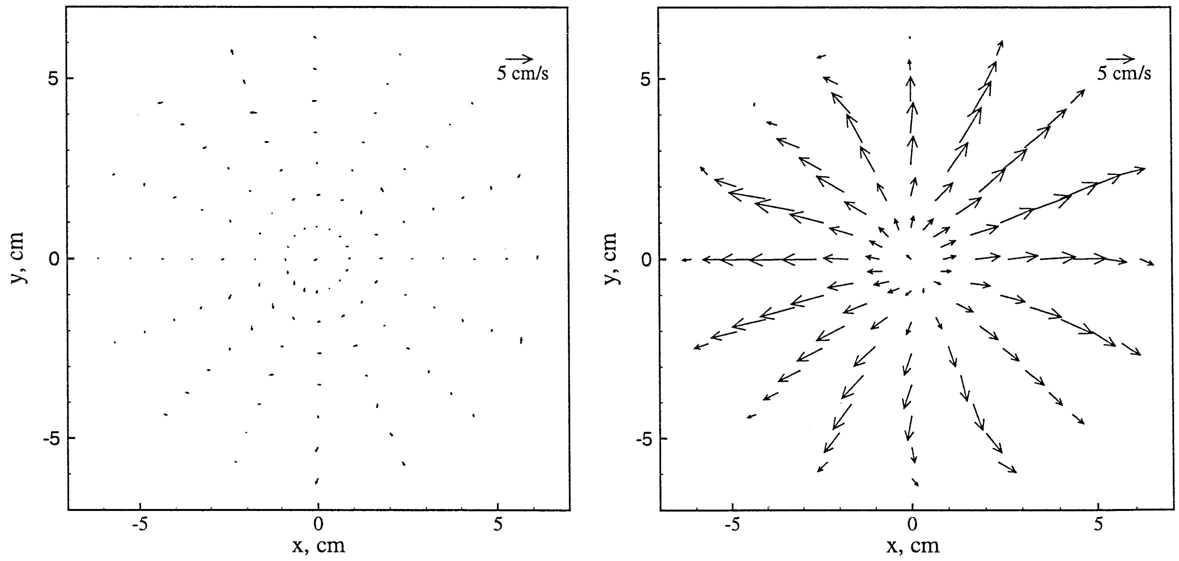

(c) z = 80 cm

(d) z = 105 cm

Figure 4.12: Velocity Vector Plots (Cross-sectional Views) for Column Diameter 14 cm, Distributor: Perforated Plate (**6B**), U_g = 2.4 cm/s

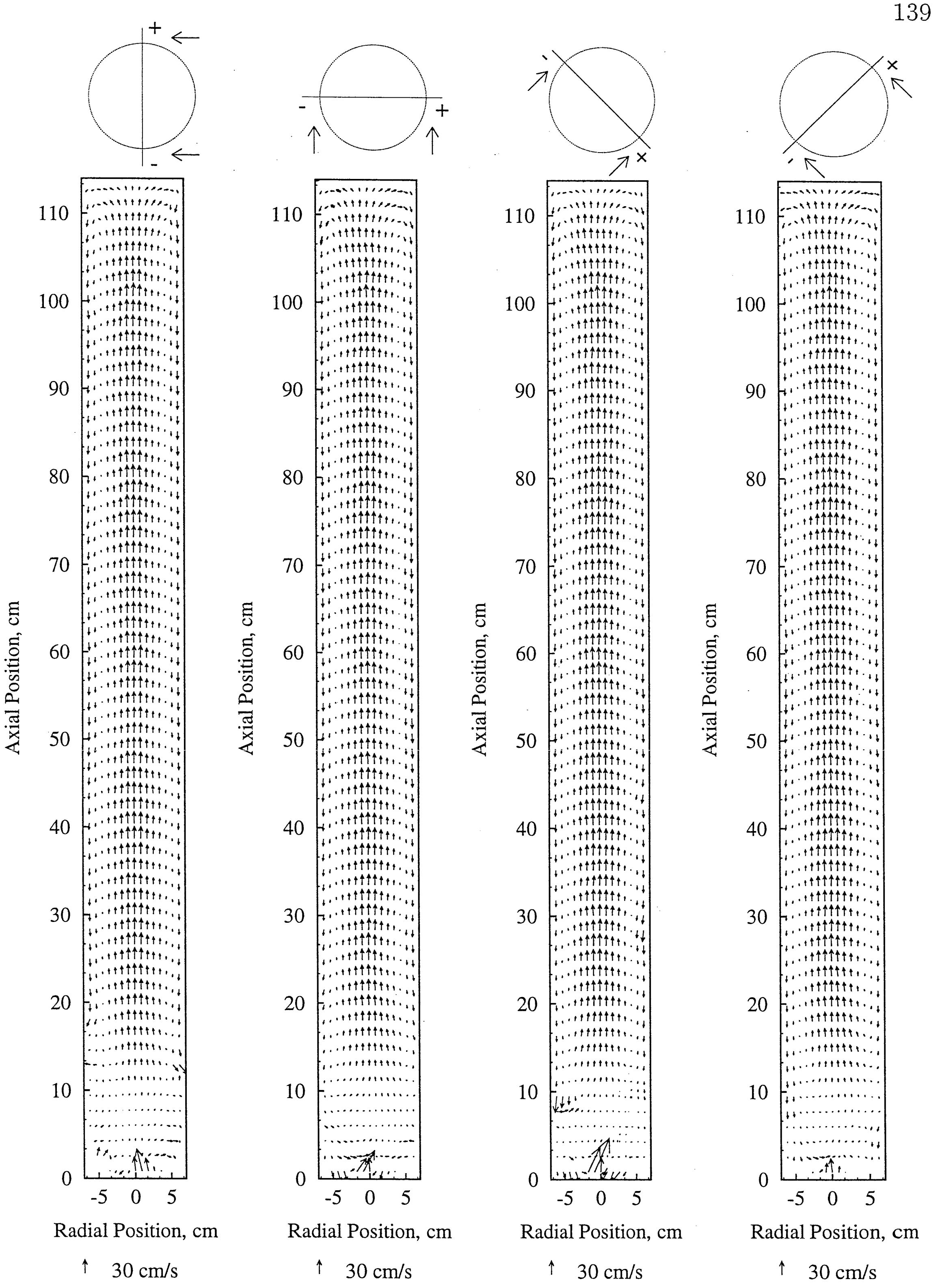

(a) (b) (c) (d)

Figure 4.13: Velocity Vector Plots (Longitudinal Views) for Column Diameter 14 cm, Distributor: Perforated Plate **6B**, $U_g = 4.8$ cm/s

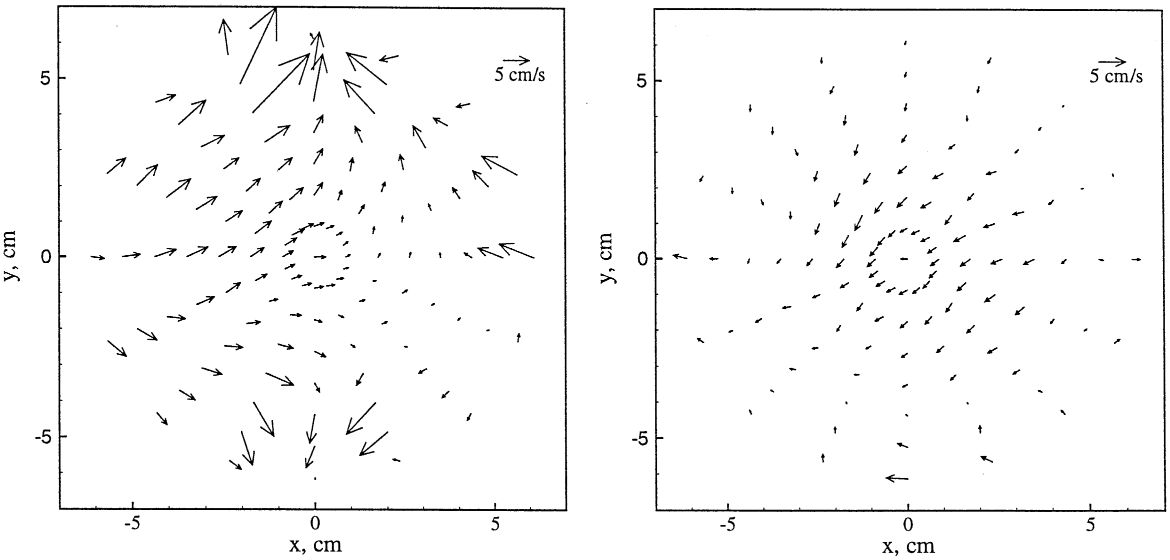

(a) z = 5 cm

(b) z = 20 cm

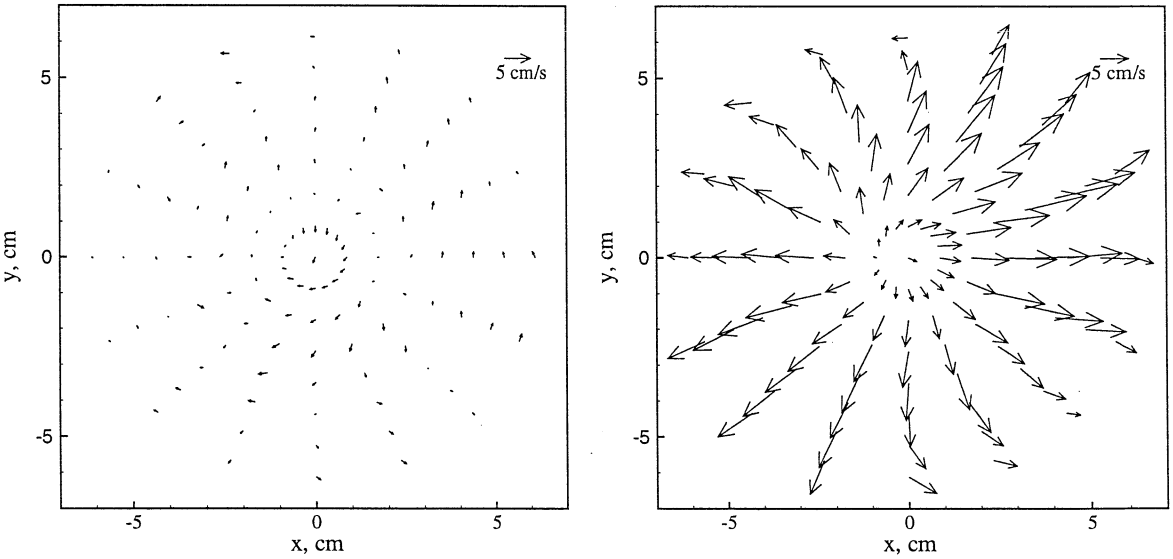

(c) z = 80 cm

(d) z = 112 cm

Figure 4.14: Velocity Vector Plots (Cross-sectional Views) for Column Diameter 14 cm, Distributor: Perforated Plate (**6B**), $U_g = 4.8$ cm/s

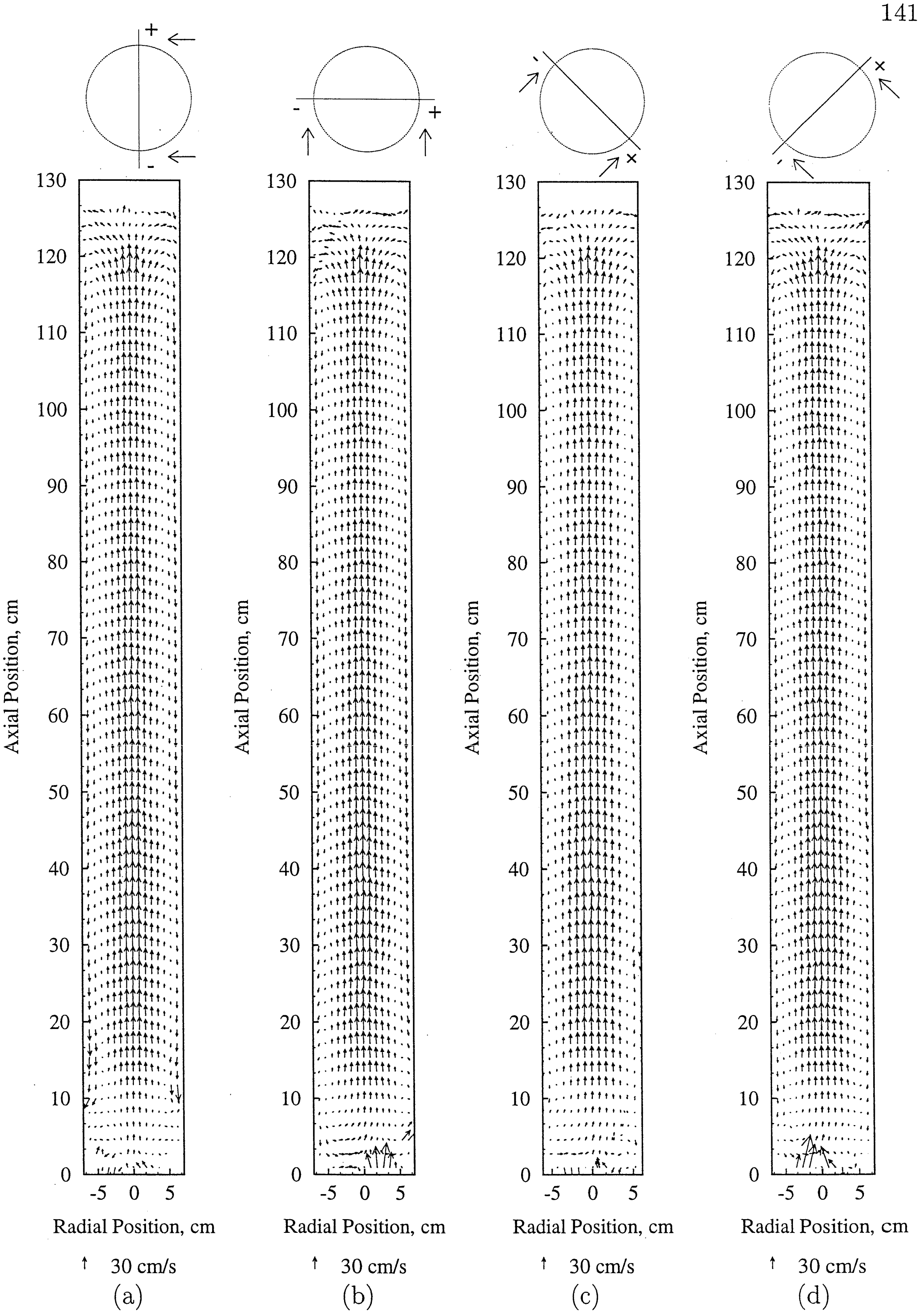

Figure 4.15: Velocity Vector Plots (Longitudinal Views) for Column Diameter 14 cm, Distributor: Perforated Plate **6B**, $U_g = 9.6$ cm/s

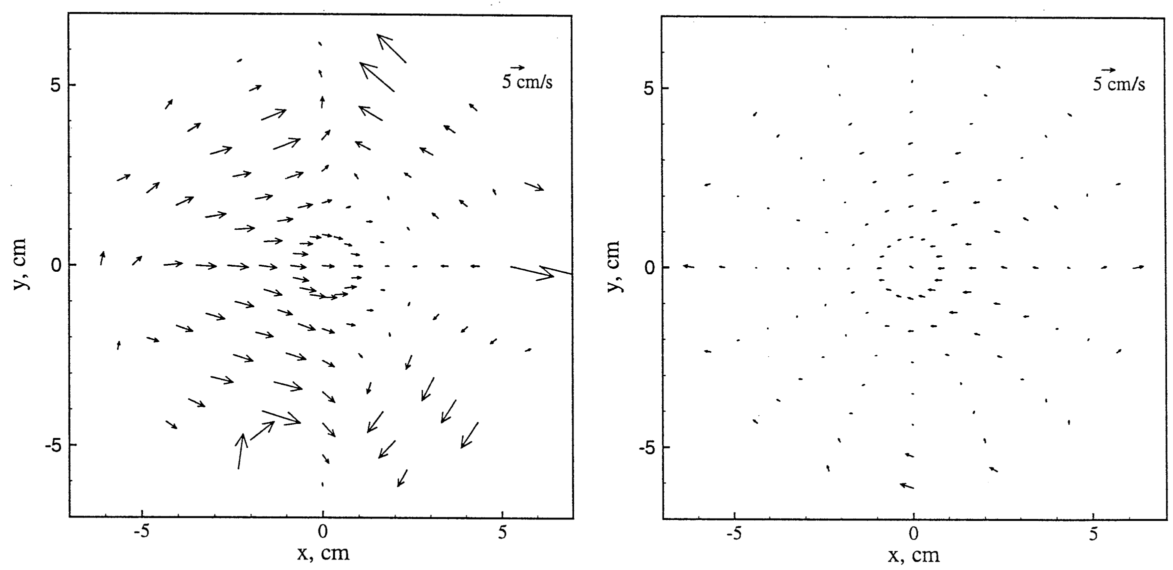

(a) z = 5 cm

(b) z = 20 cm

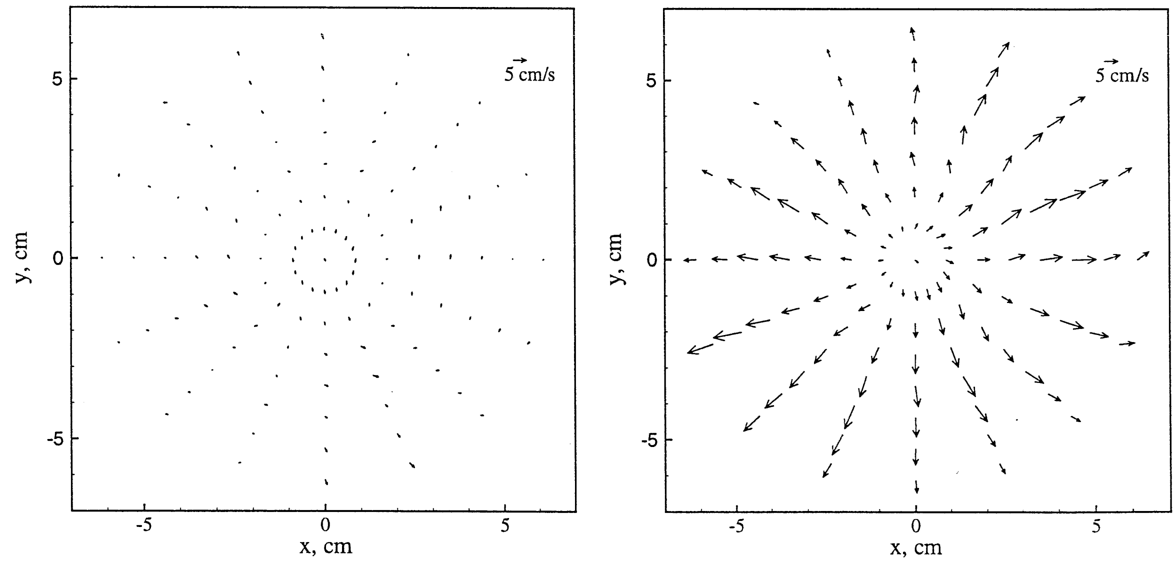

(c) z = 80 cm

(d) z = 120 cm

Figure 4.16: Velocity Vector Plots (Cross-sectional Views) for Column Diameter 14 cm, Distributor: Perforated Plate (**6B**), U_g = 9.6 cm/s

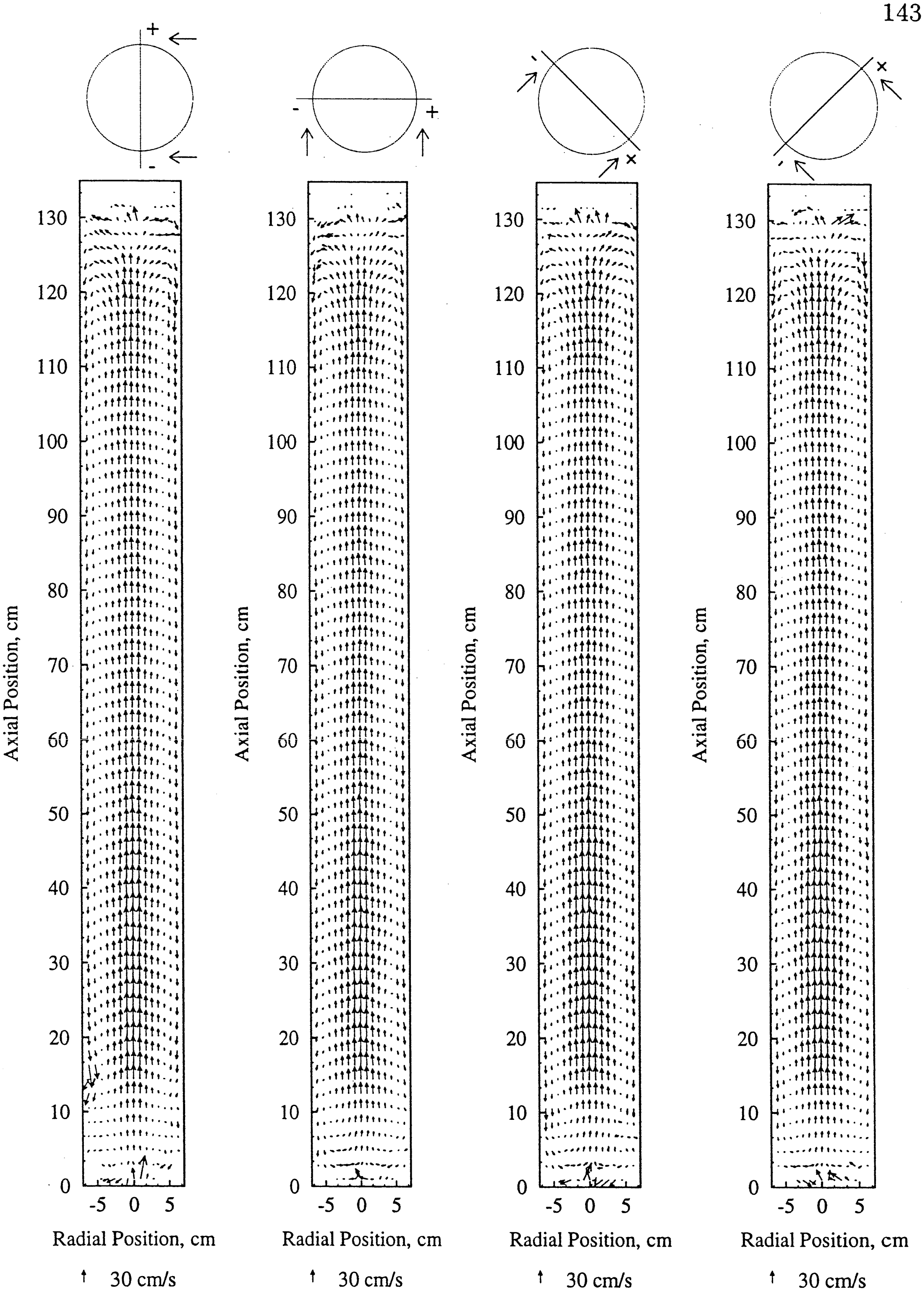

(a) (b) (c) (d)

Figure 4.17: Velocity Vector Plots (Longitudinal Views) for Column Diameter 14 cm, Distributor: Perforated Plate **6B**, U_g = 12.0 cm/s

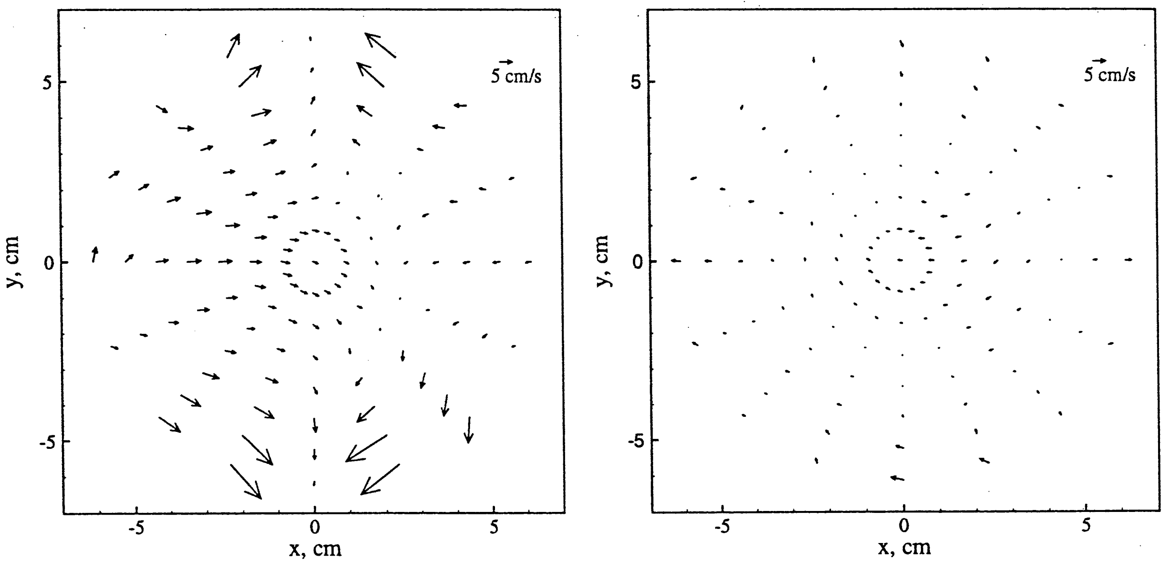

(a) z = 5 cm (b) z = 20 cm

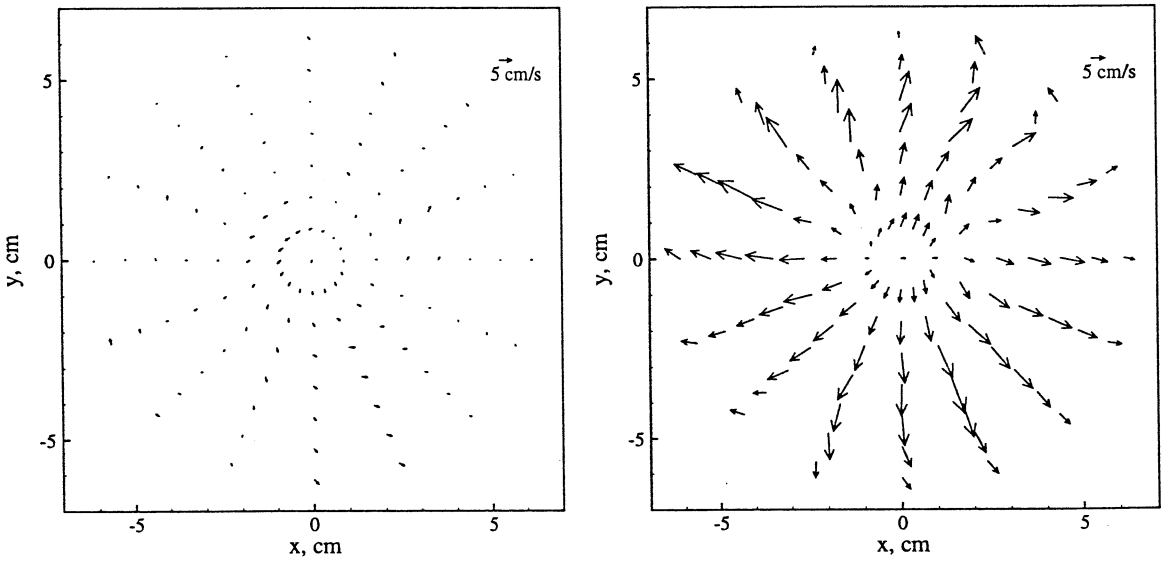

(c) z = 80 cm (d) z = 125 cm

Figure 4.18: Velocity Vector Plots (Cross-sectional Views) for Column Diameter 14 cm, Distributor: Perforated Plate (**6B**), $U_g = 12.0$ cm/s

The flow pattern near the distributor for all the gas velocities is similar to the roller like behavior observed at the higher gas velocities (9.6 and 12.0 cm/s), using distributor **6A**. It appears for all these cases, that the directional preference near the distributor is the same, as discussed before for the higher gas velocities with **6A**.

4.2.2 Flow pattern in the 19 cm column

For the 19 cm column using a perforated plate with 0.33 mm holes, the general observations noted for the 14 cm column (**6A**) seem to hold with an apparently greater influence of distributor, as can be seen in Figures 4.19 to 4.24. In this column, at 2 cm/s superficial gas velocity, a strong circulation cell is observed at the distributor, that extends over the entire column cross-section and has a height of exactly one column diameter. There is another weaker cell superimposed on the first cell, which is not as distinct as the first cell. These cells, as noted before, do not exhibit any strong swirling flow characteristics, but resemble a cylinder like structure (can be visualized as a sheet rolled into a cylinder). Further up in the column, the flow appears to approach symmetry. The asymmetry at the distributor persists even at a superficial gas velocity of 5 cm/s (Figure 4.21), along with the circulation cell, which is weaker in this case. At 12 cm/s, there is no circulation cell at the bottom, but the distinct asymmetry in the flow at the distributor is still evident.

Chen et al. (1994) describe a vortical-spiral flow regime at gas velocities between 1.7 and 2.1 cm/s in a 10 cm diameter column, wherein they observe clustering of the gas bubbles in the central portion of the column, which tend to form a bubble stream moving in a rocking spiral manner. However, these observations are based on instantaneous measurements. It should be noted that the structures that are observed in the present work represent the time averaged flow and not instantaneous flow phenomena. Such cells are evident only for the 19 cm diameter column with a perforated plate distributor (hole size 0.33 mm), and not for any other column size.

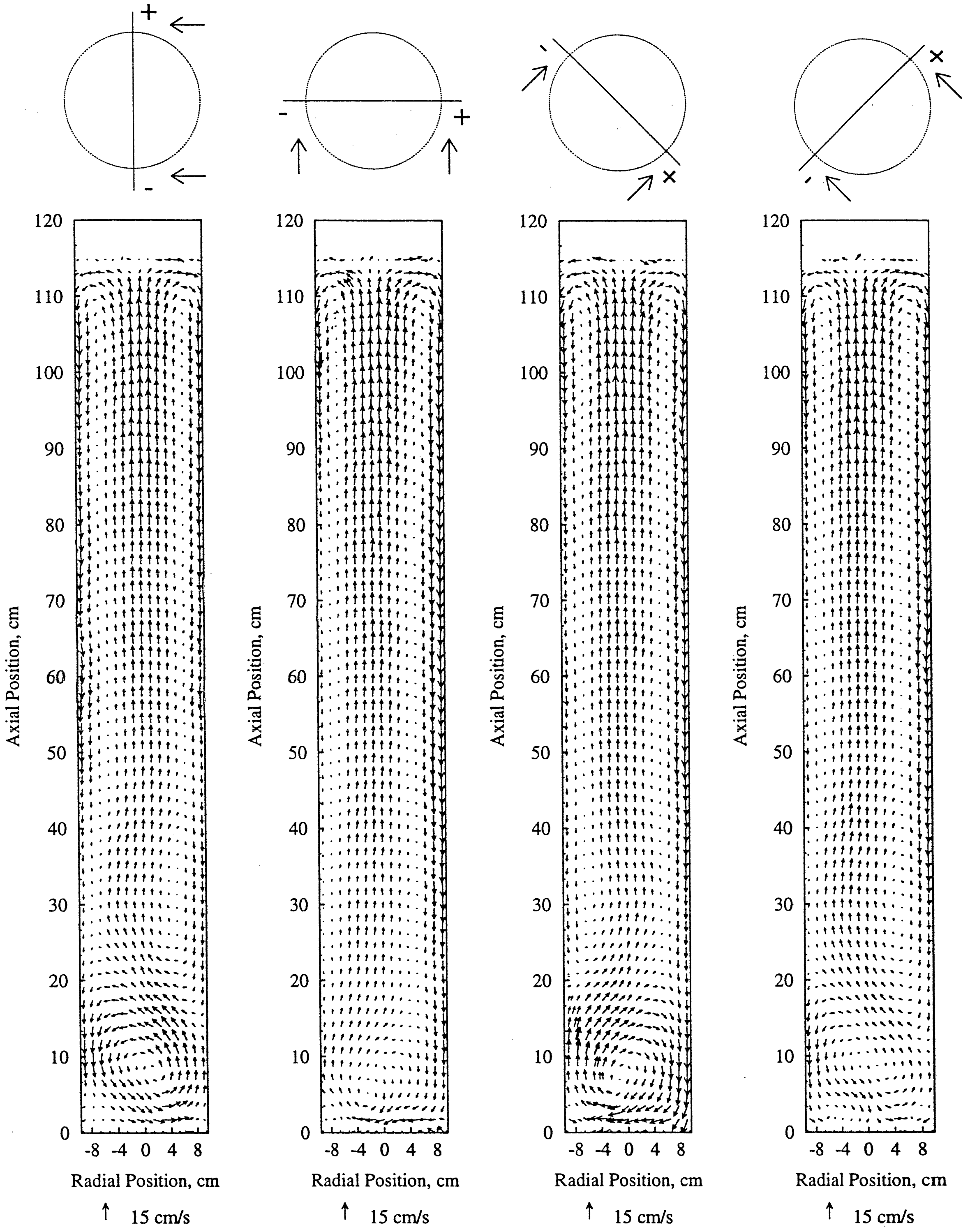

Figure 4.19: Velocity Vector Plots (Longitudinal Views) for Column Diameter 19 cm, Distributor: Perforated Plate **8A**, $U_g = 2.0$ cm/s

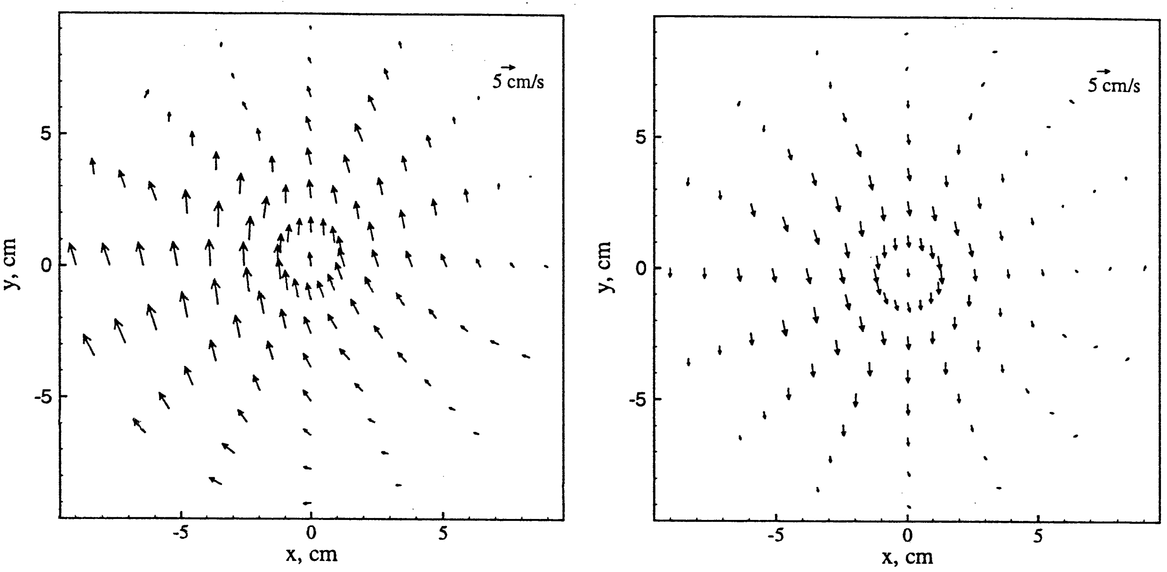

(a) z = 5 cm

(b) z = 20 cm

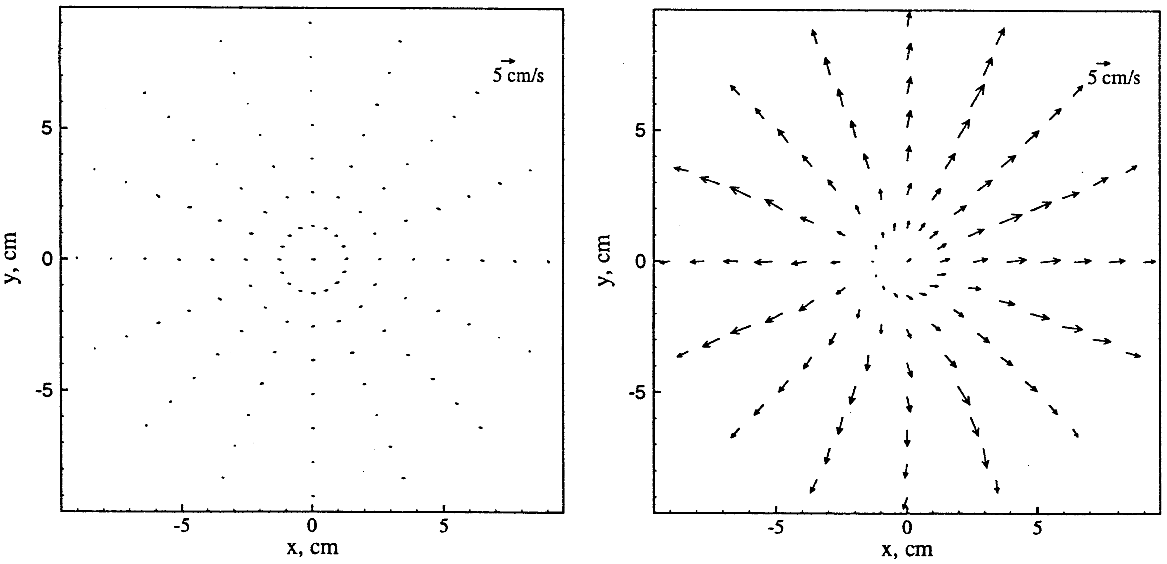

(c) z = 90 cm

(d) z = 112 cm

Figure 4.20: Velocity Vector Plots (Cross-sectional Views) for Column Diameter 19 cm, Distributor: Perforated Plate (**8A**), $U_g = 2.0$ cm/s

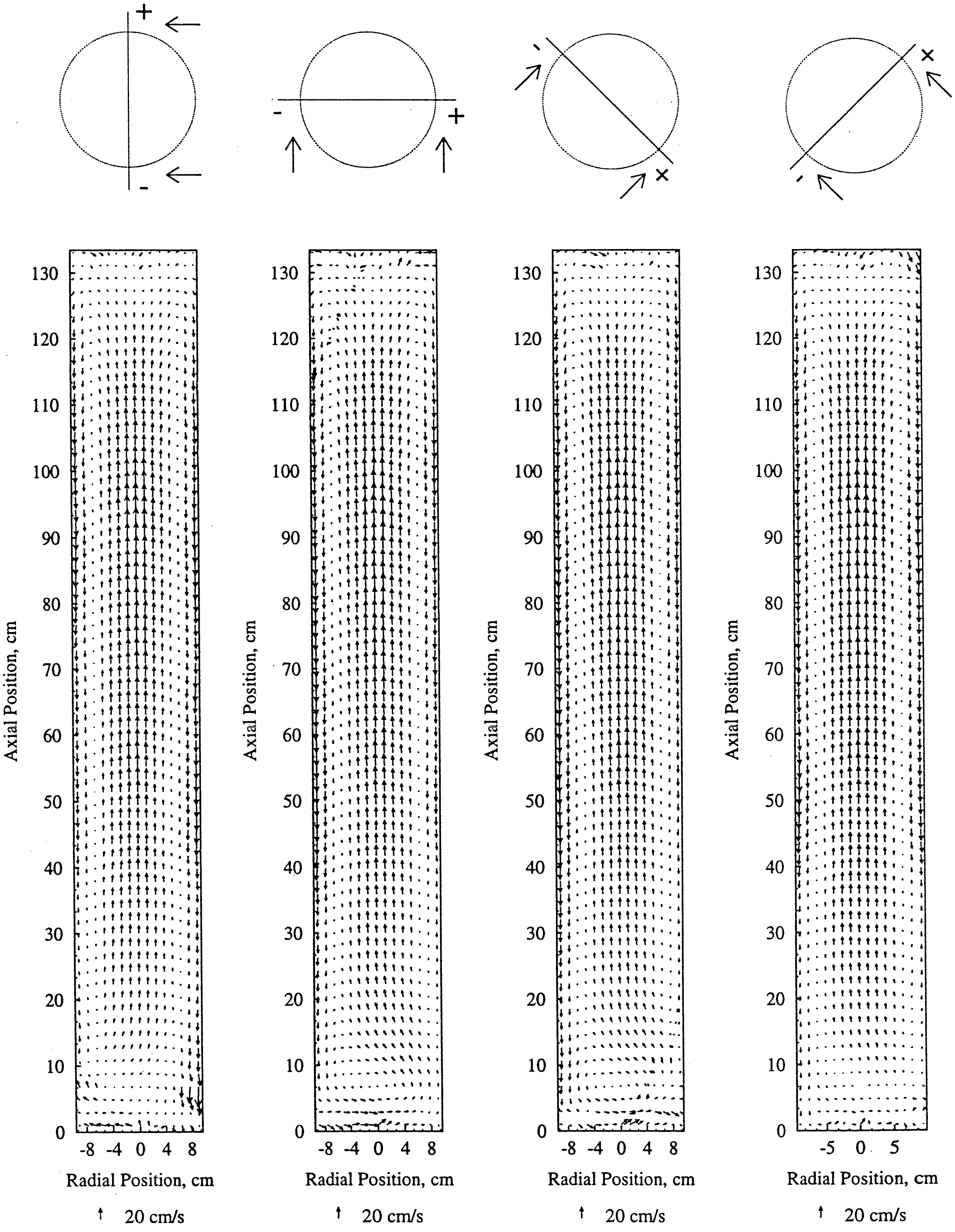

(a) (b) (c) (d)

Figure 4.21: Velocity Vector Plots (Longitudinal Views) for Column Diameter 19 cm, Distributor: Perforated Plate **8A**, $U_g = 5.0$ cm/s

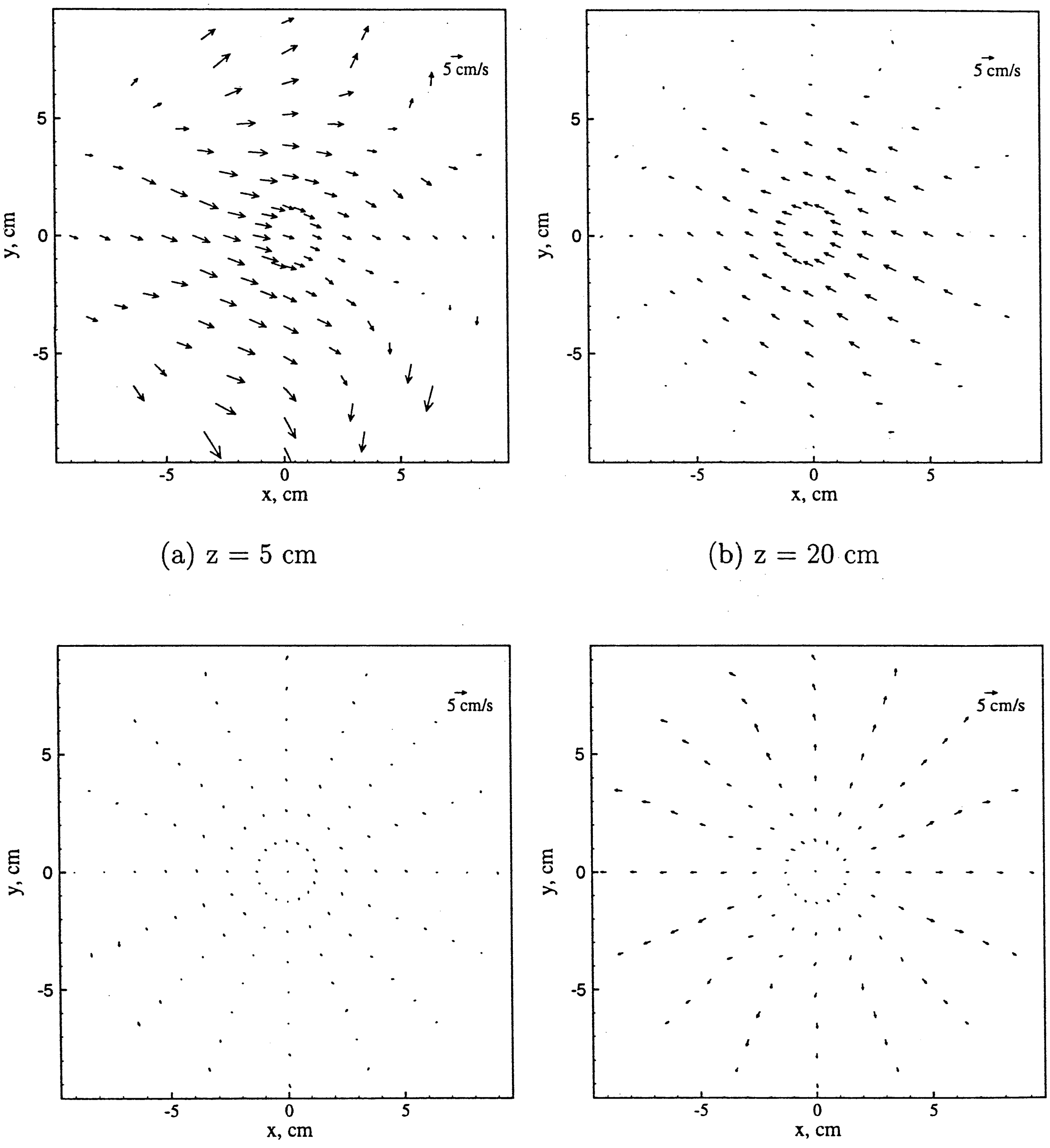

(a) z = 5 cm

(b) z = 20 cm

(c) z = 80 cm

(d) z = 125 cm

Figure 4.22: Velocity Vector Plots (Cross-sectional Views) for Column Diameter 19 cm, Distributor: Perforated Plate (**8A**), U_g = 5.0 cm/s

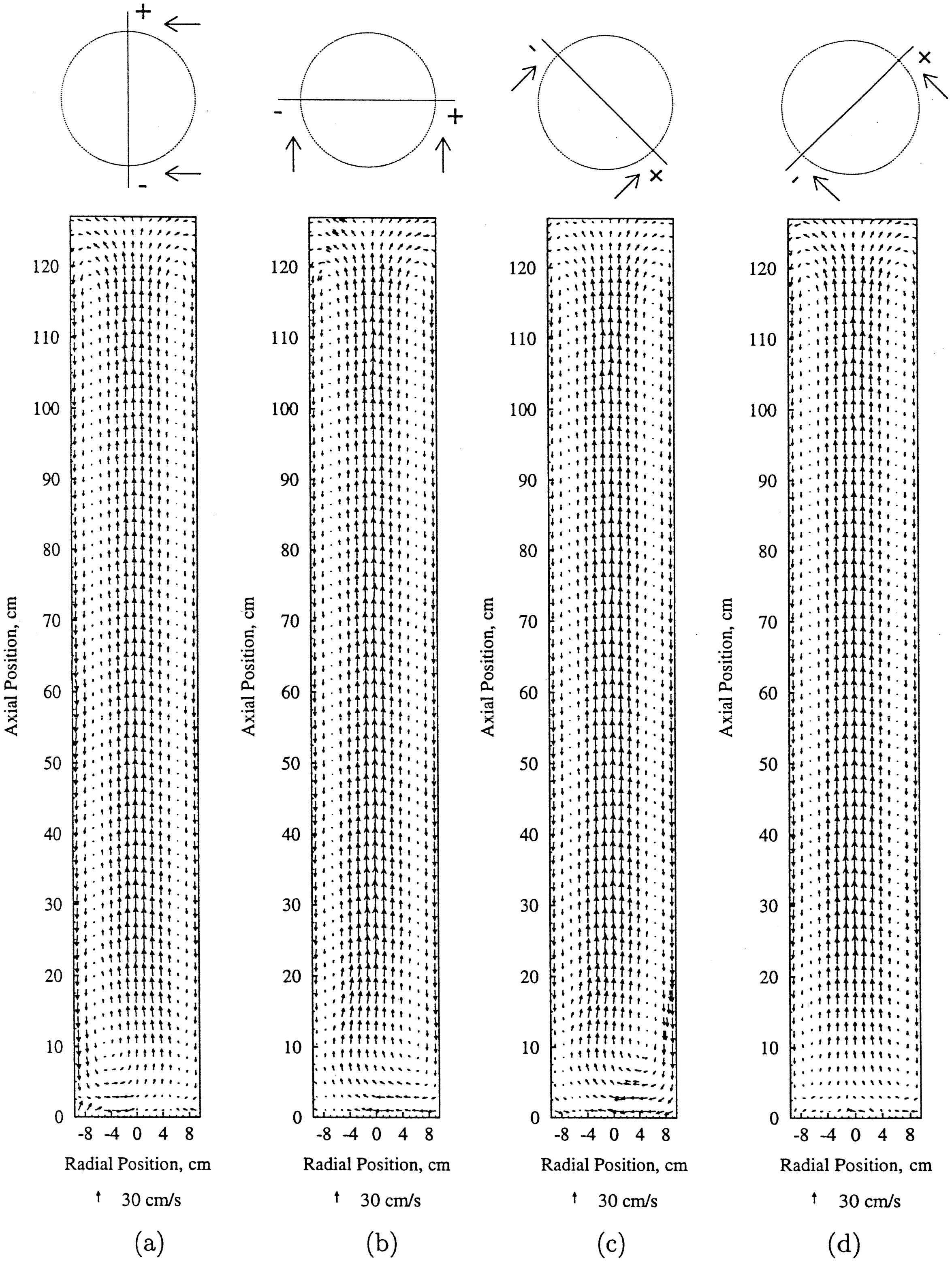

Figure 4.23: Velocity Vector Plots (Longitudinal Views) for Column Diameter 19 cm, Distributor: Perforated Plate **8A**, $U_g = 12.0$ cm/s

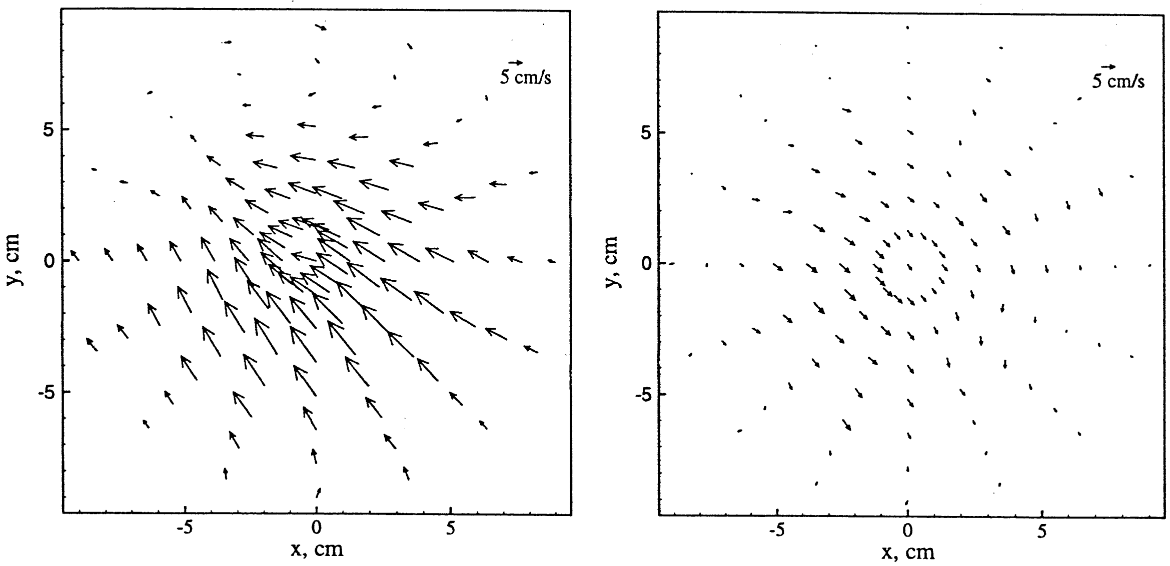

(a) z = 5 cm

(b) z = 20 cm

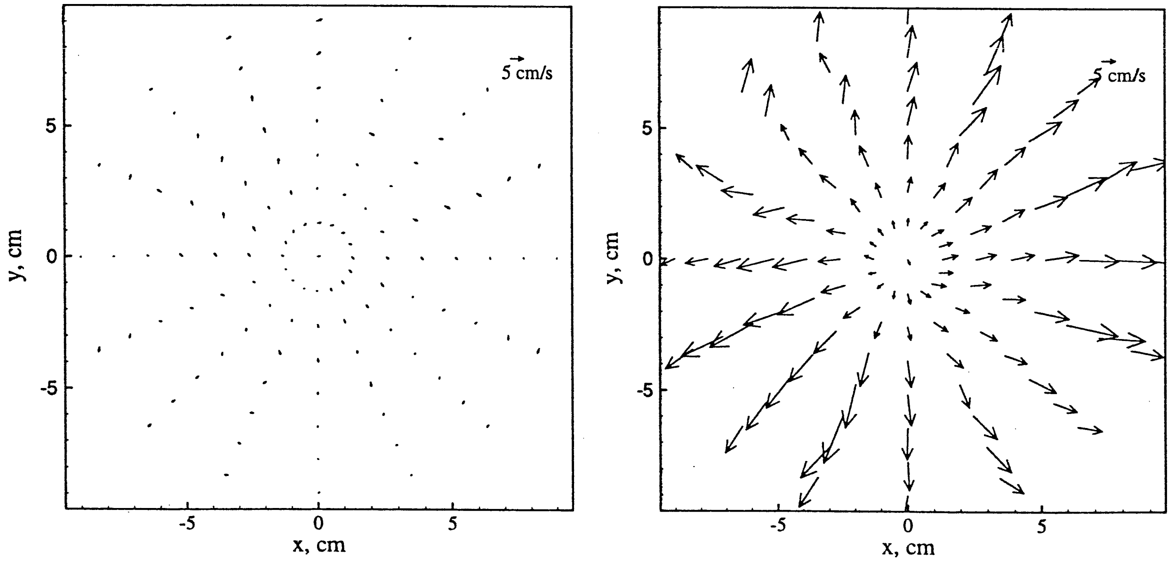

(c) z = 80 cm

(d) z = 125 cm

Figure 4.24: Velocity Vector Plots (Cross-sectional Views) for Column Diameter 19 cm, Distributor: Perforated Plate (8A), U_g = 12.0 cm/s

This certainly points to the effects of hole size in the distributor. Perforated plate distributors have been used in all the column diameters investigated in this work. However, the perforated plate used for the 19 cm column has the smallest hole size (0.33 mm). It is possible that the imperfections in a perforated plate distributor affect the flow pattern, more for cases of distributors with smaller size holes. The tendency for the formation of circulation cells, in the time averaged sense, increases with decrease in hole size and thereby bubble size.

Experiments performed at $U_g = 12$ cm/s using the bubble cap and cone distributors show similarities with the high gas velocity conditions in the 14 cm column (**6A** and **6B**), for the time averaged flow pattern. This again is attributed to the type of sparger used, and the absence of the additional influence in the distributor region, caused by the presence of the plate of the perforated plate distributor. For all the experimental conditions in the 19 cm diameter column, the flow at higher axial levels in the column tends to become symmetric with respect to the column axis. For the case of the low gas velocity experiment, i.e., at 2 cm/s, this occurs only high up in the column ($z \geq 4\ D_c$). For the higher gas velocities the asymmetry disappears after heights less than two times the column diameter. These trends are similar to that of the 14 cm column.

4.2.3 Flow pattern in the 44 cm column

The distributor used for the 44 cm column is a perforated plate, with 0.7 mm diameter holes. The resulting time averaged flow patterns show the presence of the asymmetric sheet like structure close to the distributor for all gas velocities (Figures 4.29 to 4.34). For the lower velocities of 2 cm/s and 5 cm/s, the flow does not seem to recover from the asymmetry at the distributor within the given dispersion height. Since the aspect ratio of the column is low (~ 4.5) the asymmetry persists through out the length of the dispersion. At the highest gas velocity studied which is 10 cm/s, it appears that far above the distributor, i.e., at about 3.0 times the column diameter (132 cm) the flow becomes symmetric about the column axis.

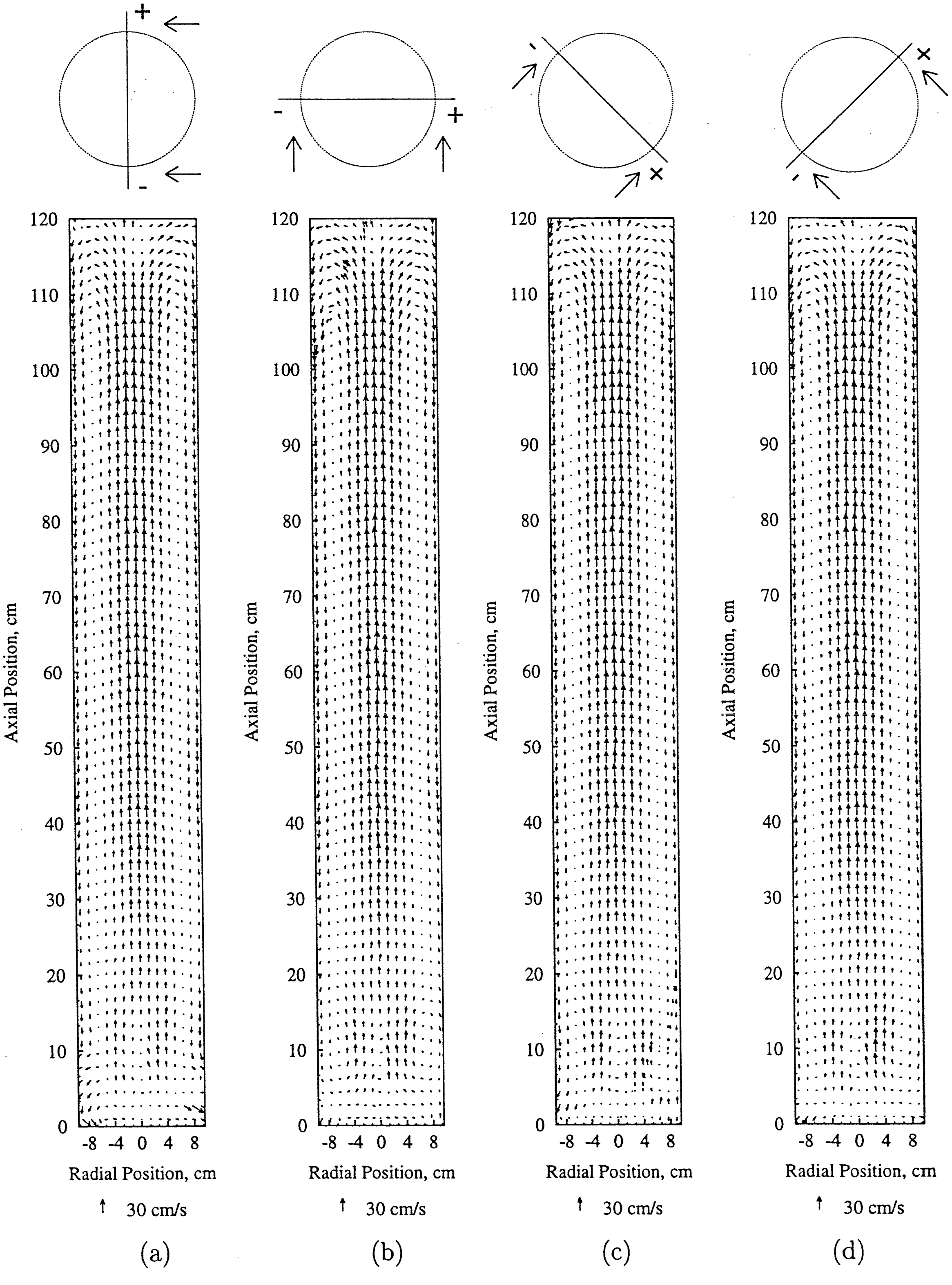

Figure 4.25: Velocity Vector Plots (Longitudinal Views) for Column Diameter 19 cm, Distributor: Bubble Cap **8B**, $U_g = 12.0$ cm/s

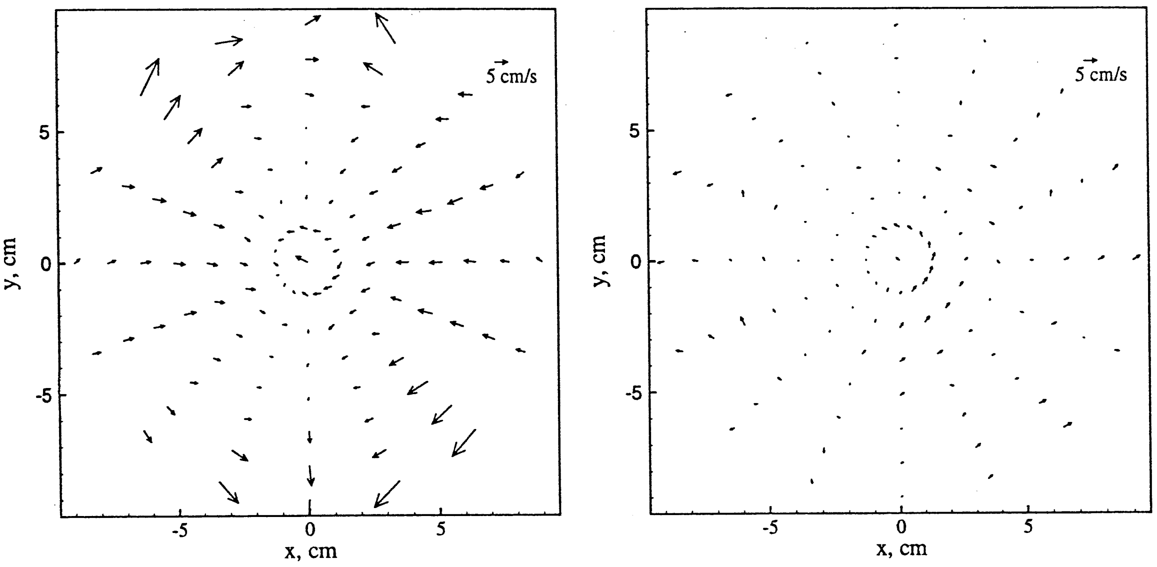

(a) z = 5 cm (b) z = 20 cm

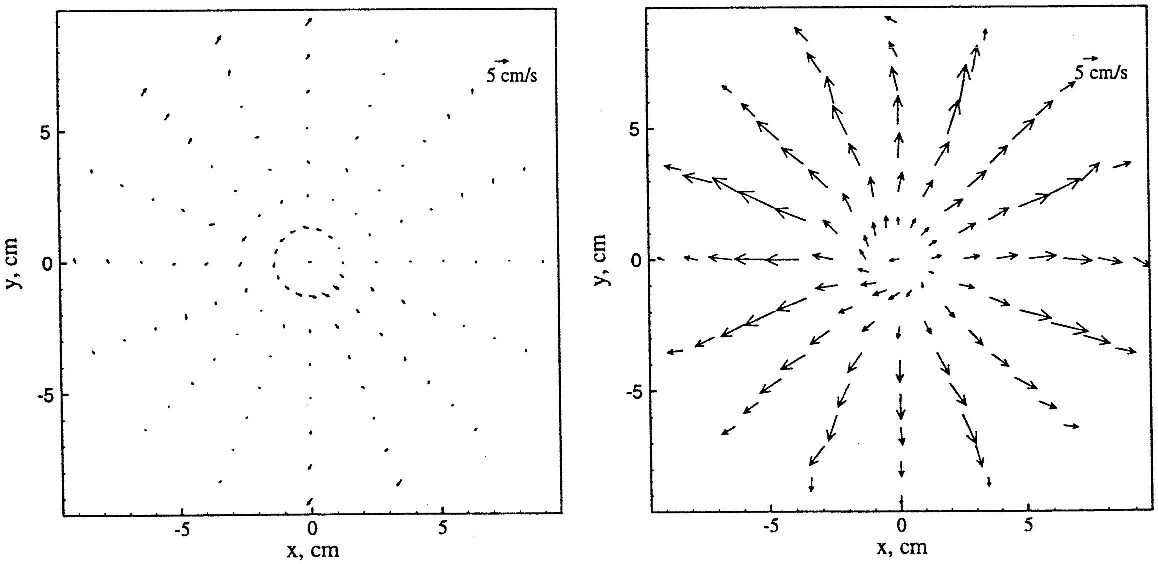

(c) z = 80 cm (d) z = 115 cm

Figure 4.26: Velocity Vector Plots (Cross-sectional Views) for Column Diameter 19 cm, Distributor: Bubble Cap (**8B**), U_g = 12.0 cm/s

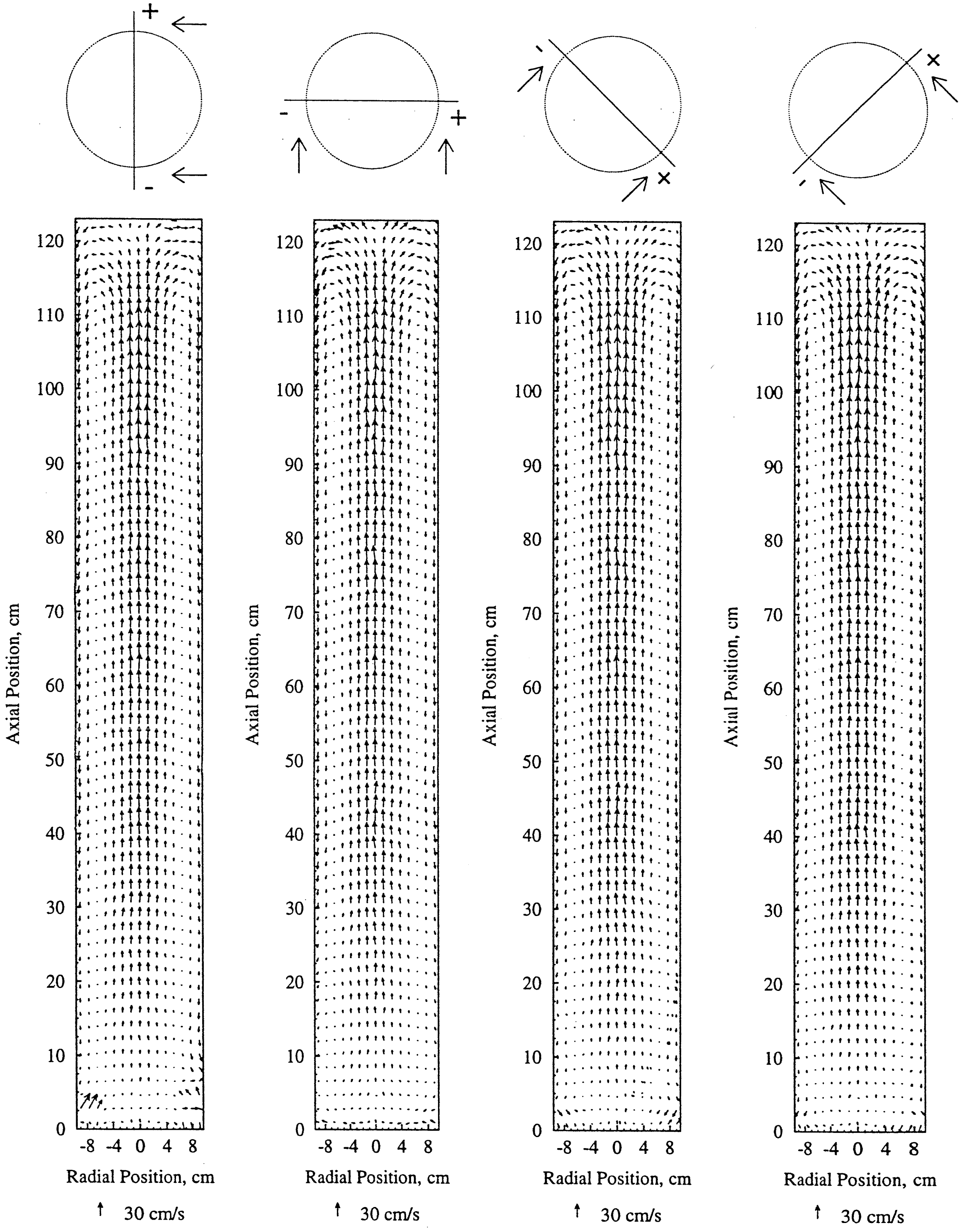

Figure 4.27: Velocity Vector Plots (Longitudinal Views) for Column Diameter 19 cm, Distributor: Inverted Cone 8C, $U_g = 12.0$ cm/s

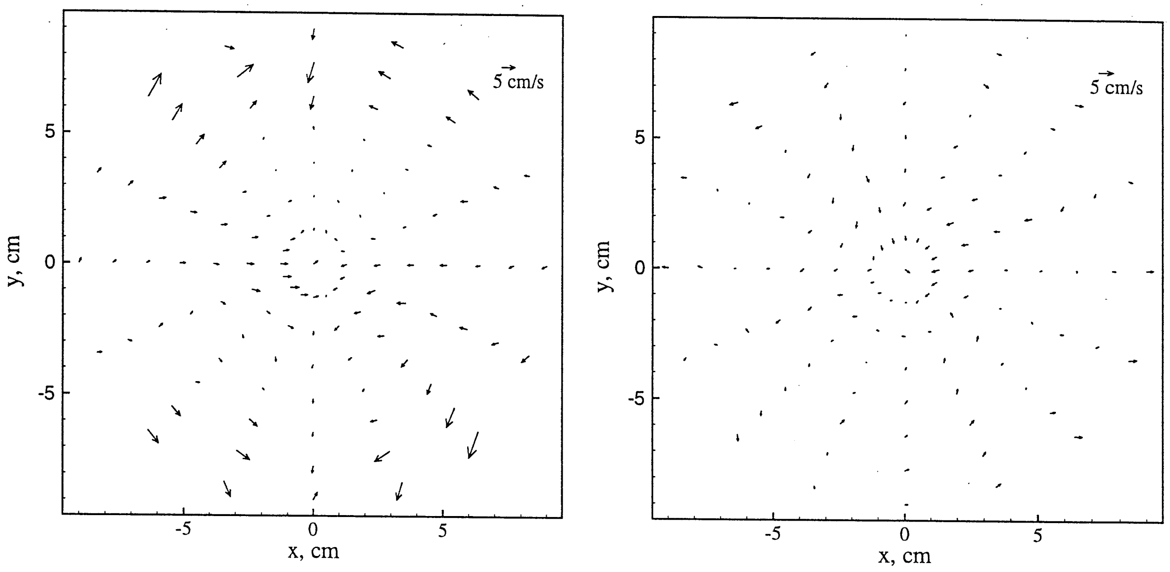

(a) z = 5 cm

(b) z = 20 cm

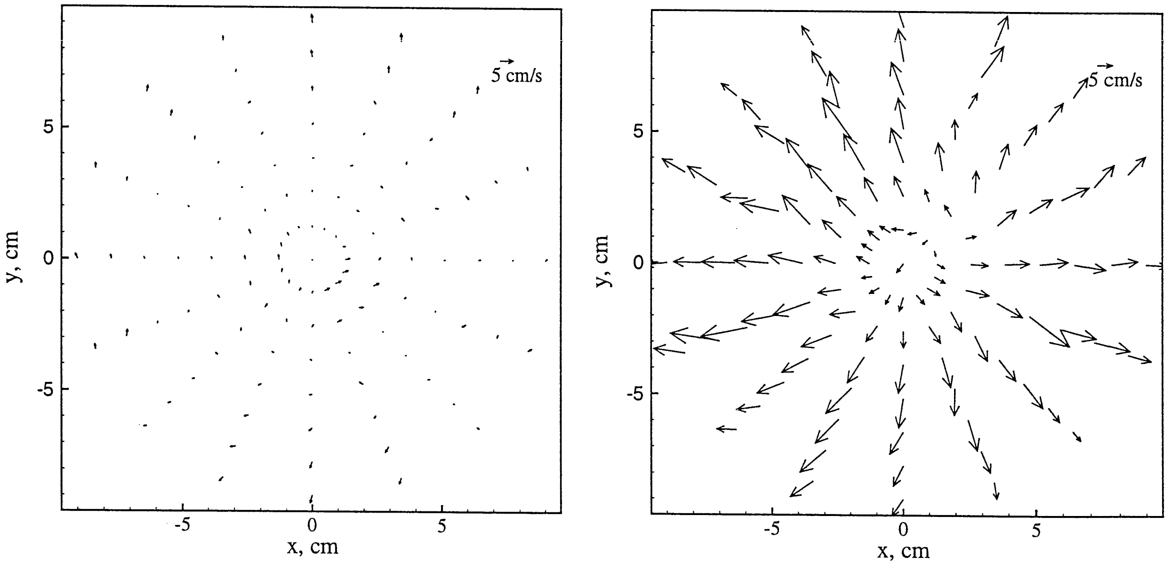

(c) z = 80 cm

(d) z = 120 cm

Figure 4.28: Velocity Vector Plots (Cross-sectional Views) for Column Diameter 19 cm, Distributor: Inverted Cone (**8C**), $U_g = 12.0$ cm/s

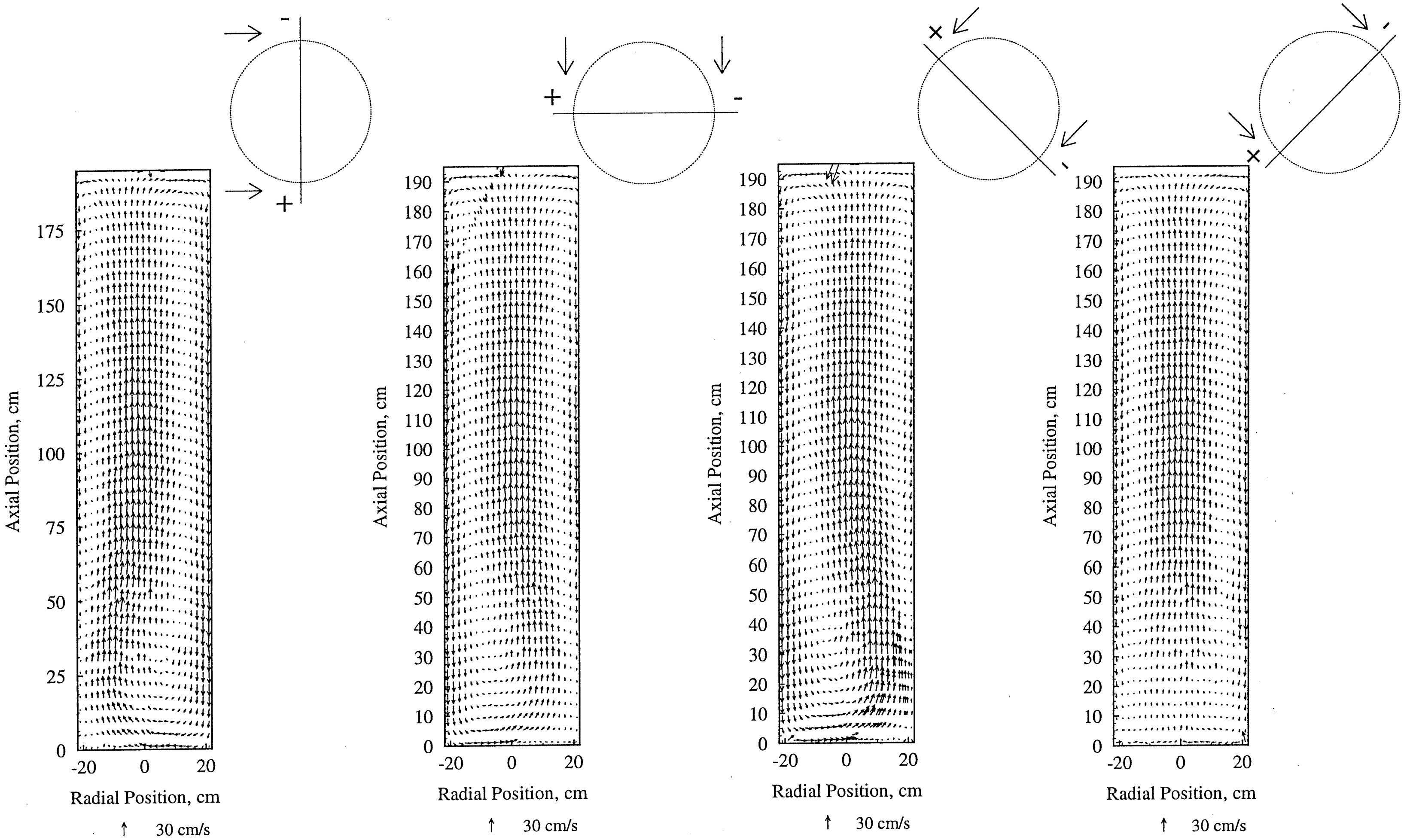

(a)

(b)

(c)

(d)

Figure 4.29: Velocity Vector Plots (Longitudinal Views) for Col. Dia. 44 cm, Distributor: Perforated Plate **18A**, $U_g = 2.0$ cm/s

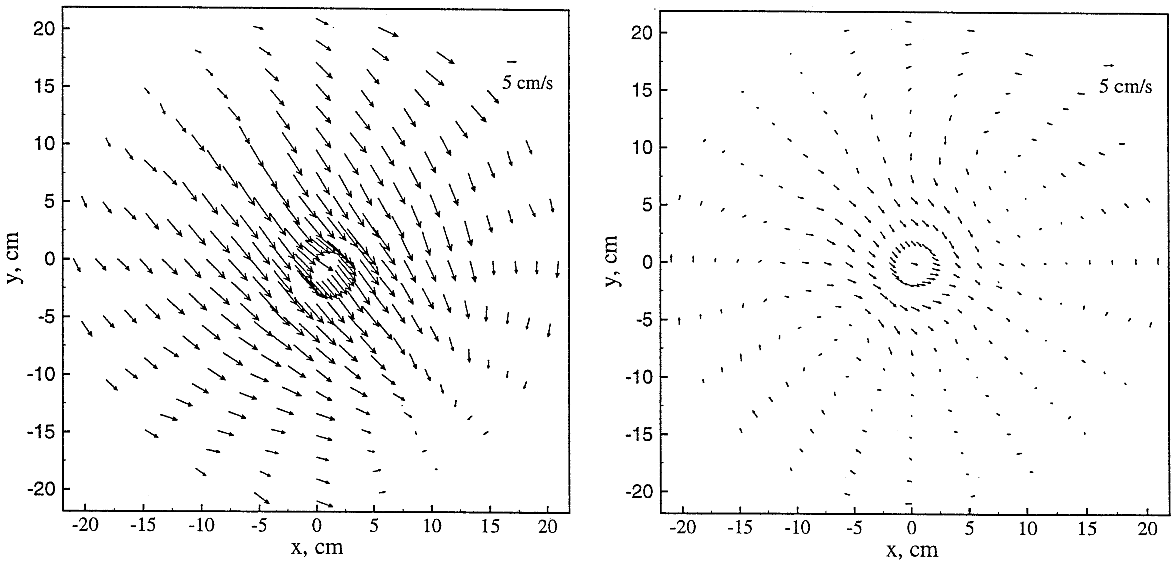

(a) z = 5 cm

(b) z = 25 cm

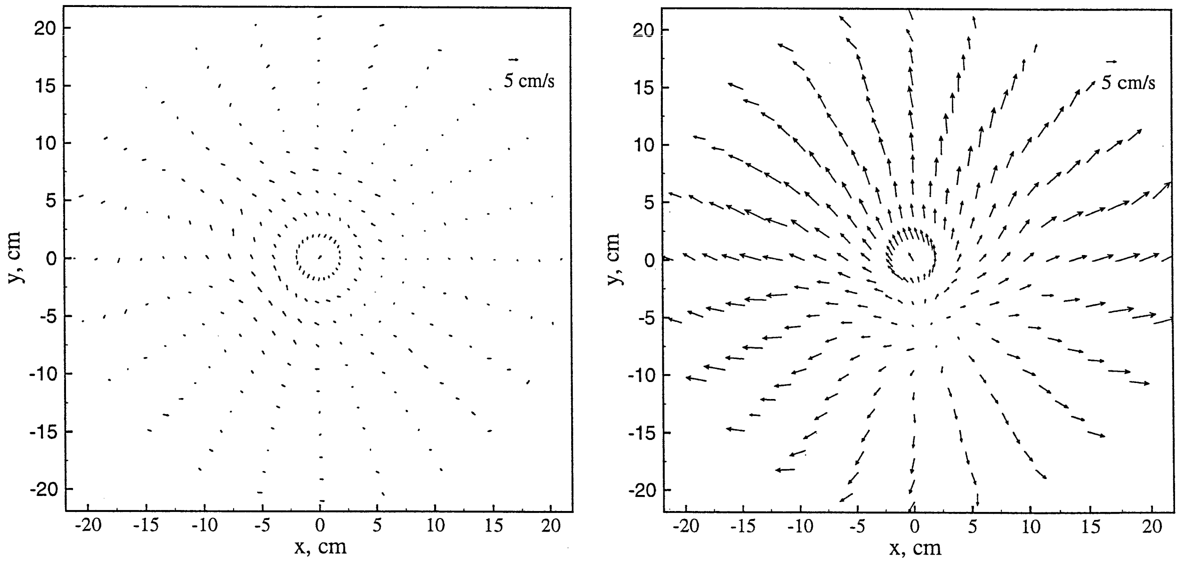

(c) z = 100 cm

(d) z = 190 cm

Figure 4.30: Velocity Vector Plots (Cross-sectional Views) for Column Diameter 44 cm, Distributor: Perforated Plate (**18A**), $U_g = 2.0$ cm/s

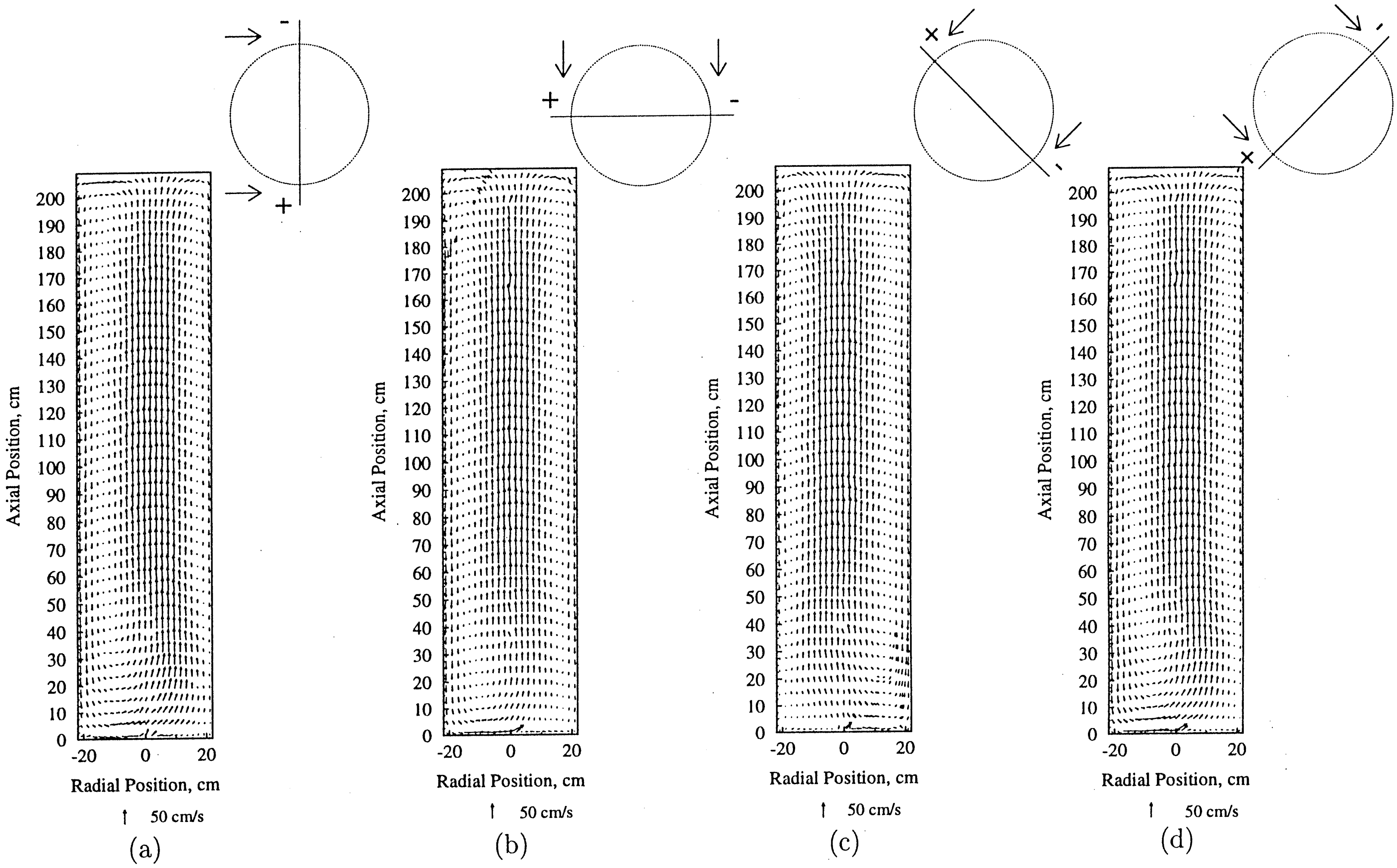

Figure 4.31: Velocity Vector Plots (Longitudinal Views) for Col. Dia. 44 cm, Distributor: Perforated Plate **18A**, $U_g = 5.0$ cm/s

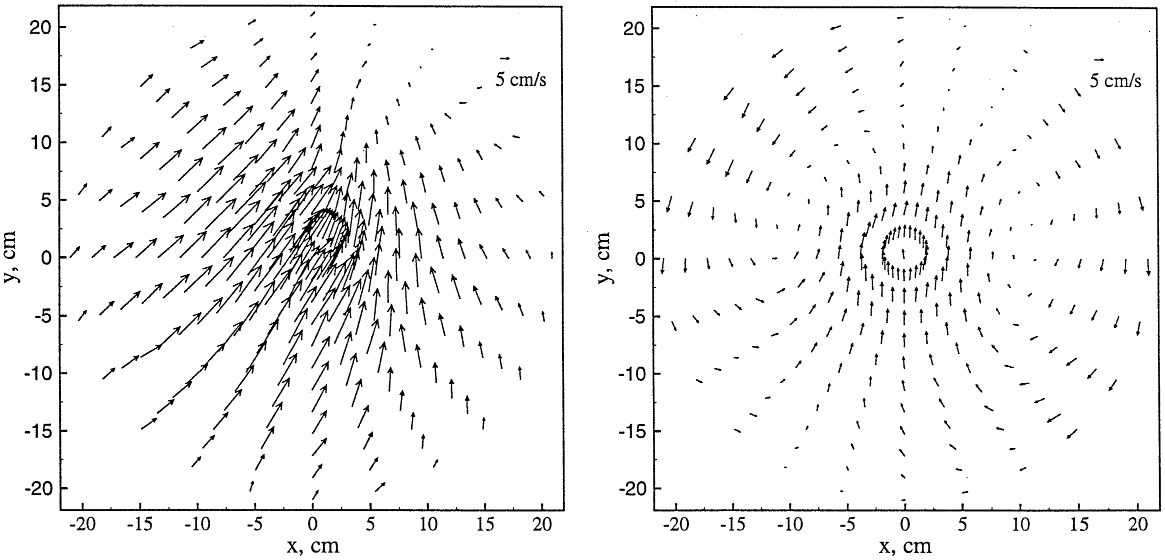

(a) z = 5 cm

(b) z = 25 cm

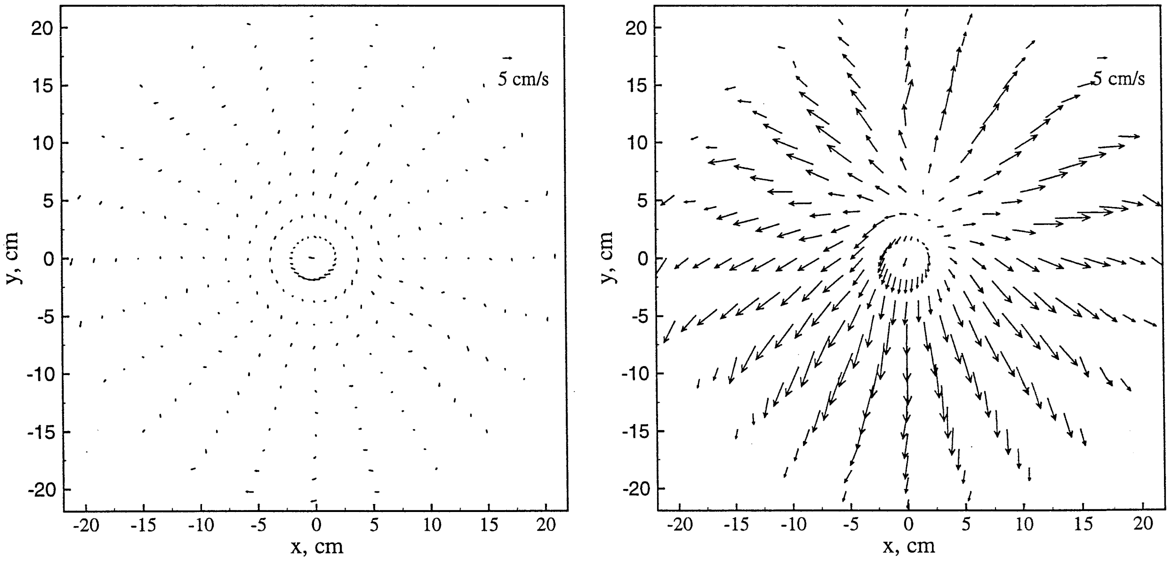

(c) z = 110 cm

(d) z = 205 cm

Figure 4.32: Velocity Vector Plots (Cross-sectional Views) for Column Diameter 44 cm, Distributor: Perforated Plate (**18A**), U_g = 5.0 cm/s

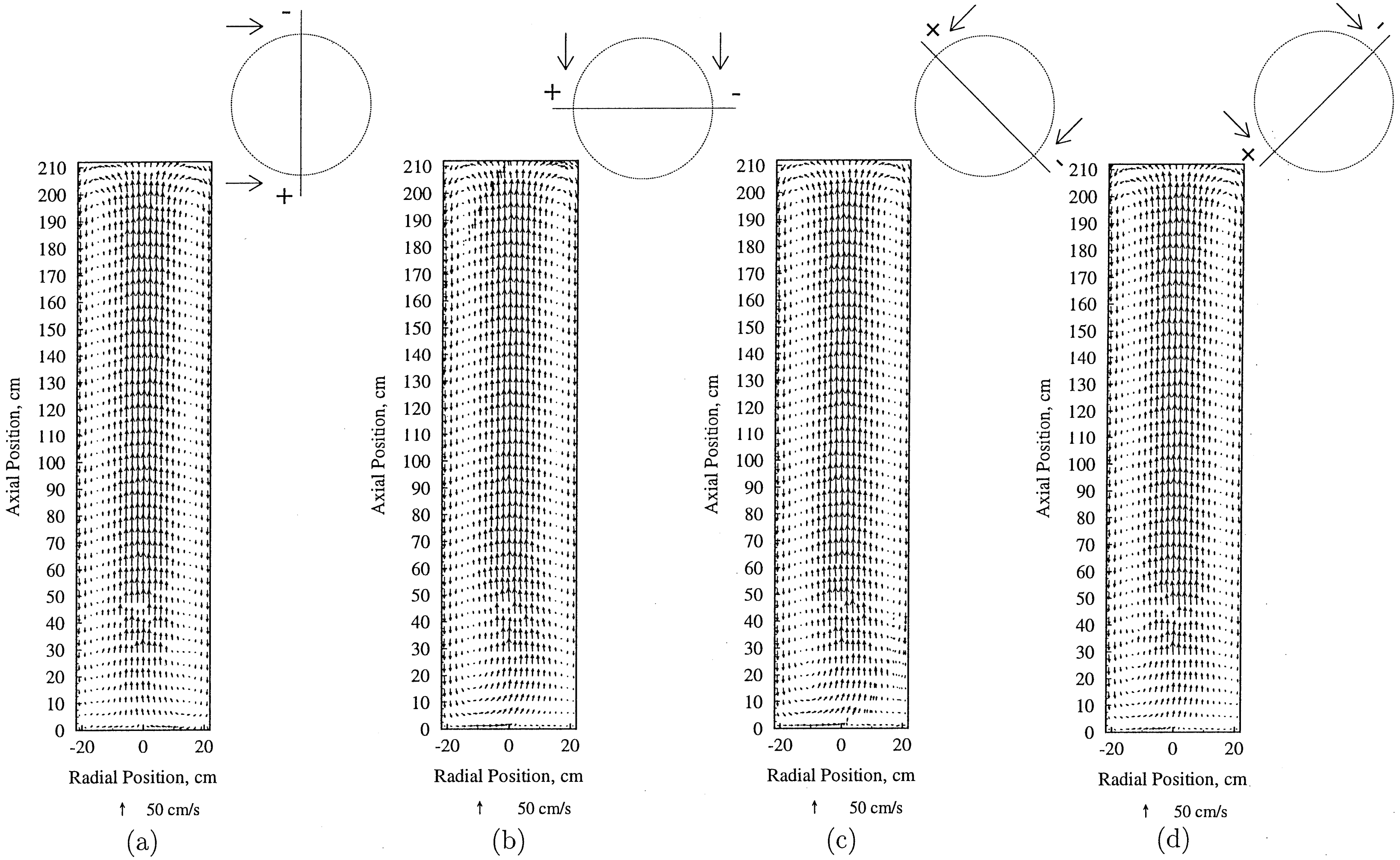

(a) (b) (c) (d)

Figure 4.33: Velocity Vector Plots (Longitudinal Views) for Col. Dia. 44 cm, Distributor: Perforated Plate **18A**, $U_g = 10.0$ cm/s

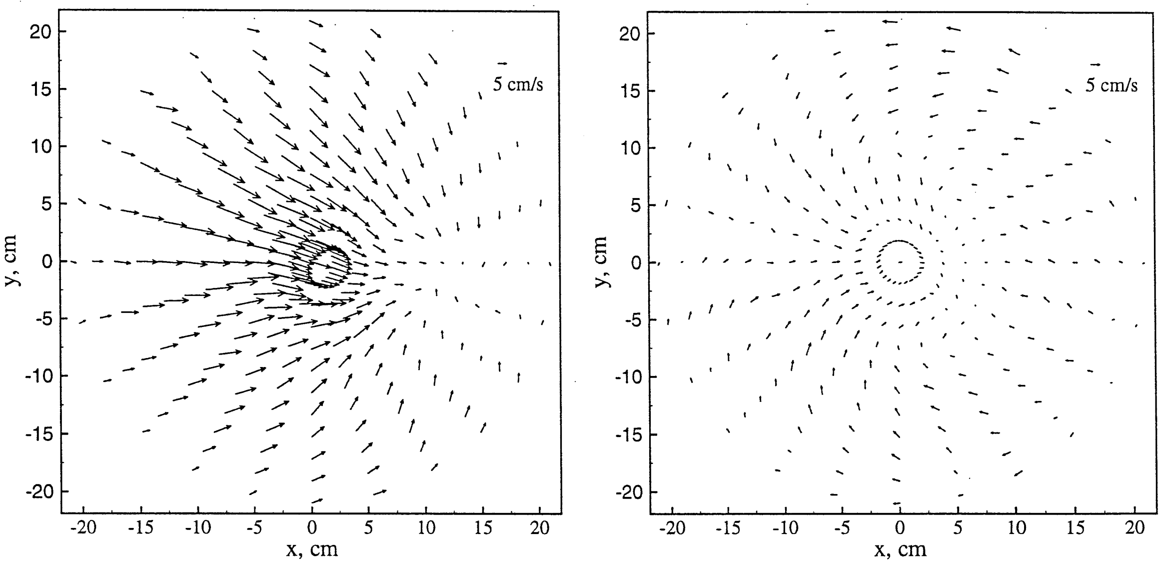

(a) z = 5 cm

(b) z = 25 cm

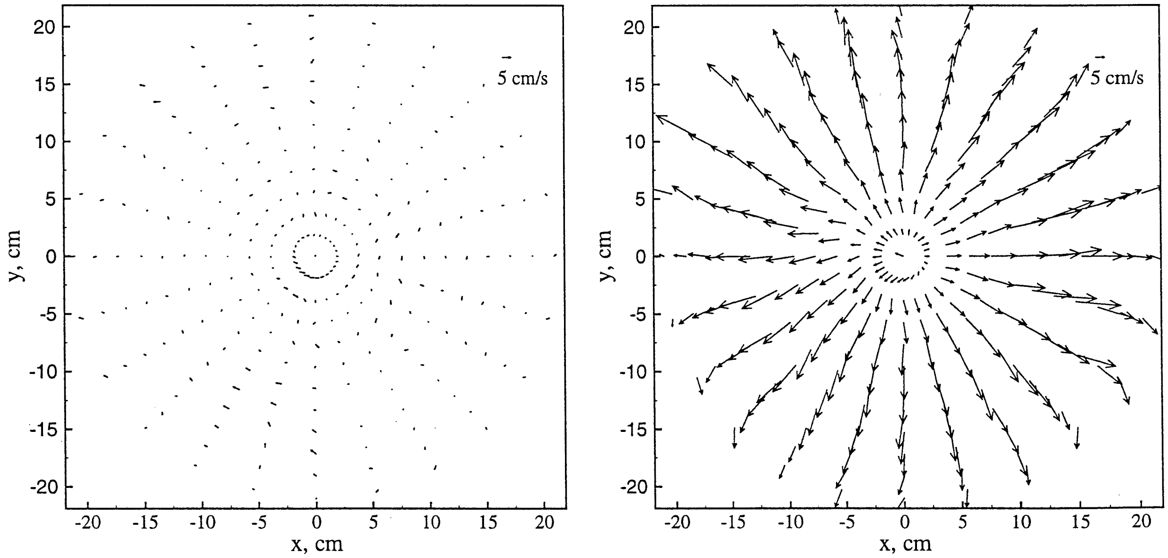

(c) z = 130 cm

(d) z = 210 cm

Figure 4.34: Velocity Vector Plots (Cross-sectional Views) for Column Diameter 44 cm, Distributor: Perforated Plate (**18A**), U_g = 10.0 cm/s

4.2.4 Distributor Effects

It is evident, based on the present results, that the type of distributor affects the flow pattern, especially close to the distributor, resulting in varying degrees of asymmetry about the axis of the column. This asymmetry is pronounced for perforated plate distributors at low superficial gas velocity, and can be attributed to the non-uniformity of the holes in the perforated plate. The distributor with the smallest size holes (**8A** in the 19 cm column) results in multiple recirculation cells, which persist up to higher gas velocities. The 14 cm column with distributor **6A**, of hole size 0.4 mm, shows strong asymmetry at the lower gas velocities, but there is no evidence of multiple circulation cells. At higher velocities, in the churn-turbulent flow regime with distributor **6A**, and for all the operating conditions with distributor **6B**, the asymmetry in the flow near the distributor manifests itself as two roller like structures. In these structures liquid flows toward the center along one direction and outward (as if it were squeezed out) in the perpendicular direction. The directional preference of these roller patterns seems to be consistent for all cases, i.e., liquid moving toward the center of the column along the x axis, and outward along the y axis. In this region the magnitude of the time averaged velocities is relatively low. For the larger size column (44 cm) there exists a typical asymmetry near the distributor, similar to the low gas velocity conditions in the 14 cm column with distributor **6A**.

For the experiments in the smaller columns, of diameters 14 cm and 19 cm, since the aspect ratio of the column is quite high (7 to 9), there is sufficient dispersion height (axial distance) in the column for the asymmetry that is created near the distributor to disappear. In these columns, the results show that the time averaged flow pattern completely recovers from the asymmetry at higher axial levels in the column. However, in the large column (44 cm), where the aspect ratio is relatively low (4.5), there is not enough dispersion height for the flow to become perfectly symmetric, especially at the lower gas velocities of 2 cm/s and 5 cm/s (Figures 4.29 and 4.31). At the highest gas velocity of 10 cm/s, the flow tends to axisymmetric behavior toward the top section of the column near the disengagement zone. Since it is evident that the asymmetry is caused by the distributor, it is expected that for the 44 cm diameter column, such an asymmetry in the time averaged flow will eventually disappear with axial position, for larger aspect ratio columns. Further experiments with larger aspect ratios (of at least 8) are warranted to show this conclusively.

4.2.5 Instantaneous Velocities

The flow patterns discussed so far represent the time averaged flow field, obtained by ensemble averaging of the instantaneous velocity data. Using the instantaneous velocities measured at a given location (compartment), the distribution of the instantaneous velocities about the mean value at that location (compartment) can be obtained. Figure 4.35 shows the histograms (or probability density function, 'pdf') of the instantaneous velocities, u_r, u_θ and u_z, at three radial locations in a 14 cm diameter column (distributor **6A**) at a superficial gas velocity of 2.4 cm/s. The pdf's at all the locations are close to Gaussian in shape, indicating a normal distribution of the instantaneous velocity along each direction, which is characteristic of turbulence in the system. Such an observation has been made by Groen et al (1996) who used LDA to measure the instantaneous liquid velocities in a 15 cm air-water bubble column. Both the radial and azimuthal velocities, in Figure 4.35, are shown to have a mean close to zero at all radial positions. For the axial velocity the mean changes from about 10 cm/s at $\xi = 0.06$ to -10 cm/s at $\xi = 0.94$. The spread in the pdf, for this case, is almost the same for the radial and azimuthal velocities, and is slightly higher for the axial velocity. However in Figure 4.36 which shows the pdf's in a 14 cm column at a gas velocity of 12 cm/s, the spread in the pdf's is much higher, especially in the axial direction where the instantaneous velocities range from -100 to +100 cm/s, depending on the radial location. The spread in the pdf about its mean, is an indication of the intensity of turbulence along each direction. These results are in agreement with the turbulence measurements from CARPT, which are discussed later on in this Chapter.

(a) Radial Velocities

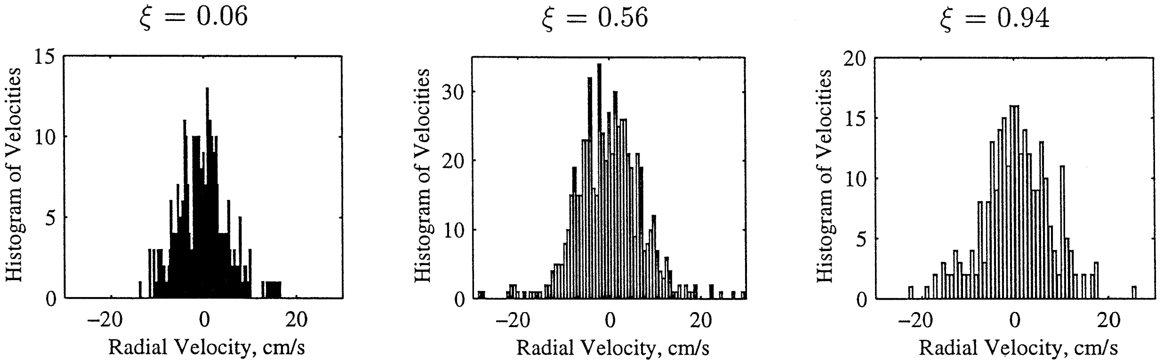

(b) Azimuthal Velocities

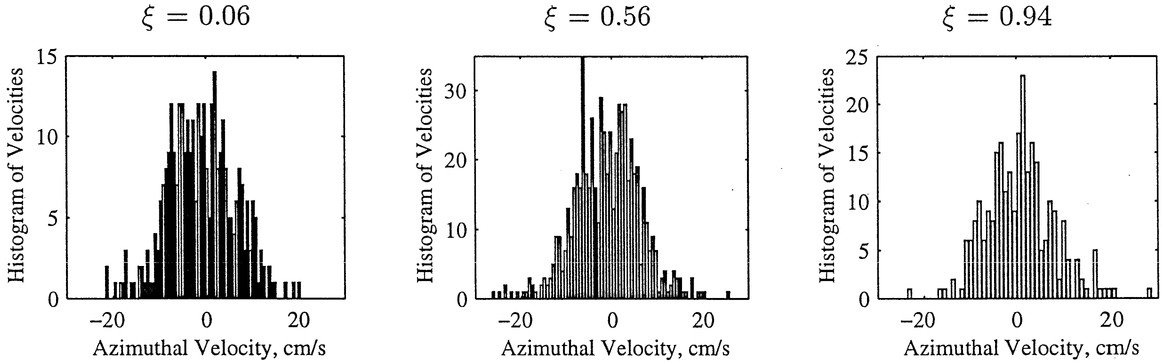

(c) Axial Velocities

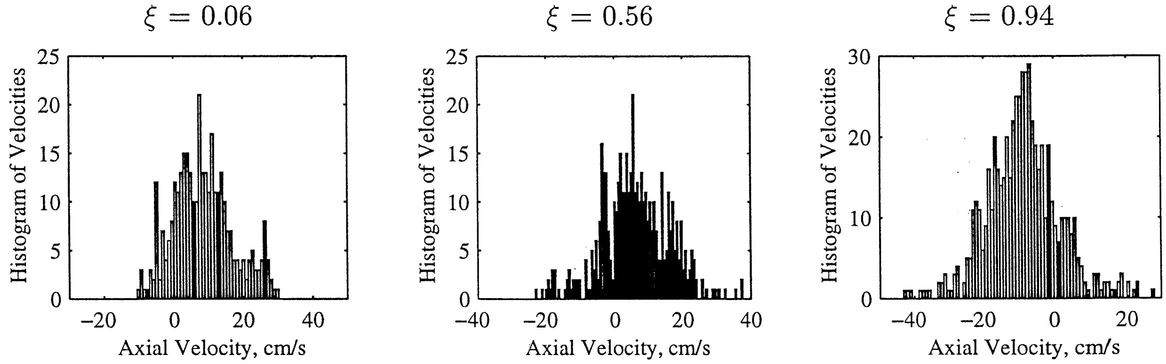

Figure 4.35: Histograms or Probability Density Functions (pdf) for the Instantaneous Velocities in a 14 cm Column, U_g = 2.4 cm/s, z = 90.0 cm, $\theta = 0^0$, (a) Radial, (b) Azimuthal, (c) Axial

(a) Radial Velocities

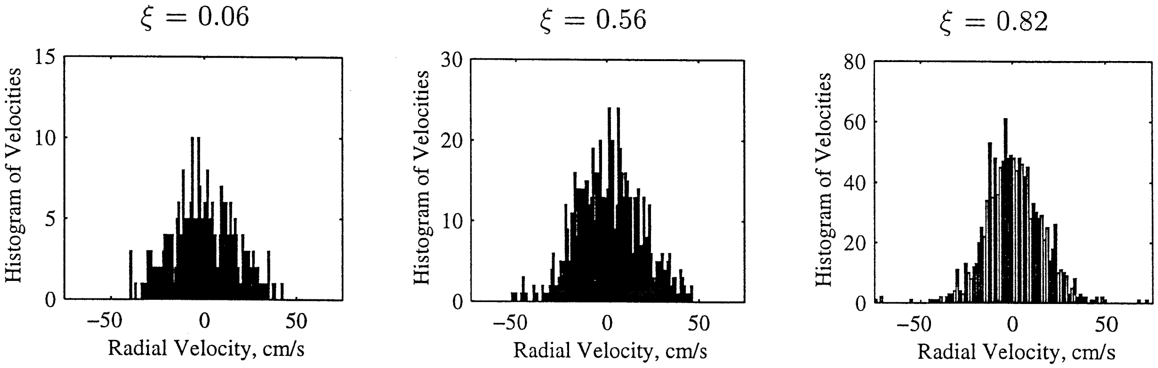

(b) Azimuthal Velocities

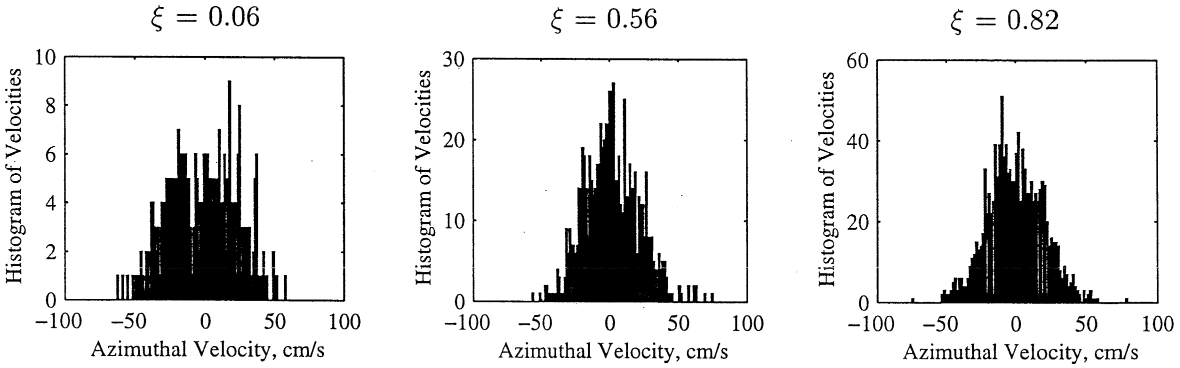

(c) Axial Velocities

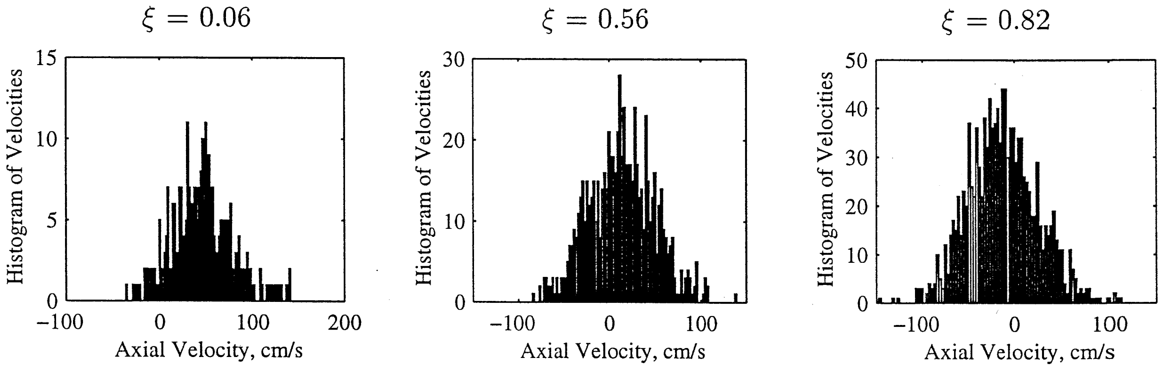

Figure 4.36: Histograms or Probability Density Functions (pdf) for the Instantaneous Velocities in a 14 cm Column, $U_g = 12.0$ cm/s, $z = 70.0$ cm, $\theta = 90^0$, (a) Radial, (b) Azimuthal, (c) Axial

4.2.6 Summary

The above results, based on a three dimensional interpretation of the time averaged flow field, show that there is a statistically stationary flow pattern in bubble columns, away from the end zones (distributor and disengagement zone) where a time averaged recirculating velocity profile is seen. The general observation is that in this region the axial liquid velocities dominate (15 cm/s to 60 cm/s), and the radial and azimuthal velocities are negligible (≤ 1 cm/s), and can be considered to be zero. For the columns with large aspect ratio (≥ 7), symmetry exists with respect to the column axis in this region. However, near the distributor zone, a symmetric flow pattern about the column axis is absent. The extent of asymmetry seems to depend on the distributor used. The asymmetry in the time averaged flow in this region is therefore attributed to the influence of the distributor. For most cases in the middle well developed region of the column, the axial variation of the time averaged velocities is not significant.

With regard to the fundamental modeling of multiphase flows in bubble columns, the above results suggest that, if possible, the distributor effects and the resulting asymmetry can only be captured using three dimensional models. Some of the important questions are: does there exist a perfectly symmetrical flow pattern at the distributor? If so, for what type of distributor, and how does it affect the resulting flow pattern in the entire column? How important are these effects in the prediction of phase and flow distribution in the column using fundamental models? This is an especially relevant question for the conditions of low gas velocities, wherein the asymmetry at the distributor tends to cause a bias in the flow pattern for quite large distances downstream, inducing larger downward velocities along one side of the column. Another question is, will the roller like patterns observed at the higher gas velocities investigated in this work persist on further increasing the inlet gas velocity? Answering the above questions requires further experimental work using different types of distributors and columns with larger aspect ratios, along with modeling efforts using three dimensional codes.

Further interpretation of the data with regard to the effects of distributor, gas velocity and column diameter is based on the one dimensional velocities (discussed in Chapter 4.4), where the axial liquid velocities are azimuthally and axially averaged in the middle section of the column. The axial levels, L_{min} and L_{max}, between which the axial averaging is done vary from run to run (Table 4.1). L_{min} and L_{max} are selected by considering the range of axial locations over which there is minimal axial variation of the time averaged axial velocities, with negligible radial and azimuthal velocities.

4.3 Liquid Turbulence

The proper understanding and modeling of turbulence forms an important aspect of modeling gas-liquid flows (Jakobsen 1993; Jakobsen et al. 1996). In bubble columns, the instantaneous flow behavior is highly transient. Visual observation of the flow indicates the presence of large scale structures or eddies that are generated by the passage of bubbles through the column, resulting in recirculation or 'gulf streaming' of the liquid phase.

Since turbulence is characterized by random fluctuations, the natural and most direct way of studying the flow is by studying and characterizing the statistics of the flow parameters (Monin and Yaglom 1965; Wilcox 1994). This gives rise to the mean or the time averaged quantities, such as the time averaged phase velocities. The statistical information about the instantaneous behavior of the system is then obtained from higher order correlations of the fluctuating quantities that represent the turbulent interactions. In such a type of representation, all the scales of turbulence are grouped and quantified together.

Modeling the flow in terms of the averaged equations gives rise to second order (and higher order) correlations between the fluctuating quantities. The second order velocity correlations, $\overline{u_i'u_j'}$, represent one part of the turbulent interactions. These terms can be visualized as effecting the transport of momentum along the i^{th} direction due to the instantaneous flow in the j^{th} direction, or vice-versa, and therefore give rise to the symmetric turbulent stress tensor, or Reynolds stresses, defined in cylindrical coordinates as:

$$\tau = \rho_l \begin{pmatrix} \overline{u'_r u'_r} & \overline{u'_r u'_\theta} & \overline{u'_r u'_z} \\ \overline{u'_\theta u'_r} & \overline{u'_\theta u'_\theta} & \overline{u'_\theta u'_z} \\ \overline{u'_z u'_r} & \overline{u'_z u'_\theta} & \overline{u'_z u'_z} \end{pmatrix} \tag{4.5}$$

Traditionally the definition of the turbulent Reynolds stresses as they appear in the Navier-Stokes equations contain a negative sign on the right hand side of Equation 4.5. However, since the main emphasis of the present work is on experimental measurements and in understanding some of the mechanisms involved in gas-liquid flows in bubble columns, the negative sign is omitted. This is in agreement with the presentation of experimental measurements of the stresses ($\rho_l \overline{u'_i u'_j}$) in the literature (Schlichting 1960; Franz et al. 1984; Menzel et al. 1990; Mudde et al. 1997). There are six unknowns in the turbulent stress tensor, the normal stresses, $\rho_l \overline{u'_r u'_r}$, $\rho_l \overline{u'_\theta u'_\theta}$ and $\rho_l \overline{u'_r u'_r}$, and the shear stresses $\rho_l \overline{u'_r u'_\theta}$, $\rho_l \overline{u'_r u'_z}$ and $\rho_l \overline{u'_\theta u'_z}$. Related to the turbulent normal stresses is the turbulent kinetic energy, k, defined per unit volume as

$$k = \frac{1}{2}\rho_l(\overline{u'^2_r} + \overline{u'^2_\theta} + \overline{u'^2_z}) \tag{4.6}$$

Here after, k will be referred to as the turbulent kinetic energy although it is implied to be the turbulent kinetic energy per unit volume.

Using the CARPT technique, it is possible to measure all the above quantities in the entire three dimensional flow field of a bubble column. In the following section the three dimensional variation of the turbulence quantities in the column is studied, with the specific focus on the middle section of the column, in order to assess the distribution of each of these quantities in space. This analysis is presented only for a few sample cases, to give a general idea about the behavior of the various stresses. Following this, the effects of operating conditions, distributor type and column size are analyzed using the axially and azimuthally averaged turbulence parameters.

4.3.1 3-D Analysis of Data

Similar to the case of the time averaged velocities, the experimental data from CARPT for the various turbulence parameters in a three dimensional flow field is visualized using TECPLOT, by obtaining longitudinal slices along four directions, 0^o - 180^o, 45^o - 225^o, 90^o -270^o and 135^o - 315^o. The results are presented as contour plots using a gray scale gradation. The results shown in Figures 4.37 to 4.43 are for the 14 cm column diameter with distributor **6A**, at a superficial gas velocity of 12 cm/s. In general, these results are representative of the results obtained under all conditions in the different column diameters studied. Some specific aspects can be related to the time averaged flow patterns, shown in the previous section.

Figures 4.37, 4.38 and 4.39 show the contour plots for the normal stresses, τ_{rr}, $\tau_{\theta\theta}$ and τ_{zz}. Common to all the figures is that the results show good symmetry about the column axis (within experimental error of $\sim$ 10 to 15 %). This is the general trend observed for almost all the cases studied and suggests that there is no variation of the turbulence quantities with angular position, which is similar to the time averaged flow pattern. With regard to axial variation, it appears that, within experimental error, the stresses are quite uniform with axial position in the middle section of the column. Considering the radial variation of the normal stresses, the radial normal stresses have a maximum in an annular region close to the axis of the column, but show a dip at the axis itself. On the other hand, the angular stresses seem to peak at the axis of the column. Such trends are suspected to arise due to the artifact of the cylindrical coordinates, and are discussed in the following section, where the radial variation of the fluid dynamic parameters are considered in greater detail. The axial normal stresses have higher values in the annular portion of the column, although the radial variation is not so distinct.

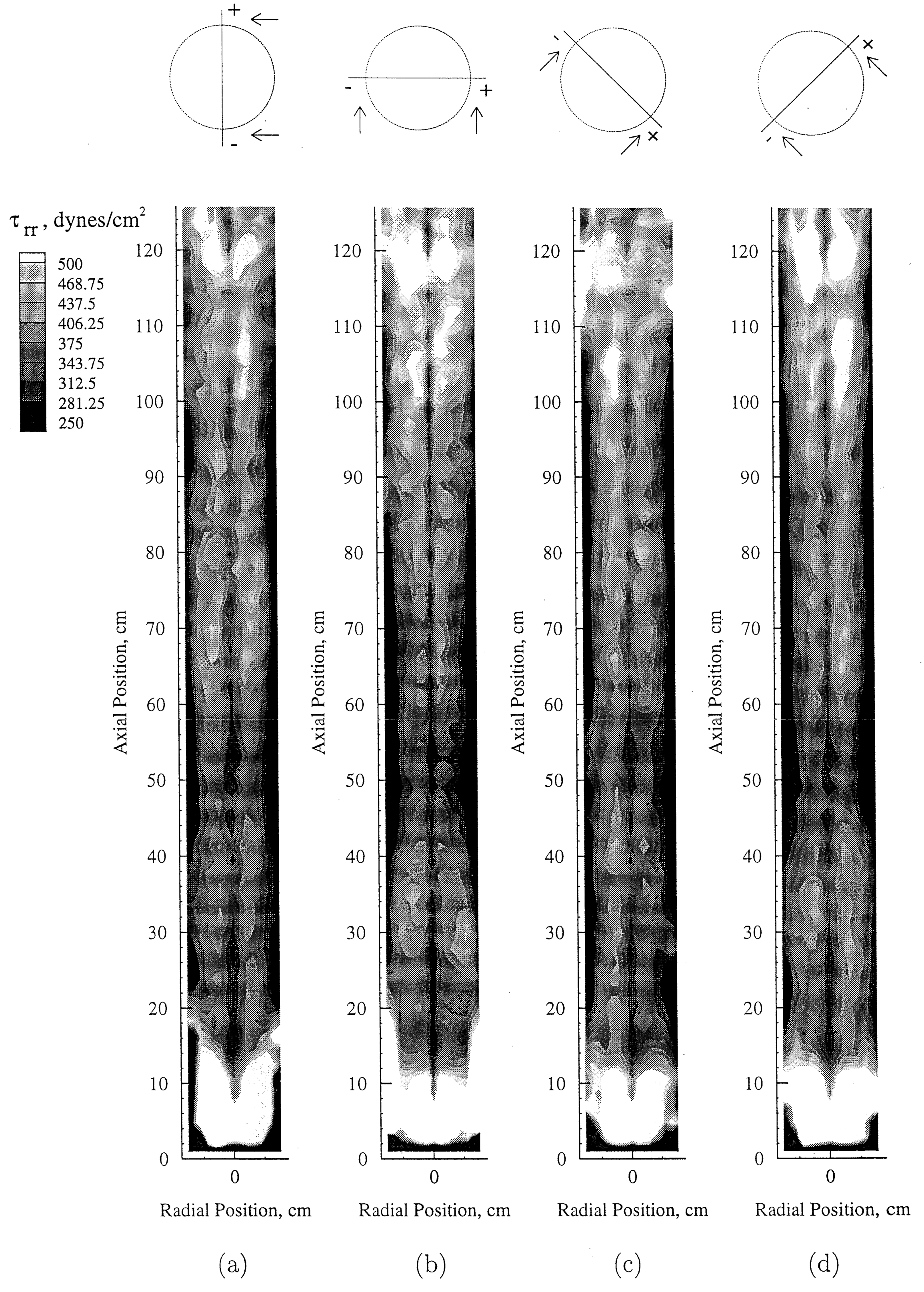

Figure 4.37: Radial Turbulent Normal Stress (Longitudinal Views) for Column Diameter 14 cm, Distributor: Perforated Plate **6A**, $U_g = 12.0$ cm/s

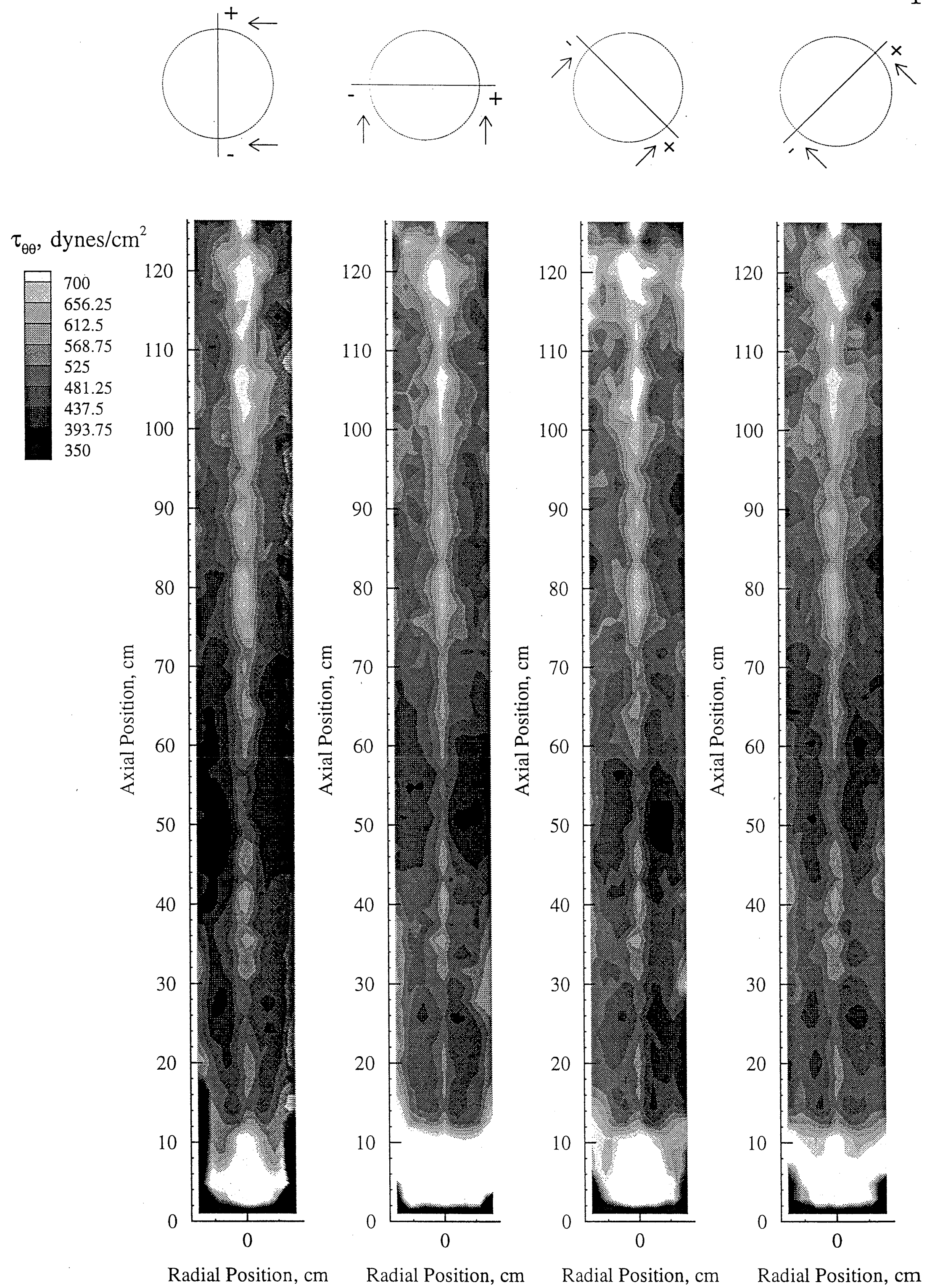

(a) (b) (c) (d)

Figure 4.38: Azimuthal Turbulent Normal Stress (Longitudinal Views) for Column Diameter 14 cm, Distributor: Perforated Plate **6A**, $U_g = 12.0$ cm/s

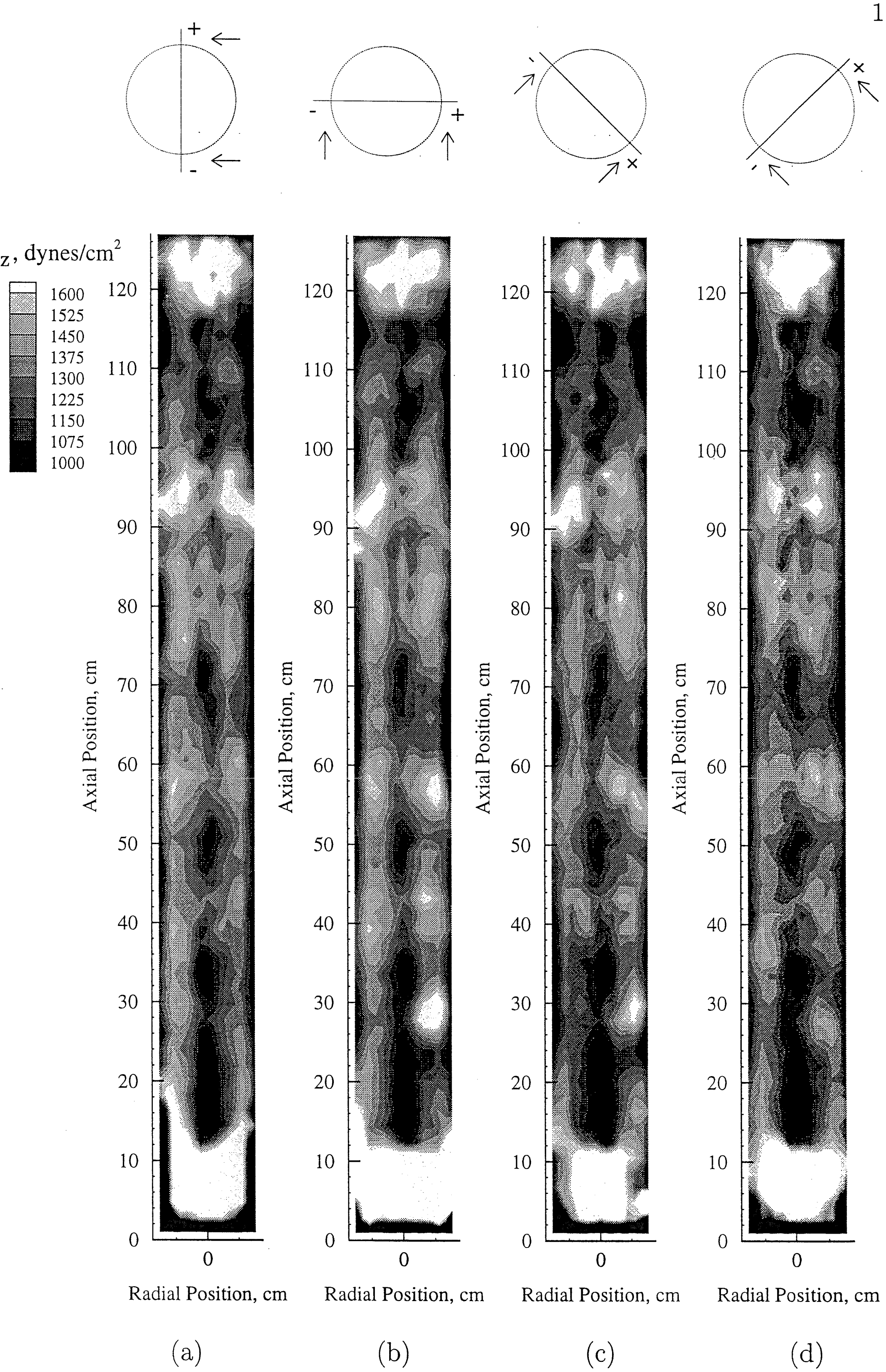

Figure 4.39: Axial Turbulent Normal Stress (Longitudinal Views) for Column Diameter 14 cm, Distributor: Perforated Plate **6A**, $U_g = 12.0$ cm/s

The turbulent shear stress, τ_{rz}, is rather uniform, both axially and along the azimuthal direction, in the middle section of the column (Figure 4.40). Radially, τ_{rz} peaks in the annular region of the column, showing a more pronounced variation than the axial normal stress. The shear stresses involving the angular velocities, i.e., $\tau_{\theta r}$ and $\tau_{\theta z}$, are relatively small in magnitude, as seen from Figures 4.41 and 4.42. The patterns in Figures 4.41 and 4.42 have no physical significance, since the variation of values shown are within experimental error of the measurements. The average value of $\tau_{\theta r}$ and $\tau_{\theta z}$ is close to zero. The contour plot for the turbulent kinetic energy shown in Figure 4.43 indicates trends similar to the axial normal stress.

Results for all the normal stresses and the turbulent kinetic energy indicate higher values very close to the distributor. These values are about two to three times larger than the corresponding average values in the middle section of the column, indicating high degree of turbulence in the inlet section. The error in the results for the turbulence parameters at the distributor are also higher than in the main section of the column, as discussed in Chapter 3. Hence, an accurate quantitative estimate of the stresses at the distributor (within 10 cm of the distributor) cannot be obtained. Such an estimate would be valuable, since it has been shown that the inlet value of the kinetic energy is important in modeling multiphase flows (Sannaes 1997; He and Simonin 1994). In the $k - \epsilon$ model formulation for modeling multiphase flows an arbitrary value is usually set as the inlet condition for k, which is a function of the mean liquid and gas phase velocities at the inlet (Jakobsen 1993).

The above discussed results are representative of the cases where the time averaged flow pattern is well developed in the middle section, with the least amount of asymmetry at the distributor (typical for the high superficial gas velocity conditions). For situations where the time averaged velocities exhibit strong asymmetry close to the distributor, this is also reflected to some extent in the patterns for the turbulence parameters. Figures 4.44 and 4.45 show the axial normal stress, τ_{zz}, and the shear stress, τ_{rz} in a 19 cm diameter column at a superficial gas velocity of 2.0 cm/s.

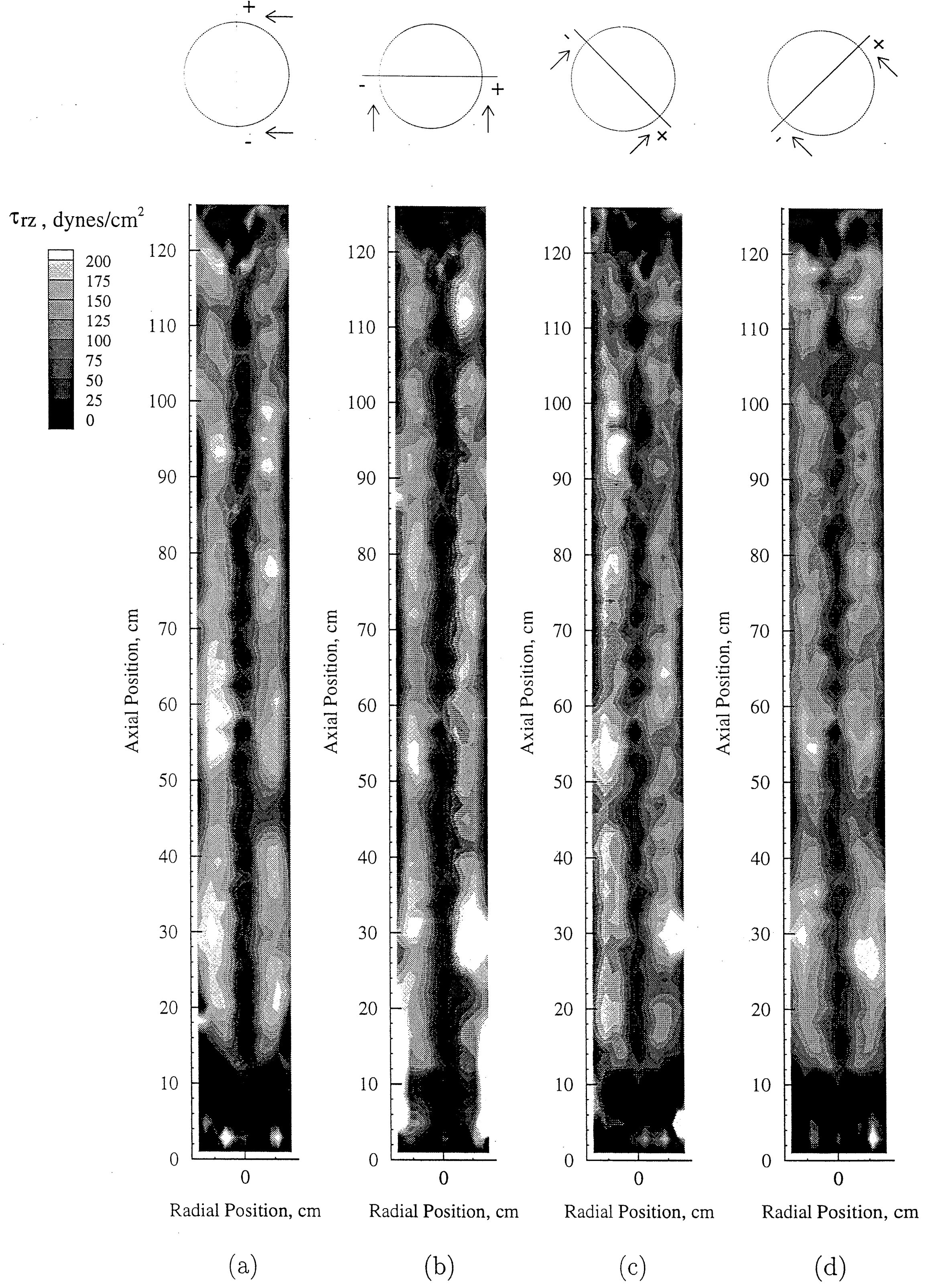

(a) (b) (c) (d)

Figure 4.40: Reynolds Shear Stress,τ_{rz}, (Longitudinal Views) for Column Diameter 14 cm, Distributor: Perforated Plate **6A**, U_g = 12.0 cm/s

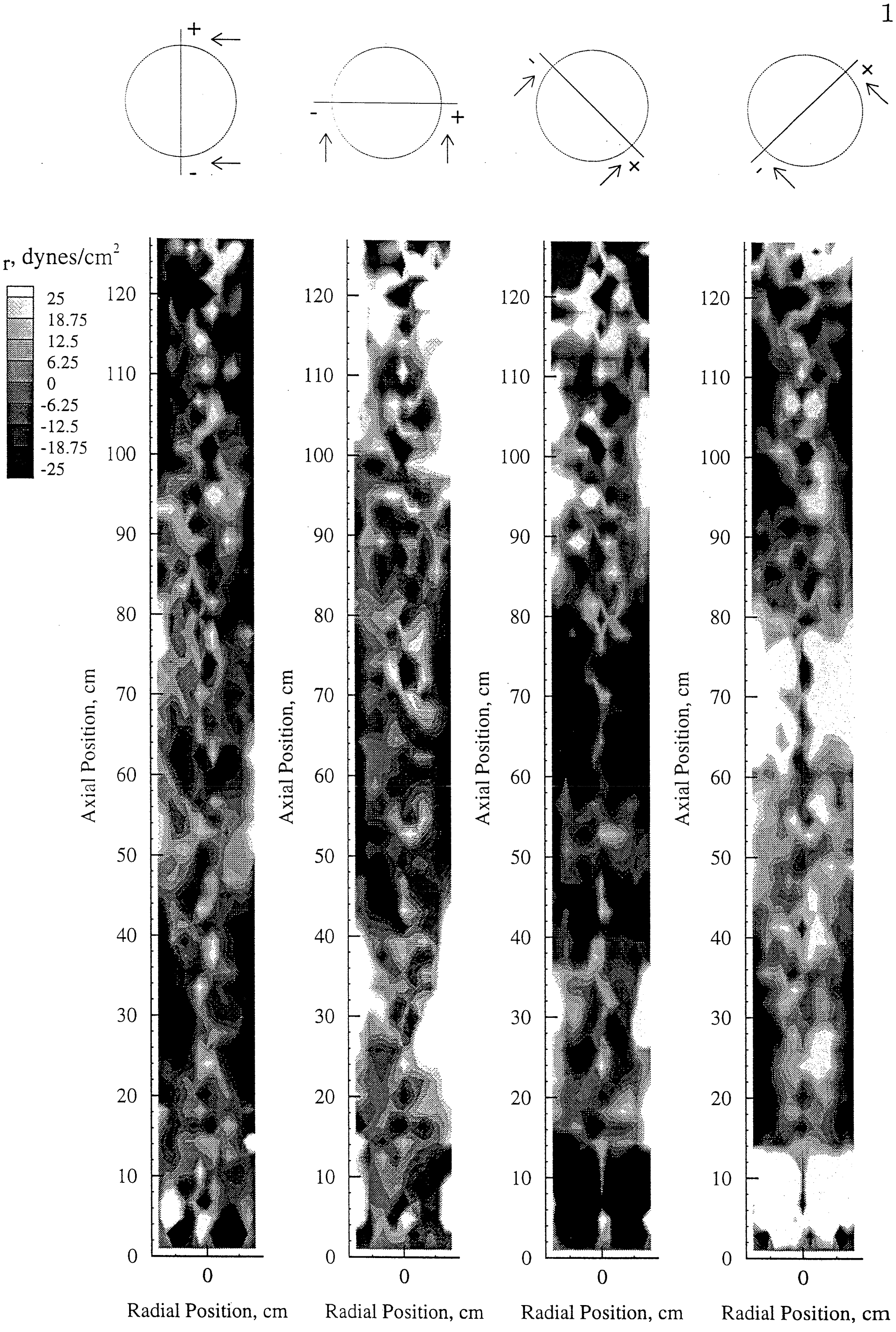

(a) (b) (c) (d)

Figure 4.41: Reynolds Shear Stress, $\tau_{\theta r}$, (Longitudinal Views) for Column Diameter 14 cm, Distributor: Perforated Plate **6A**, $U_g = 12.0$ cm/s

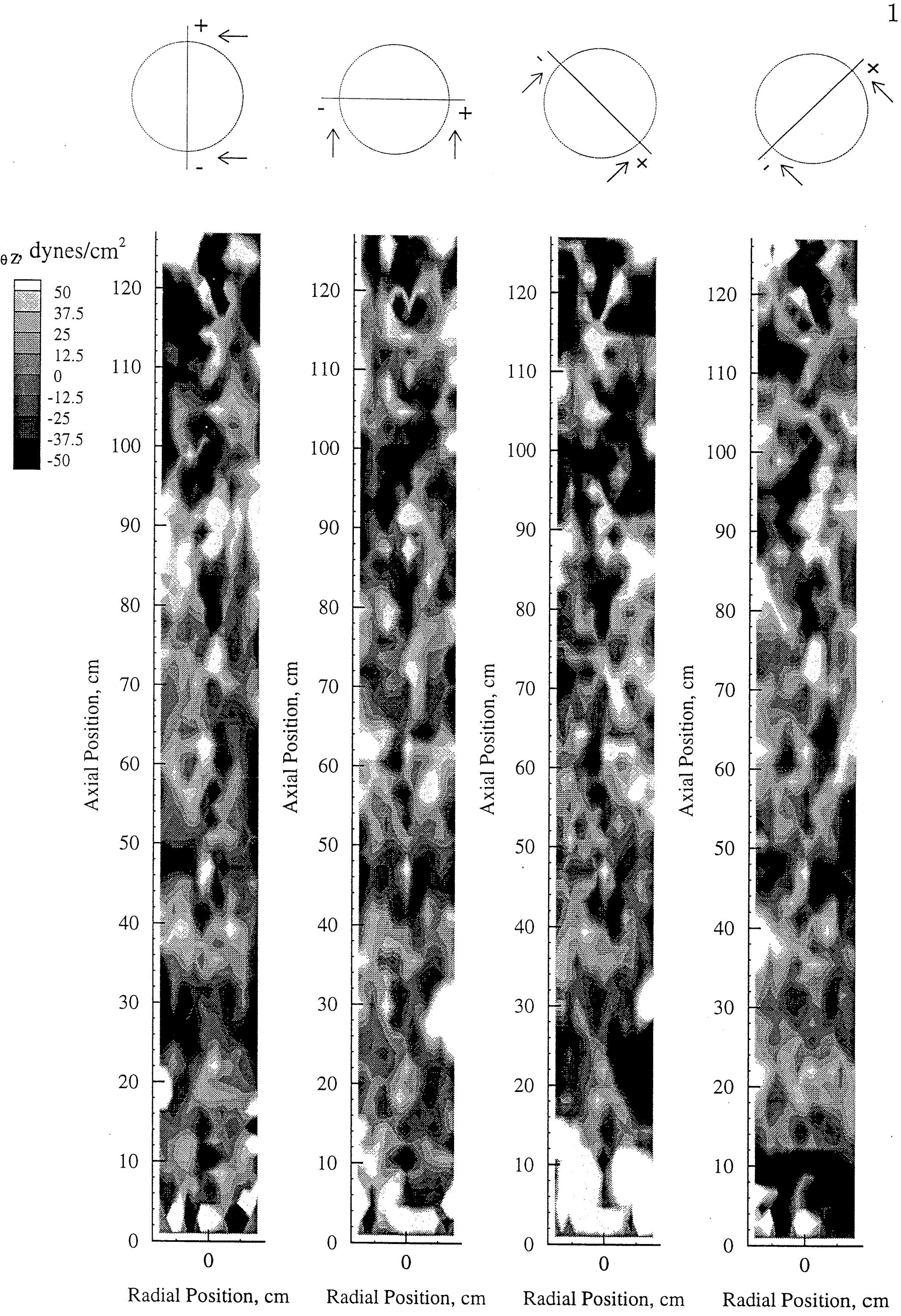

(a) (b) (c) (d)

Figure 4.42: Reynolds Shear Stress,$\tau_{\theta z}$,(Longitudinal Views) for Column Diameter 14 cm, Distributor: Perforated Plate **6A**, U_g = 12.0 cm/s

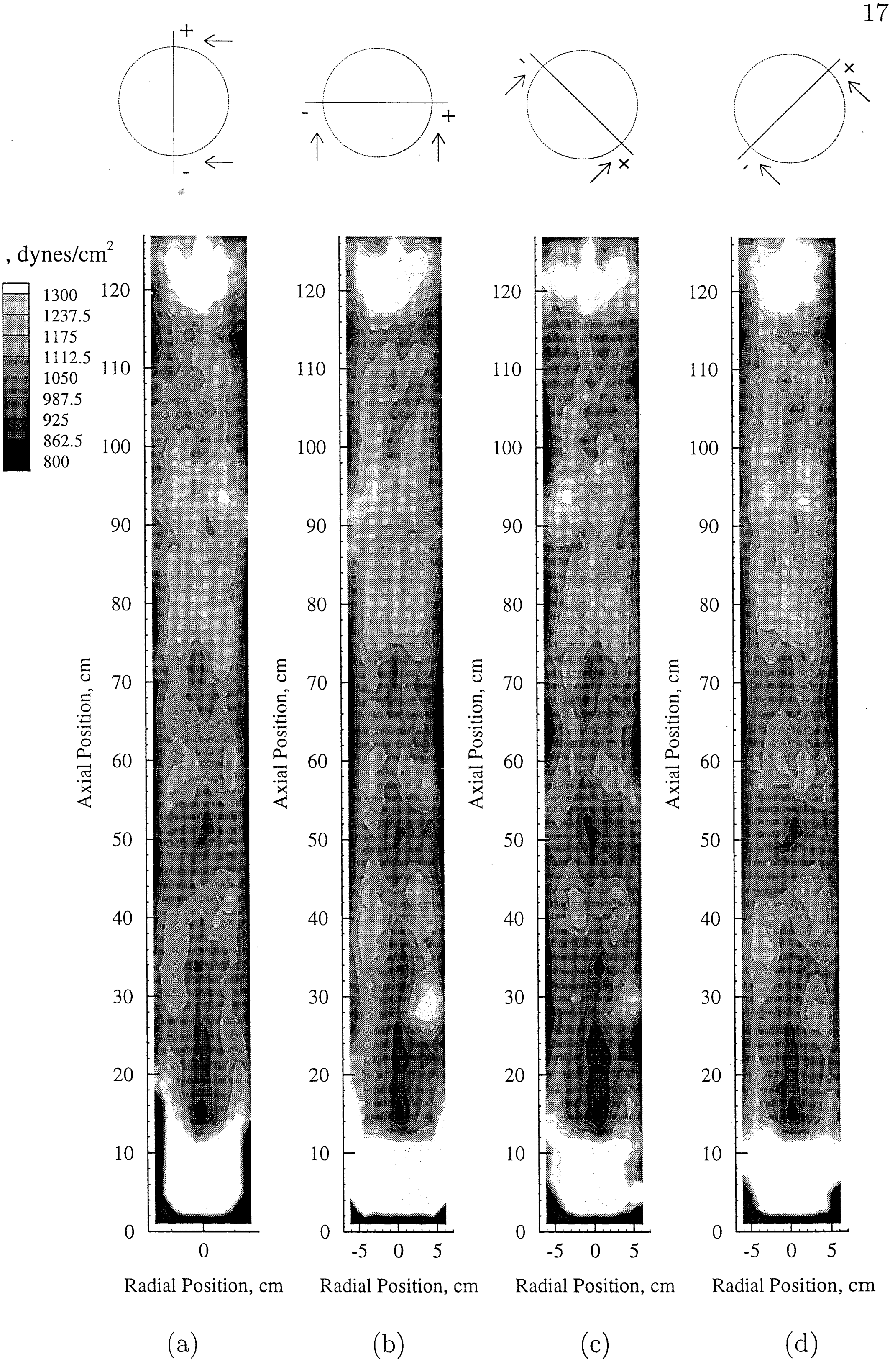

Figure 4.43: Turbulent Kinetic Energy, (Longitudinal Views) for Column Diameter 14 cm, Distributor: Perforated Plate **6A**, U_g = 12.0 cm/s

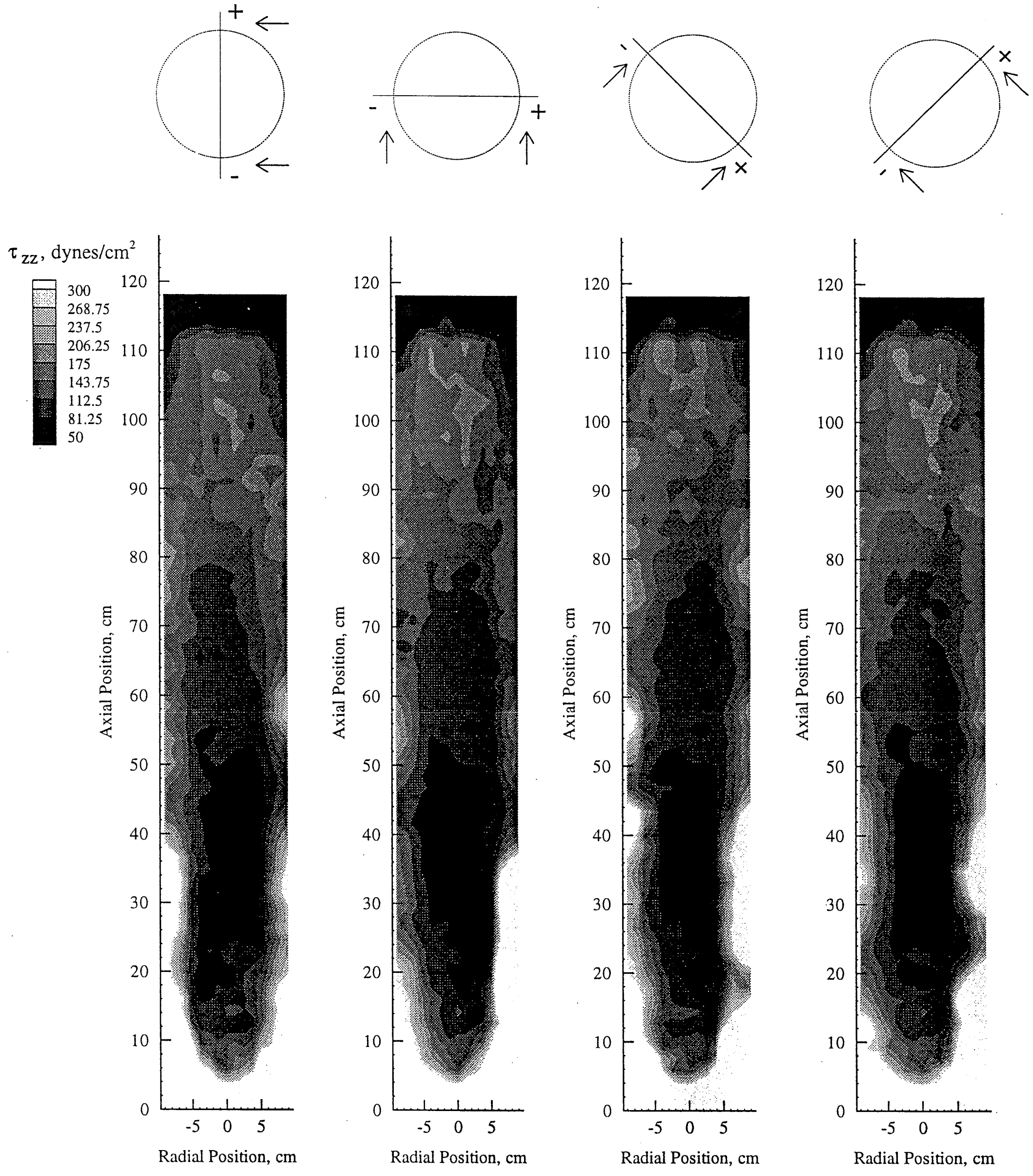

(a) (b) (c) (d)

Figure 4.44: Axial Turbulent Normal Stress (Longitudinal Views) for Column Diameter 19 cm, Distributor: Perforated Plate **8A**, U_g = 2.0 cm/s

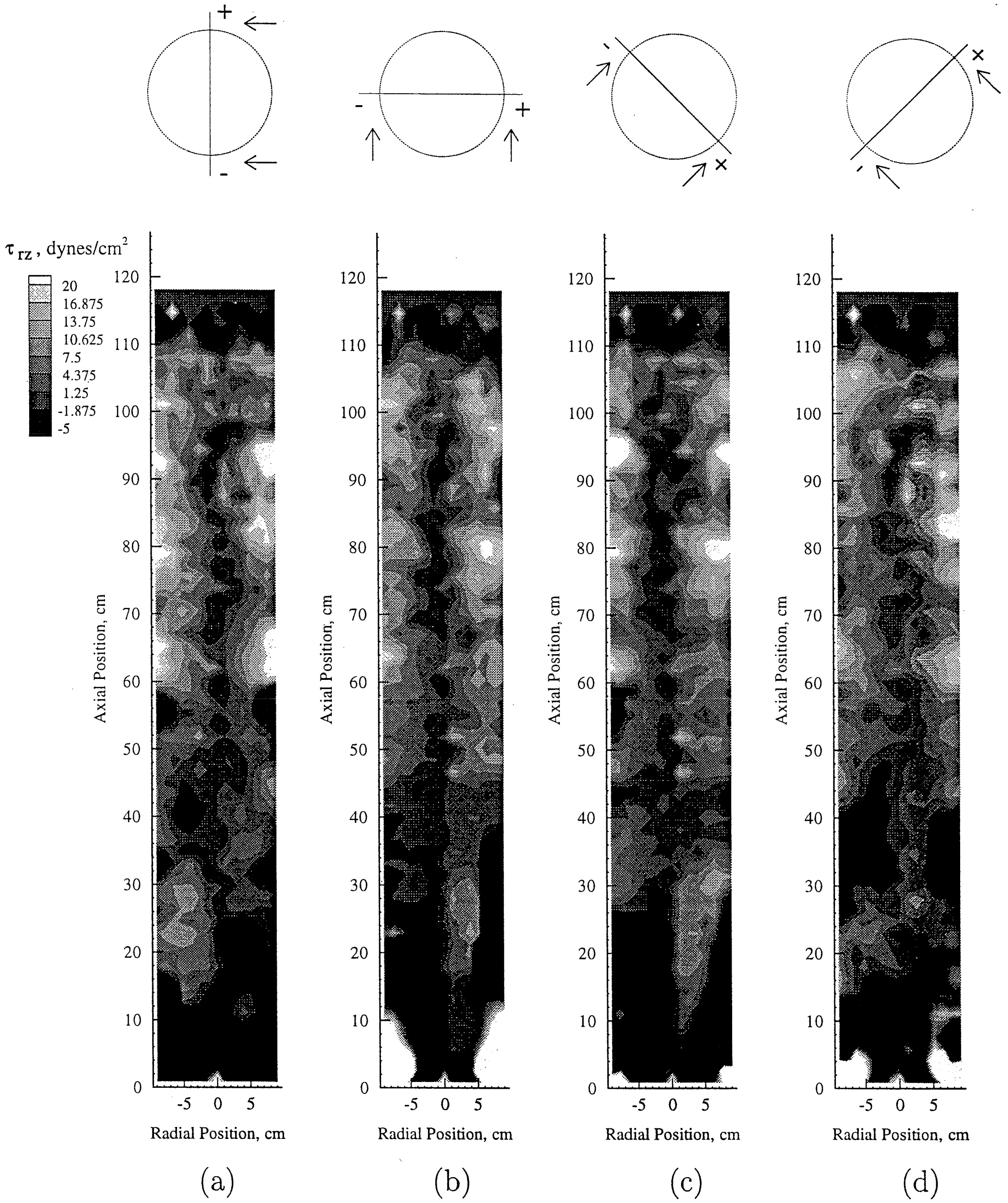

Figure 4.45: Reynolds Shear Stress, τ_{rz}, (Longitudinal Views) for Column Diameter 19 cm, Distributor: Perforated Plate **8A**, $U_g = 2.0$ cm/s

The bottom half of the column shows a certain degree of asymmetry, which seems to disappear at the higher sections, similar to the corresponding time averaged flow patterns. The asymmetry in the turbulence parameters is the strongest for the 44 cm column at 2 cm/s, in which pronounced asymmetry is observed for the time averaged velocities through out the length of the column.

Analysis of the results for the various turbulent stresses indicates that, in general, the turbulence parameters exhibit a symmetric behavior with respect to the column axis. In the middle section, the axial variation of the turbulence parameters is not very significant, and conforms with the behavior of the time averaged flow patterns. Hence for further analysis, the turbulence parameters are averaged azimuthally and axially in the middle section of the column (defined in Table 4.1). This enables an effective analysis of the data for the study of the effects of gas velocity, column diameter and distributor on the various fluid dynamic parameters.

4.4 One Dimensional Analysis of Data and Discussion of Results

4.4.1 Turbulence Parameters

There is considerable experimental evidence that turbulence (based on long time averaging) in bubble columns is not isotropic (Franz et al. 1984; Devanathan et al. 1990, Chen et al. 1994; Mudde et al. 1997). The normal stresses in the axial direction are much larger than in the radial and angular directions. Visual observation of the flow, especially under high superficial gas velocity conditions, indicates the presence of large scale structures that are generated by the passage of the gas bubbles and the subsequent bubble-wakes interaction. Since there is lesser restriction in the axial direction to the path of these structures, the length scales in the axial direction are significantly larger than in the radial direction, which is restricted by the diameter of the column. The diameter of the column also restricts the tangential velocities ($u_\theta = \frac{r\Delta\theta}{\Delta t}$) and therefore the azimuthal length scales.

In the previous section, contour plots of the various components of the Reynolds stress tensor were presented (Figures 4.37 to 4.42) that indicated the existence of symmetry in the column. Therefore in this section the axially and azimuthally averaged radial profiles of the various parameters are presented and discussed. The axial averaging of the parameters has been done between the levels L_{min} and L_{max} in the column, as indicated in Table 4.1.

Figures 4.46 to 4.53 show the six components of the turbulent stress tensor, as a function of radial position, under various operating conditions. For majority of the conditions the axial normal stresses are about 2 to 3 times higher than the radial and azimuthal normal stresses. The Reynolds shear stress, τ_{rz}, is much lower than the radial/angular normal stresses (by approximately half), while the shear stresses involving the angular fluctuating velocities, $\tau_{\theta r}$ and $\tau_{\theta z}$, are negligible and can be considered to be zero.

Although the angular and radial normal stresses are about the same order of magnitude, the angular normal stress is almost always higher than the radial normal stress. A distinct feature for conditions of high superficial gas velocities, in the churn turbulent flow regime (Figures 4.48, 4.49, 4.52 and 4.53), is that $\overline{u_\theta'^2}$ peaks at the center of the column. This suggests that the vortical structures spiraling up the column have a tendency to cross over the axis, especially at the higher gas velocities. Such a motion will induce large angular velocities (due to large changes in θ) despite the fact that the movement is along the center axis of the column (small values of r). This behavior of the eddies and vortex structures rules out the possibility of performing a transient simulation of flows in bubble columns using two dimensional axisymmetric codes since, under these circumstances, imposing a zero gradient at the centerline is not realistic and will contradict the existing physical picture of the flow. In addition, the transient three dimensional vortical structures cannot be captured in a two dimensional axisymmetric code due to the absence of the θ dimension.

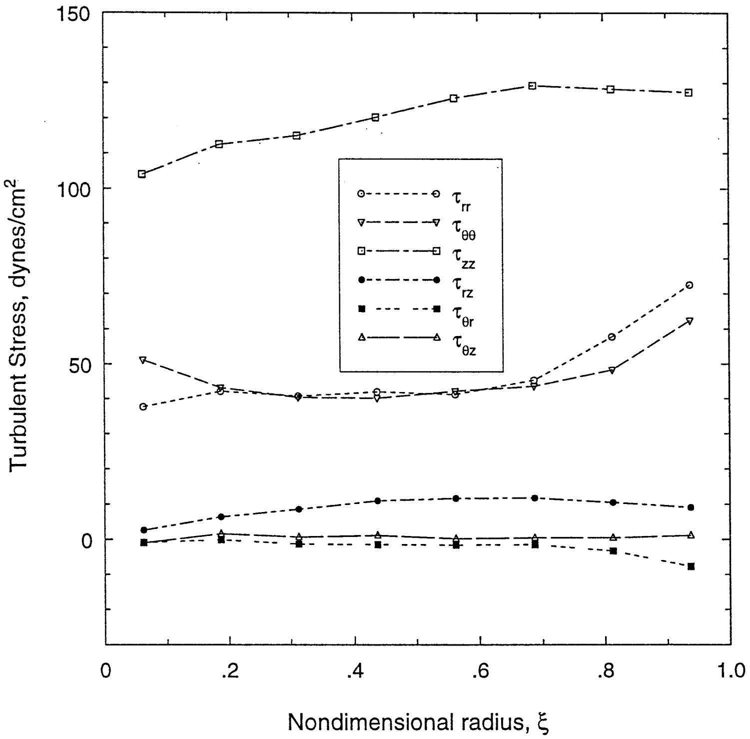

Figure 4.46: Components of the Turbulent Stress tensor, τ, in a 14 cm Diameter Column, Distributor: **6A**, $U_g = 2.4$ cm/s

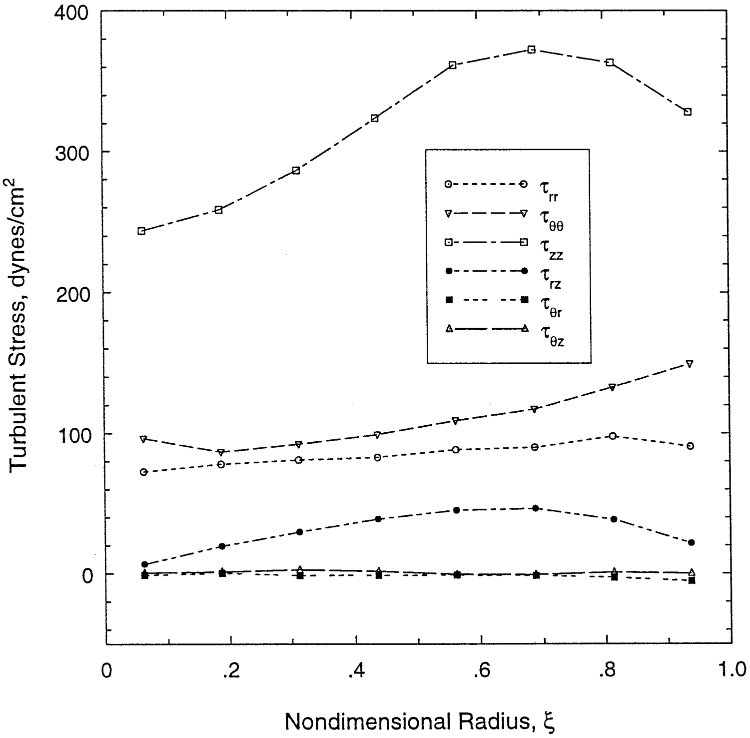

Figure 4.47: Components of the Turbulent Stress tensor, τ, in a 14 cm Diameter Column, Distributor: **6A**, $U_g = 4.8$ cm/s

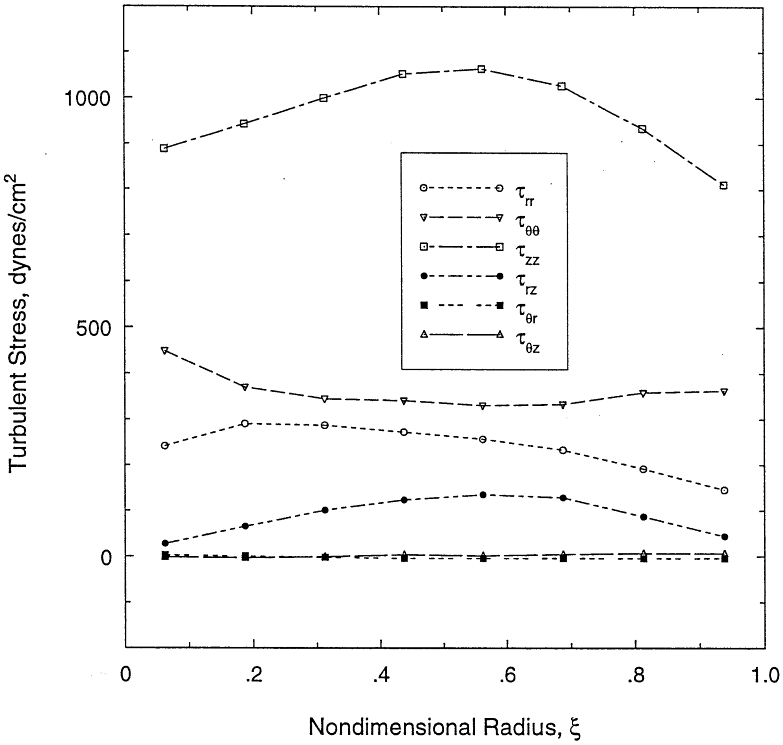

Figure 4.48: Components of the Turbulent Stress tensor, τ, in a 14 cm Diameter Column, Distributor: **6A**, $U_g = 9.6$ cm/s

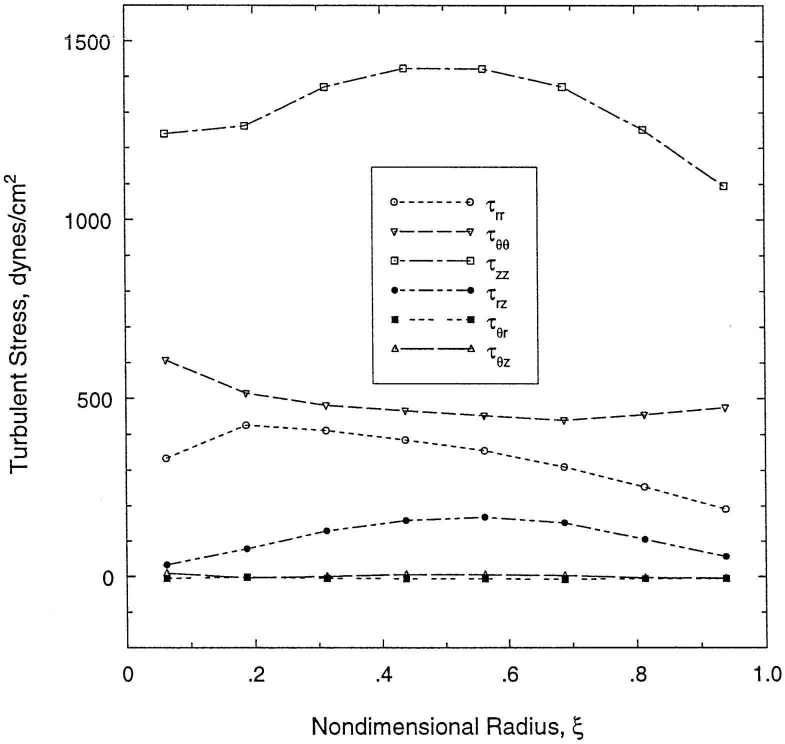

Figure 4.49: Components of the Turbulent Stress tensor, τ, in a 14 cm Diameter Column, Distributor: **6A**, $U_g = 12.0$ cm/s

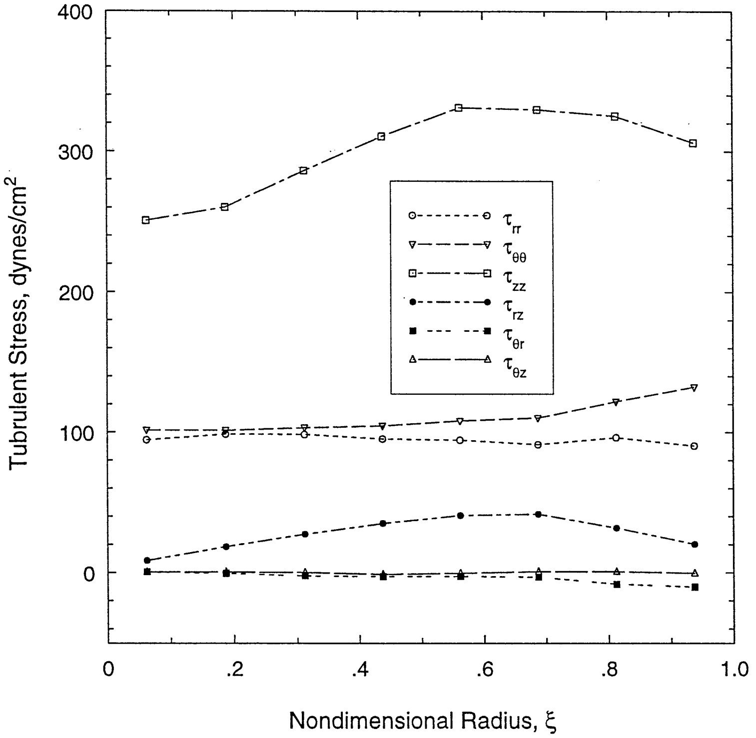

Figure 4.50: Components of the Turbulent Stress tensor, τ, in a 14 cm Diameter Column, Distributor: **6B**, $U_g = 2.4$ cm/s

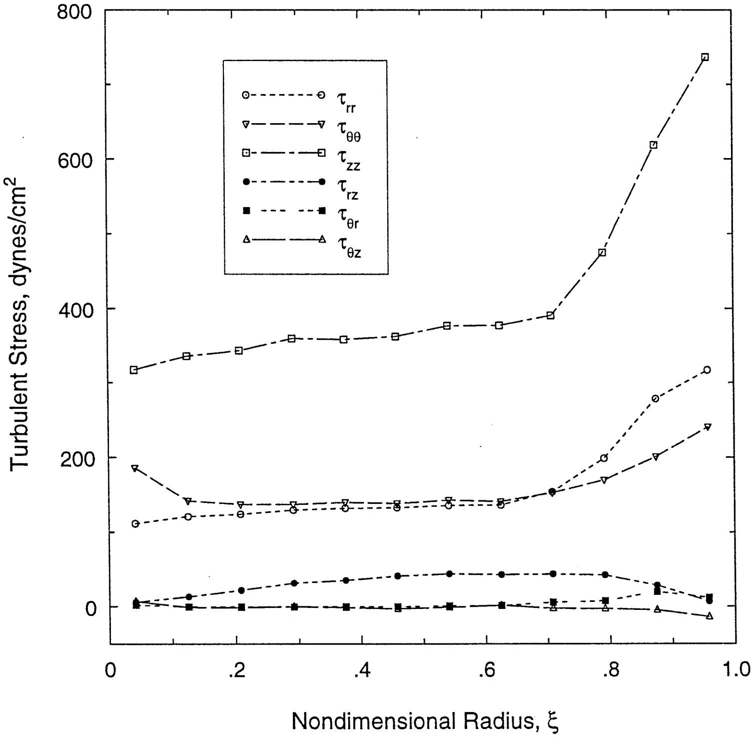

Figure 4.51: Components of the Turbulent Stress tensor, τ, in a 44 cm Diameter Column, $U_g = 2.0$ cm/s

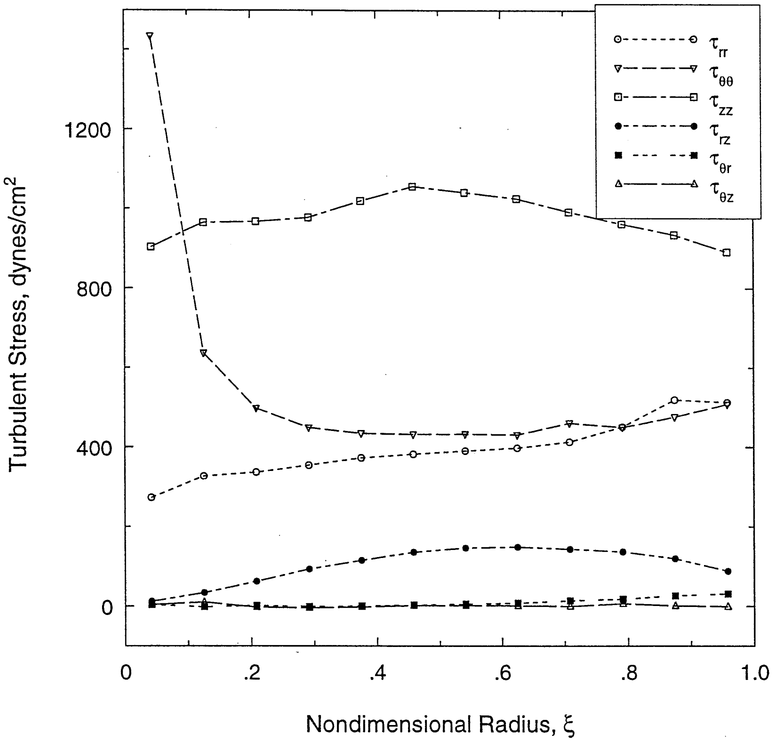

Figure 4.52: Components of the Turbulent Stress tensor, τ, in a 44 cm Diameter Column, $U_g = 5.0$ cm/s

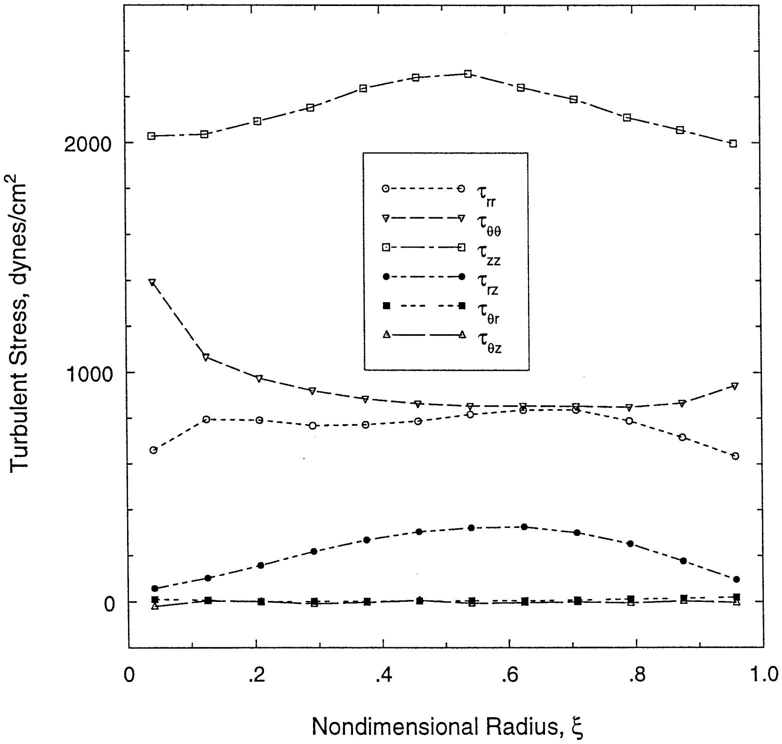

Figure 4.53: Components of the Turbulent Stress tensor, τ, in a 44 cm Diameter Column, $U_g = 10.0$ cm/s

The profile for $\overline{u_\theta'^2}$ also indicates high values closer to the wall, which can be reasoned as being caused by the spiraling movement of the eddies as they pass through the column.

On the other hand, the radial profiles for $\overline{u_r'^2}$ show just the opposite trends than $\overline{u_\theta'^2}$, especially at high gas velocities. Results indicate that there is always a dip in the $\overline{u_r'^2}$ profile at the center axis of the column. This dip may be an artifact of the cylindrical coordinates which are used in calculating the stresses. If the eddies had a tendency to cross over the axis, as mentioned before, then an equivalent displacement in the $x - y$ plane, would result in a lower Δr at the center, than away from the center. This explanation is in complete agreement with the reason for the peaks in $\overline{u_\theta'^2}$ at the center, and goes to substantiate the spiraling and vortical motion of the eddies crossing over the line of symmetry.

The profiles for the axial normal stress vary with gas velocity. At low gas velocities, these profiles tend to peak near the column wall. With further increase in gas velocity this peak seems to shift more towards the center of the column. In fact, a similar trend is also observed for the radial and angular normal stresses as a function of superficial gas velocity (shown for the 14 cm diameter column with distributor **6A**). At the low gas velocities considered the flow, according to Chen et al. (1994), is in the vortical spiral flow regime. They describe the instantaneous flow in this regime as having a central upward spiraling motion of the gas plume which rocks laterally back and forth. The downflowing liquid between the central bubble stream and the wall is also characterized by liquid vortices that contribute to the large fluctuations in the velocities, in all directions. With an increase in velocity, there is more intense coalescence of the bubbles with the formation of larger bubbles or gas 'pockets', that rise discretely up the column in spiraling paths that are constantly changing in diameter. Hence, while an increase in superficial gas velocity causes an increase in the overall magnitude of the velocity fluctuations, it also tends to spread the fluctuations over the column cross-section. As a result, the profiles for the axial normal stresses start to peak increasingly towards the middle annular region than at the wall of the column, which is closer to the time averaged position of flow inversion. When using the distributor **6B**, since the bubbles are larger, even at low gas velocities, there is more bubble-bubble interaction. Therefore, the peak near the wall of the normal stresses is not as pronounced as in the case of the distributor **6A**.

It is noted here that due to the finite size of the tracer particle used in the CARPT experiments, the maximum range of frequencies tracked by the particle are up to 30 Hz. Therefore the present measurements represent only the large scales of the turbulence structures. However, since the large scales contain the most energy, it is expected that what remains due to the smaller scales is not very significant in magnitude. Validation of CARPT measurements for the turbulence parameters is done by comparing CARPT results with independent experimental measurements (discussed in a later section in this Chapter).

The results presented for the turbulent stresses indicate that the shear stresses are much lower than the normal stresses (also reported by Devanathan 1991; Chen et al. 1994). This implies that the cross-correlation (shear stress) between the velocities are not as strongly correlated as the auto-correlation (normal stresses), which is normal. The non-zero, positive τ_{rz} term can be interpreted in two different ways. In terms of a correlation, this implies that for a positive perturbation in the axial direction, the system reacts by resulting in a positive displacement in the radial position. Physically this means that the vortices or eddies have a preference to a +z +r rotation. From a shear stress point of view the positive τ_{rz} means that a shear in the axial velocity causes an outward radial transport of momentum. On the other hand the cross-correlation between the fluctuating angular velocities with the radial and axial velocities is close to zero. This implies that the rotational movement of the spiraling vortex structures is uncorrelated from its axial and radial movement, and is in this sense totally random. This also means that there is no net transport of axial or radial momentum in the azimuthal direction.

The most common approach to modeling the correlations between the fluctuating velocities, $\overline{u_i' u_j'}$ (turbulent stresses) is by using Boussinesq's hypothesis and a gradient diffusion model, given in vector notation by

$$\overline{\vec{u}'\vec{u}'} = -\nu_t[\nabla\vec{u} + (\nabla\vec{u})^T] + \frac{2}{3}[\frac{1}{2}\mathrm{Tr}(\overline{\vec{u}'\vec{u}'})] + \frac{2}{3}\nu_t\nabla.\vec{u} \tag{4.7}$$

$$\frac{1}{2}\mathrm{Tr}(\overline{\vec{u}'\vec{u}'}) = k$$

where the turbulent kinetic energy k is solved using the $k-\epsilon$ model. It is often argued that the $k-\epsilon$ model is inappropriate for modeling turbulence in multiphase flows such as in bubble columns (Sokolichin and Eigenberger 1994), due to the highly non-isotropic behavior of the flow in these systems. However, for the lack of any suitable alternative, the $k-\epsilon$ model is still being predominantly used (Jakobsen 1993). Considering the experimental data from CARPT for the correlation of the various fluctuating velocity terms (in the long time averaged sense), and the gradients of the time averaged velocities, the only gradient that exists under fully developed flow conditions, in the middle section of the column, is $\frac{\partial u_z}{\partial r}$. This corresponds with the only non-zero cross-correlation term, τ_{rz}, which suggests that there may be some meaning to using the gradient diffusion approach. However, with regard to the diagonal terms that appear in the turbulent stress tensor, the axial normal stress is much larger (about two to three times) than the radial and angular normal stresses. Such a characteristic feature is commonly observed for most multiphase flows, such as gas-liquid (Franz et al 1984; Mudde et al 1997), gas - solid (Dasgupta et al. 1994) gas-liquid-solid (Sannaes 1997). Therefore, assuming the kinetic energy to be equally distributed between the three directions is not valid. To account for this an appropriate weighing factor can be given to the second term involving k in Equation 4.7, that represents the distribution of k along a given direction. Since this needs to be known *a priori*, the existing information from experimental data can be used to assign this factor. For the case of long time averaged measurements, results from CARPT show that in general, k is approximately distributed along the three directions in a cylindrical coordinate system as $\tau_{rr}:\tau_{\theta\theta}:\tau_{zz} = \overline{u_r'^2}:\overline{u_\theta'^2}:\ \overline{u_z'^2}=f_r:f_\theta:1$, where $f_r \sim f_\theta=0.3$ to 0.5. Such an approach, of appropriately weighing k in writing the balance equations along each direction, has been reported by Neti and Mohammed (1990) in their simulation of two phase flows in jets.

Along this argument, the eddy viscosity which usually is defined for bubble column flows as:

$$\nu_t = C_\mu \frac{k^2}{\epsilon} \tag{4.8}$$

can be modified as follows to account for the directional differences in the turbulent kinetic energy,

$$\nu_{t,i} = C_\mu f_i \frac{k^2}{\epsilon} \tag{4.9}$$

where f_i is the ratio factor for distribution of k along a given direction. The suffix i in $\nu_{t,i}$ represents the magnitude of ν_t in the i^{th} direction and should not be confused with a vector. The above method of introducing the factor f into Equation 4.7, in an attempt to handle the anisotropic nature of the flow, introduces a certain degree of empiricism in the model, since the values of f are obtained from experiment. Another possible way of addressing the issue of the non-isotropic nature of turbulence in bubble columns is to write a Reynolds stress model for closure of the turbulent Reynolds stresses. In this model separate transport equations are written for each component of the Reynolds stress tensor. Here the production, dissipation and convection of each component mainly corresponds to the flow characteristics along each direction. Therefore, the anisotropy in the flow can be automatically handled by this type of closure. The main difficulty is that for two phase flows, many interaction terms arise and should be properly modeled (Lahey 1990; He and Simonin 1994).

Based on experimental measurements of the velocity cross-correlations and the velocity gradients, the eddy viscosity is important only as far as τ_{rz} is concerned (in the long time averaged sense), since the shear stresses in the other two directions and related velocity gradients are zero, for bubble column flows. Hereafter Reynolds shear stress refers to τ_{rz}.

4.4.2 Effect of Gas Velocity and Column Diameter on the One Dimensional (Axially and Azimuthally Averaged) Time Averaged Axial Velocity Profile

Figure 4.54 shows the effect of superficial gas velocity on the time averaged one dimensional axial liquid velocities, as a function of column diameter, using perforated plate distributors **6A**,**8A** and **18A** for the 14 cm, 19 cm and 44 cm columns, respectively. The bars represent the deviation of the local data from the one dimensional values averaged over the middle section of the column. On the average this deviation is around 10 % of the centerline velocity. In all the column sizes there is an increase in liquid velocities with both gas velocity and column diameter, which is expected. The difference between the interstitial liquid velocities in the downflow region is lesser than that in the upflow region, for different gas velocities. This is due to the large area in the annular portion of the column and the higher liquid holdup in this region, which results in larger volumetric flow rate when compared to the upflow region.

In the 14 cm column, not much difference is observed between the liquid velocities at gas velocities of 9.6 and 12 cm/s. On the other hand for the same difference (2.4 cm/s) at lower gas velocities, i.e. comparing the cases of $U_g = 2.4$ cm/s and $U_g =$ 4.8 cm/s, there is a noticeably large difference between the liquid velocities for these two cases. The same trends are noted in the 14 cm column using distributor **6B** (not shown). This suggests that initially there is a large increase of liquid recirculation with gas velocity, which tends to flatten out with further increase in gas velocity, in the churn-turbulent flow regime. Such comparisons are not obvious for the other column sizes due to the limited number of experiments conducted. This aspect is discussed in greater detail in Chapter 5 (scale-up issues).

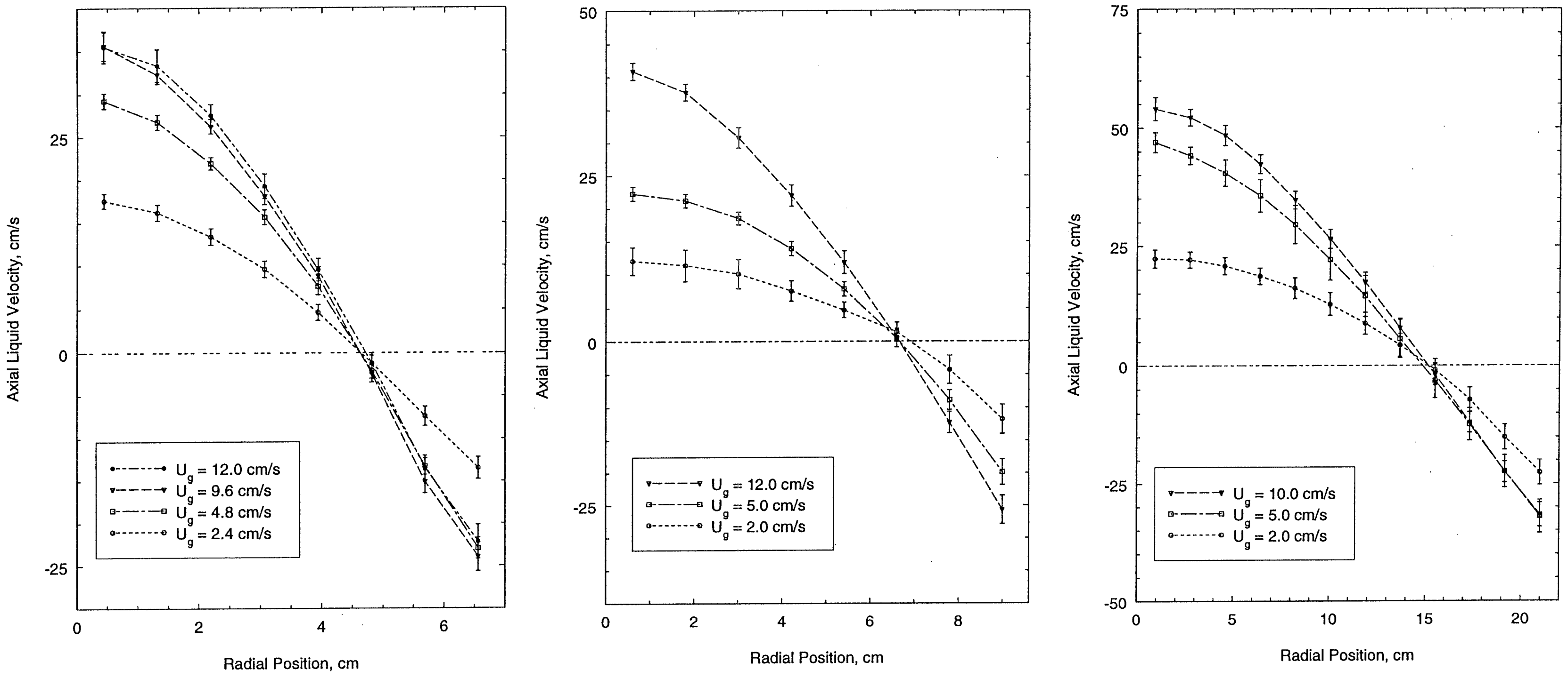

(a) (b) (c)

Figure 4.54: Effect of Superficial Gas Velocity on the Time Averaged One Dimensional Axial Liquid Velocity Profiles (a) Col. Dia. = 14 cm (**6A**) (b) Col. Dia. = 19 cm (**8A**) (c) Col. Dia. = 44 cm

For the 44 cm diameter column, a three dimensional analysis of the results in the earlier sections indicated existence of asymmetry in most part of the column, which was most pronounced at a gas velocity of 2 cm/s. Figures 4.55, 4.56 and 4.57 show the local, time averaged axial liquid velocities as a function of radial position, at selected axial and azimuthal positions in the 44 cm column, for the three gas velocities investigated. The asymmetry is most significant at $U_g = 2$ cm/s, and decreases with increase in gas velocity. For the condition of $U_g = 2$ cm/s, there is really no axial level where the flow can be deemed fully developed. However, for the sake of comparison and analysis averaging is done in the middle section of the column.

4.4.3 Effect of Gas Velocity and Column Diameter on the Axially and Azimuthally Averaged Turbulent Kinetic Energy

Figure 4.58 shows turbulent kinetic energy, averaged in the middle section of the column, as a function of superficial gas velocity for the three column sizes investigated. The results are shown for distributors **6A**, **8A** and **18A**. The bars, as in the previous case, represent the deviation of the local (r, θ, z) turbulent kinetic energy from the (θ-z) averaged values, which is about 10 %.

In general, the results have the same trends as for the axial liquid velocity, showing an increase with gas velocity and column diameter. The difference from the profiles for the axial liquid velocity is that at low gas velocities the increase of k with gas velocity is lower than when compared to the increase at higher gas velocities, in the churn-turbulent flow regime. Initially, in the bubbly flow regime the level of turbulence is low. It increases slightly in the transition regime and in the churn-turbulent flow, the increase is much larger. With further increase in gas velocity, well into the churn-turbulent flow regime, it is expected that the turbulent kinetic energy will level off, similar to the liquid recirculation velocities.

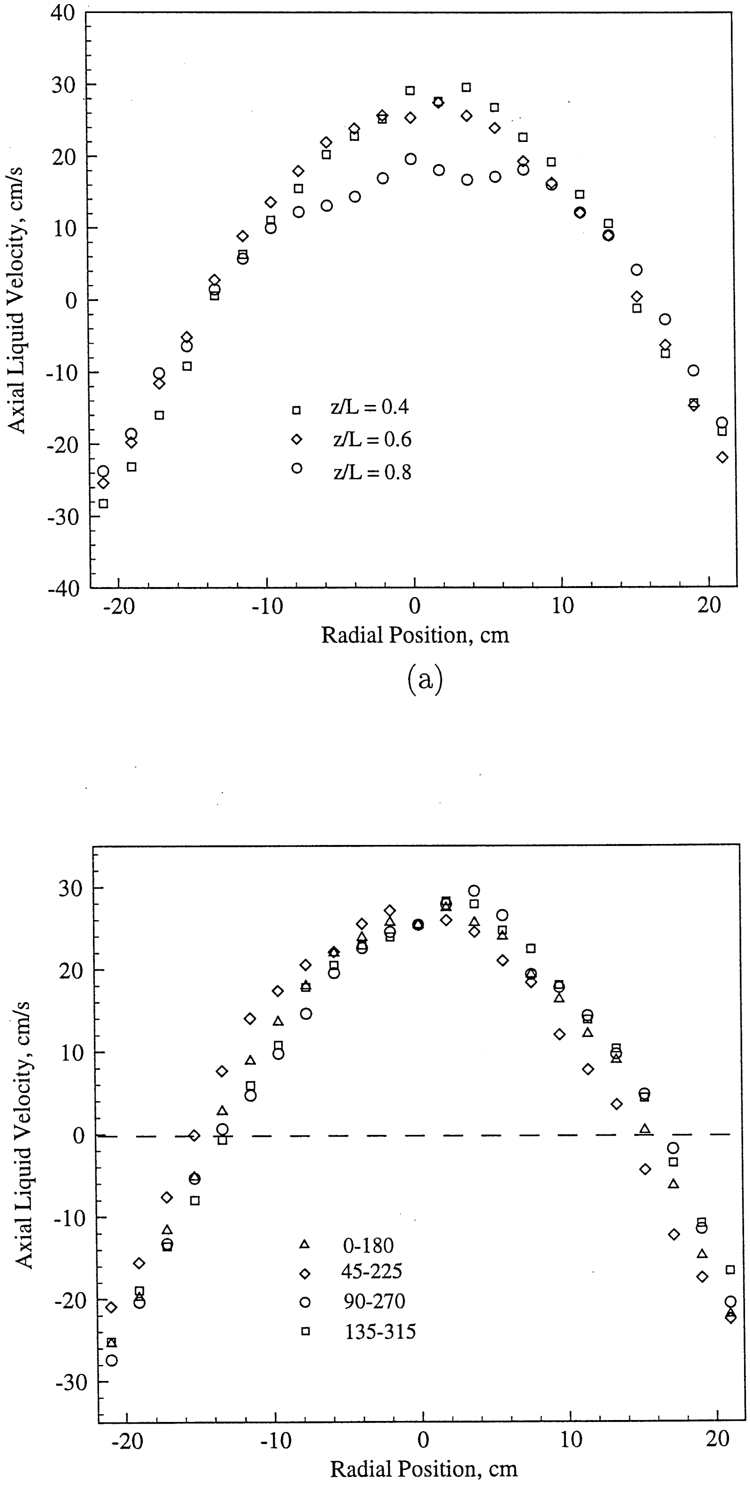

(a)

(b)

Figure 4.55: Time Averaged Axial Liquid Velocities in a 44 cm Column, U_g = 2.0 cm/s (a) Along Slice 0 - 180 (b) z/L = 0.6

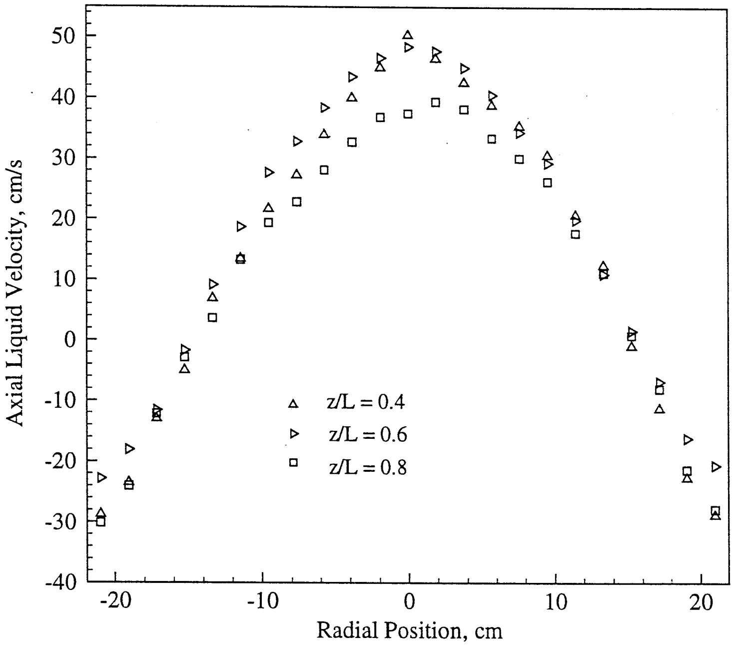

(a)

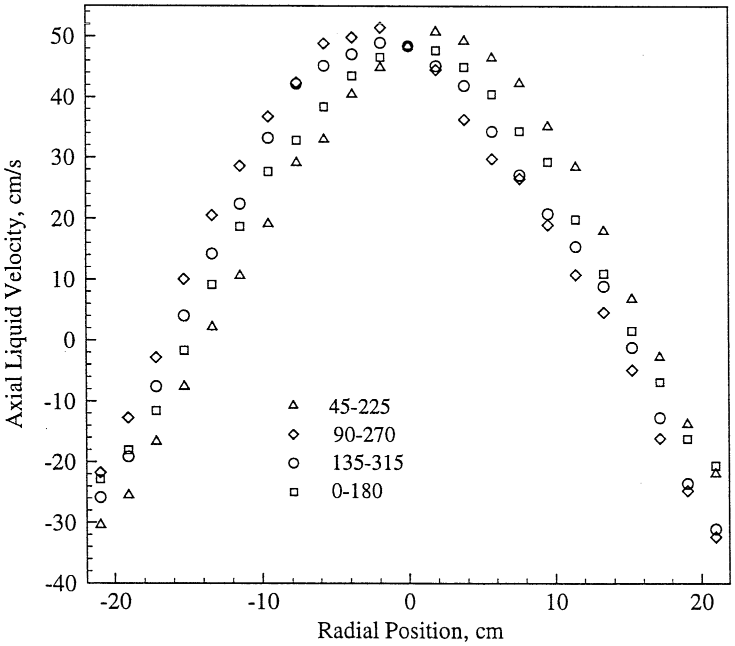

(b)

Figure 4.56: Time Averaged Axial Liquid Velocities in a 44 cm Column, U_g = 5.0 cm/s (a) Along Slice 0 - 180 (b) z/L = 0.6

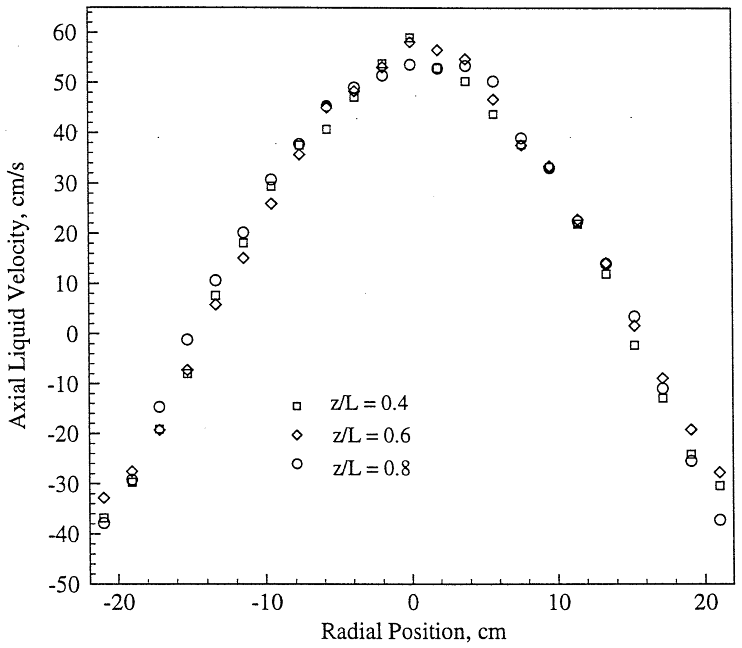

(a)

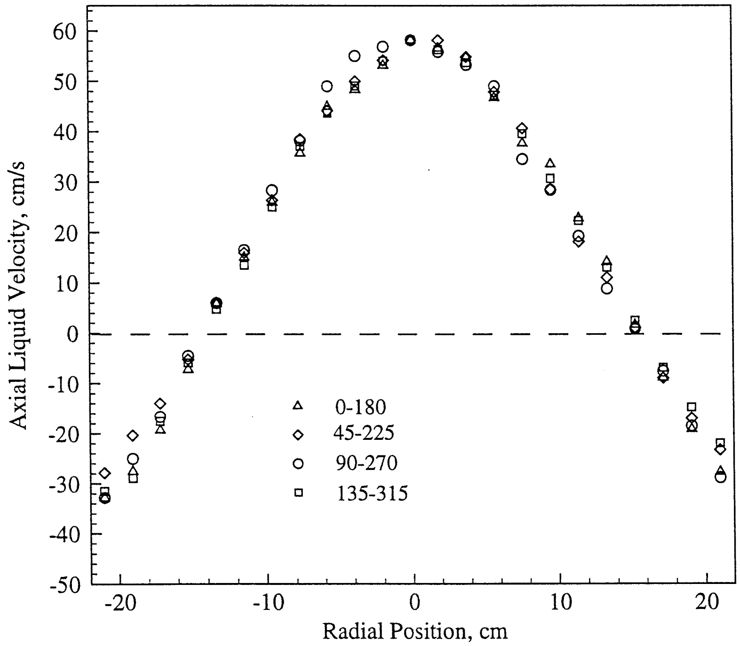

(b)

Figure 4.57: Time Averaged Axial Liquid Velocities in a 44 cm Column, U_g = 10.0 cm/s (a) Along Slice 0 - 180 (b) z/L = 0.6

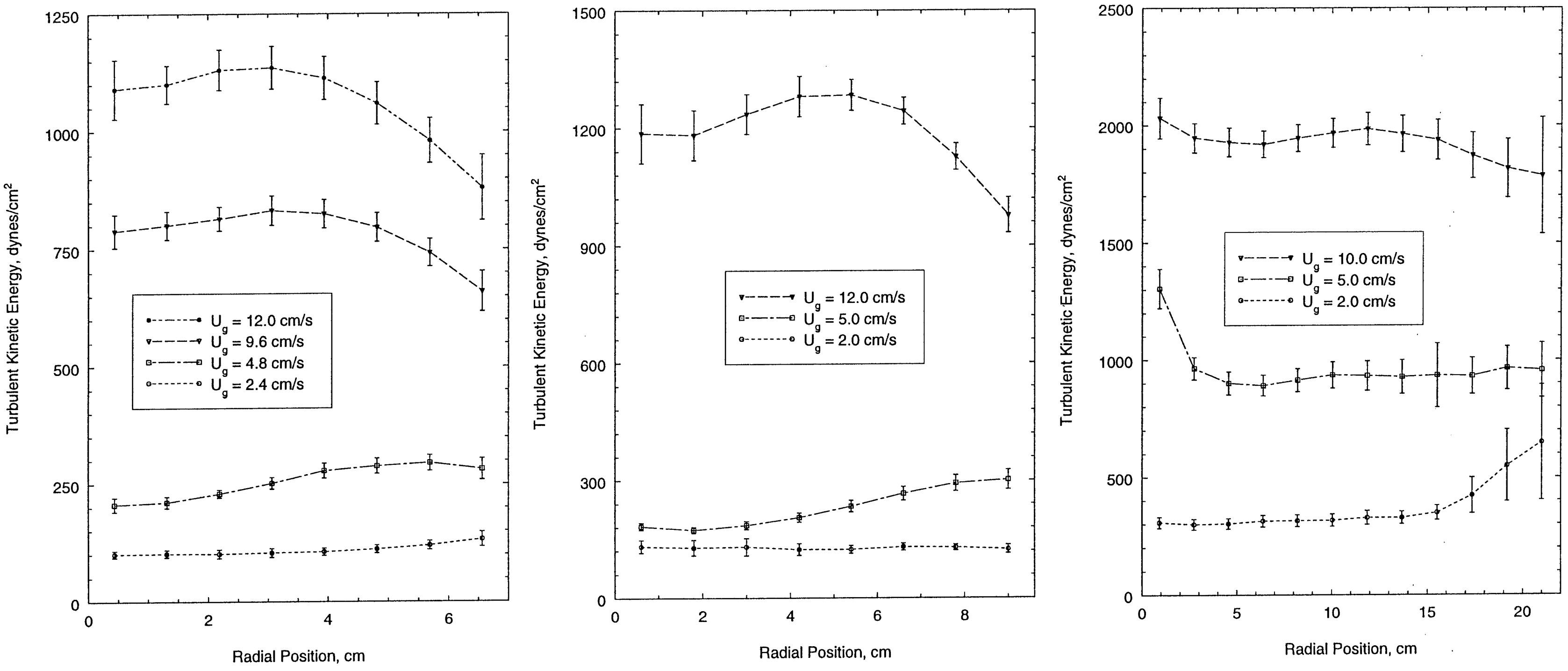

(a) (b) (c)

Figure 4.58: Effect of Superficial Gas Velocity on the One Dimensional Turbulent Kinetic Energy Profiles (a) Col. Dia. = 14 cm (**6A**) (b) Col. Dia. = 19 cm (**8A**) (c) Col. Dia. = 44 cm

An interesting feature is the change in the nature of the radial profiles of the turbulent kinetic energy with superficial gas velocity. For all column sizes investigated it is observed that at low gas velocities the turbulent kinetic energy peaks near the wall, while as the gas velocity increases the peak tends to shift towards the center of the column. This has been discussed earlier, in the section that discusses the turbulent stress measurements.

4.4.4 Effect of Gas Velocity and Column Diameter on the Axially and Azimuthally Averaged Turbulent Shear Stress

The Reynolds shear stresses are plotted as a function of superficial gas velocity for various column sizes in Figure 4.59. The spread of the data about the average profiles is higher for the shear stress than for the other turbulent quantities. This is not surprising, since the measurement of the shear stresses involves measuring the cross-correlation of the velocities, and is prone to more error.

The behavior of the shear stress is very similar to that of the turbulent kinetic energy. At low gas velocities, in the bubbly flow regime, the variation of the shear stress with gas velocity is low, as opposed to higher gas velocities, in the churn turbulent flow regime, where the variation is more pronounced. The radial variation of the shear stresses seems to be about the same for all the cases, showing a maximum close to the position of flow inversion.

4.4.5 Effect of Distributor Type on Fluid Dynamic Parameters

Experiments were performed as part of this work to investigate the effect of distributor on the fluid dynamics in the 14 cm and 19 cm diameter columns. For a given column and gas superficial velocity, a change in the distributor directly influences the bubble size and distribution in the system, which affects the fluid dynamics.

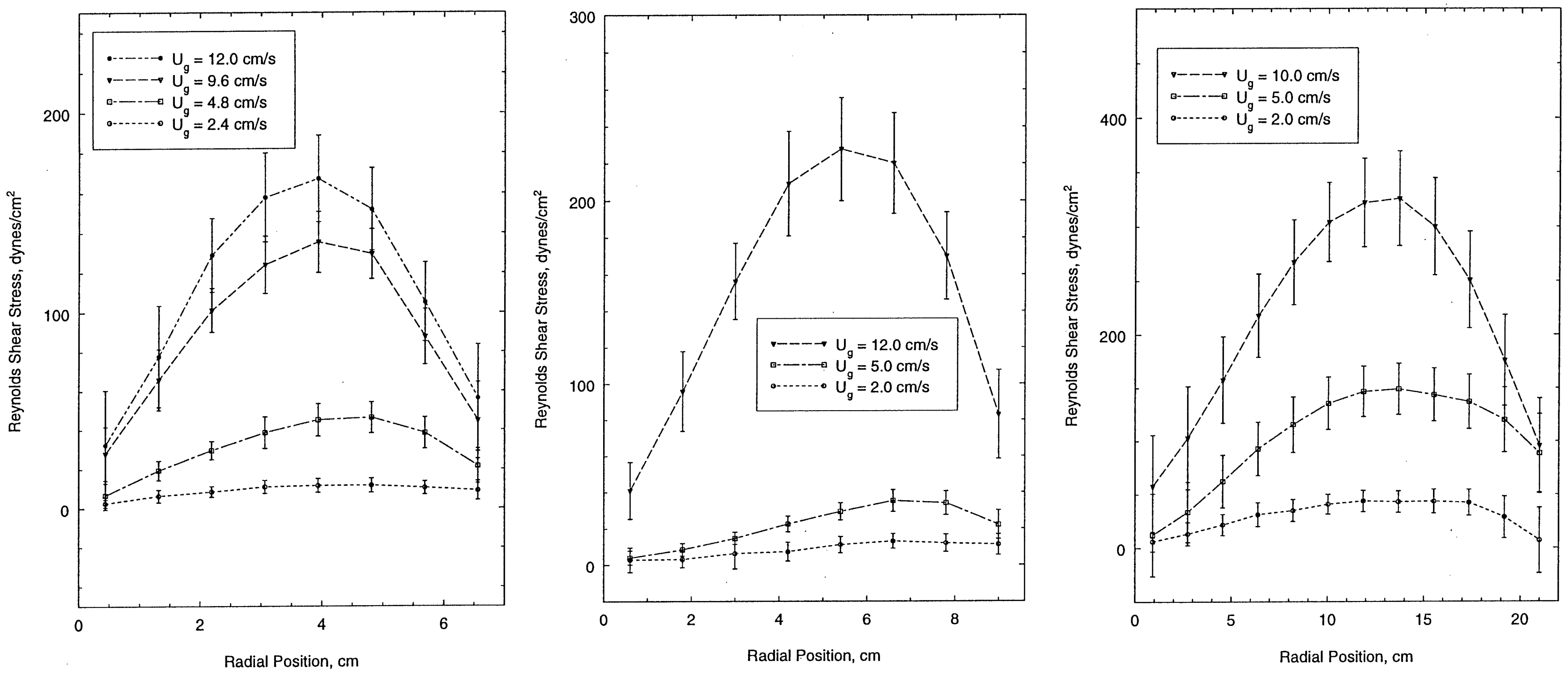

(a) (b) (c)

Figure 4.59: Effect of Superficial Gas Velocity on the One Dimensional Reynolds Shear Stress Profiles (a) Col. Dia. = 14 cm (**6A**) (b) Col. Dia. = 19 cm (**8A**) (c) Col. Dia. = 44 cm

In order to analyze the effects of distributor, and thereby bubble size, on the hydrodynamics of the system, three parameters that are representative of the fluid dynamics of the system are considered. These are the time average axial liquid velocity, the turbulent kinetic energy and Reynolds shear stress.

At the lowest gas velocity of 2.4 cm/s in the 14 cm column, the use of distributors **6A** and **6B** results in different values of the time averaged liquid velocity. Distributor **6A** results in smaller size gas bubbles close to the distributor. With regard to the time averaged flow pattern, there is the existence of an asymmetrical sheet like structure folding around the edge of the column (Figure 4.3). Distributor **6B**, with larger holes of 1 mm diameter, results in larger bubbles of about 6 mm at the distributor, which result in higher fluctuations at the inlet (higher turbulent kinetic energy). In this case the sheet like structure is not seen (Figure 4.11). Figures 4.60 and 4.61 show the axial profiles of the axial liquid velocities at various radial positions for the two cases. For distributor **6A** the axial liquid velocities are low at lower (axial) levels in the column. With further increase in axial position, they increase and finally level off near the top. On the other hand for **6B**, the velocities are axially more uniform, and are higher in magnitude than those for **6A**. This can be explained in terms of the flow phenomena that is observed in the systems for the two distributors. For distributor **6A**, the bubbles are initially small in size and therefore their rise velocity is relatively lower in the initial part of the column. At the lowest gas velocity of $U_g = 2.4$ cm/s, the level of turbulence in the column is low, and the rate at which the bubbles rise dictates the liquid velocities. As these originally small bubbles rise up the column they start to interact with other bubbles and coalesce to reach a stable bubble size (for the given operating conditions). This thereby increases the rise velocity of the bubbles, which in turn increases the axial liquid velocities higher up in the column. On the other hand, for distributor **6B**, the bubbles even as they are formed near the distributor are relatively larger (possibility of coalescence at the distributor, as described earlier), and are not very far from the stable bubble size for the given operating conditions and physical properties of the liquid. Therefore, the liquid velocities are in turn higher than that for **6A**, and are also axially more uniform. This is a mechanistic view of the dynamics of the system, based on visualization of the bubble column during the experiments. It

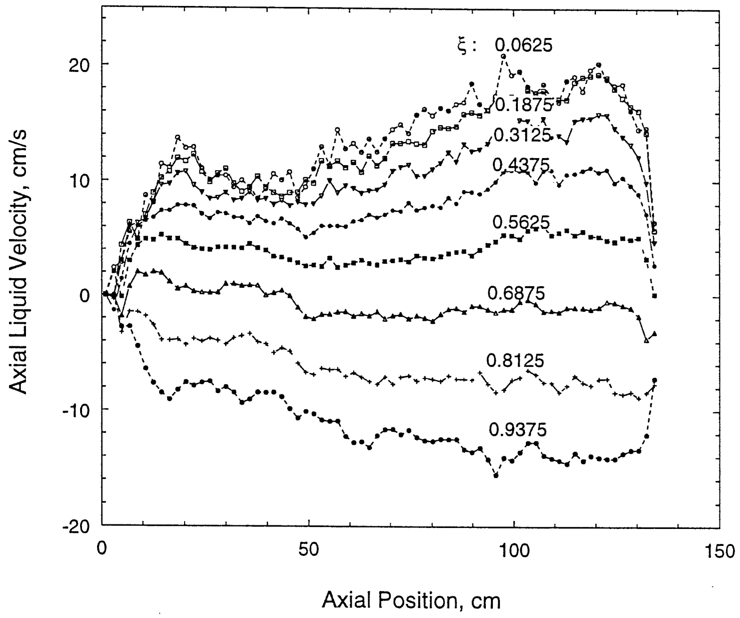

Figure 4.60: Time Averaged Liquid Velocity as a function of Axial Position in a Column of Diameter 14 cm, Distributor: **6A**, $U_g = 2.4$ cm/s

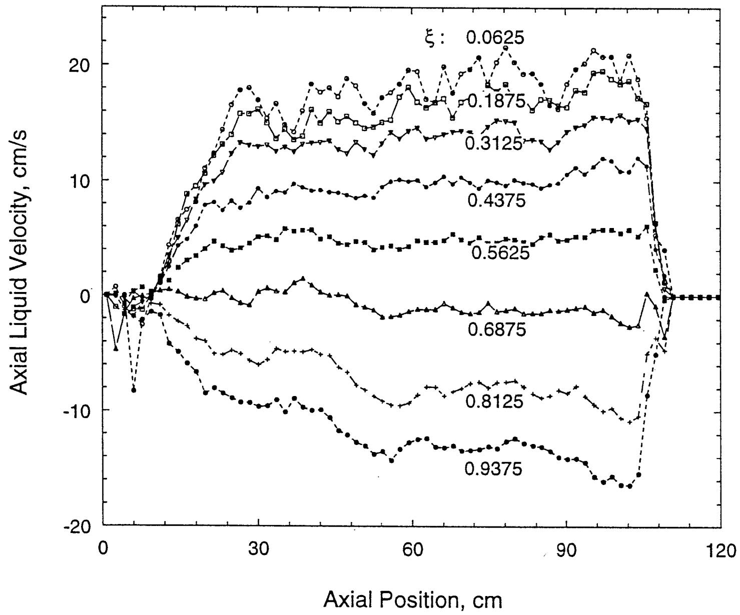

Figure 4.61: Time Averaged Liquid Velocity as a function of Axial Position in a Column of Diameter 14 cm, Distributor: **6B**, $U_g = 2.4$ cm/s

gives an essence of what dictates the liquid velocities along the height of the column in the bubbly flow regime, where the turbulence level is still relatively low and the bubble interaction (coalescence-breakup) is low compared to the churn-turbulent flow regime. In the bubbly flow regime, since the bubbles tend to rise in a rather rectilinear manner, a larger bubble size yields larger rise velocities and thereby higher liquid recirculation velocities. Similar interpretation is used by Krishna et al. (1994) based on the bubble growth model of Darton et al. (1977), to predict the gas holdup of the large columns in the churn–turbulent flow regime.

At higher gas velocities, in the churn-turbulent flow regime, there are still noticeable differences between the liquid velocities. However, the trends are opposite to those observed at low gas velocities. This is because for the higher gas velocities the size of the bubbles influences the fluid dynamics with a different mechanism. In the churn-turbulent flow regime, at high superficial gas velocities, a relative bubble size is judged based on comparison of the global gas holdups in the column, shown in Table 4.1. This suggests that in the 14 cm diameter column, the use of the distributor **6B** results in larger bubble sizes than that the use of distributor **6A**, since large bubble sizes result in lower gas holdups. However, since the calculated regimes of bubbling are different for the two distributors at high velocities, a direct comparison cannot be made.

For the 19 cm column, the column with the bubble cap distributor, **8B**, and cone distributor, **8C** result in larger bubble sizes than that for the perforated plate distributor **8A**. This is reasonable, since it implies that the distributor with larger open area results in larger bubble sizes, for the operating condition under consideration. In addition, the flow appeared more violent for the case of the cone and the bubble cap, with large structures frequently moving up the system in a spiraling motion. On the other hand with the perforated plate, the flow appeared less violent and the large structures were less distinct and less frequent. These observations conform with calculations of the orifice Reynolds number reported in Table 4.2, which show the highest orifice Reynolds number is for the cone, followed by the bubble cap and the perforated plate distributor. The Re_o for both the cone and the bubble cap distributors are much higher than that of the perforated plate. At a gas velocity of 12 cm/s, all the distributors are in the jetting regime. Hence, the higher Re_o implies a higher inlet kinetic energy and thereby results in increased turbulence.

Figure 4.62 shows a comparison of the axial liquid velocities measured in the 19 cm diameter column using different distributors, at a high superficial gas velocity of 12 cm/s. The trends imply that for larger bubble sizes the time averaged axial liquid velocity gets suppressed in comparison with that for the relatively smaller bubble sizes. The reason for this is explained below.

Figure 4.63 shows a comparison of the turbulent kinetic energy in the 19 cm column for the three distributors considered. The results for the bubble cap and the cone are much higher than that for the perforated plate distributor, which is in agreement with visual observations mentioned above. The larger bubbles that are formed in the presence of the cone and the bubble cap, tend to have high instantaneous velocities. However, due to their size they tend to have high instantaneous radial and angular velocities as well (Fan and Tsuchiya 1990). Due to their interaction with the liquid, the resulting eddies and vortex structures formed are dictated by the bubble movement and this results in large fluctuating velocities, in the azimuthal, radial and the axial direction. Therefore, although the magnitude of the resultant instantaneous liquid velocity, $\sqrt{u_r^2 + u_\theta^2 + u_z^2}$, and kinetic energy are higher, on time averaging these instantaneous velocities yield a lower value of the mean upward velocity but larger value of the fluctuating velocity terms (turbulent kinetic energy). As a result, for the perforated plate distributor the turbulent velocities are lower, but the net axial component of the time averaged velocity is higher. Hence, the analysis based on the bubble sizes in the column and experimental observations agree with the analysis based on the inlet kinetic energy as a function of the orifice Reynolds number in the jetting regime. Although there is a distinct difference in global gas holdups, it is noted that the difference is not significant.

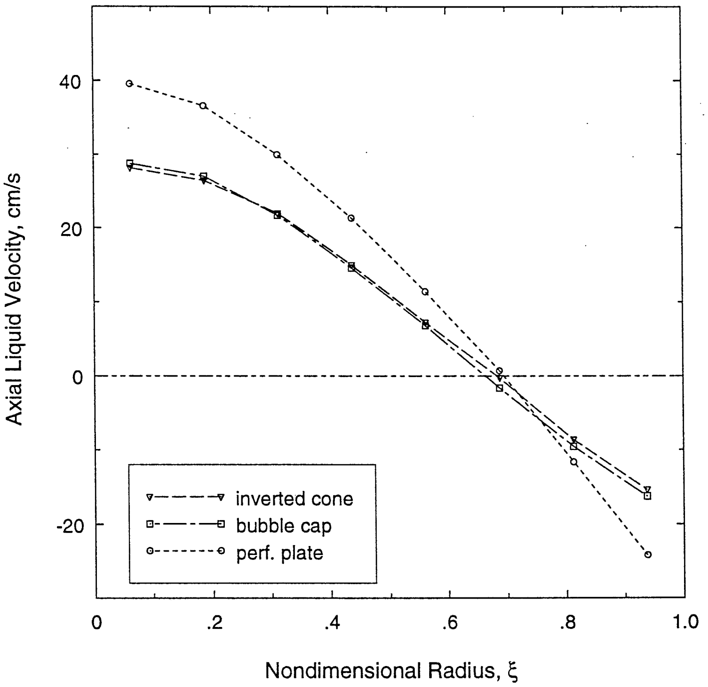

Figure 4.62: Effect of Distributor on the Time Averaged Liquid Velocity in a Column of Diameter 19 cm, U_g = 12.0 cm/s

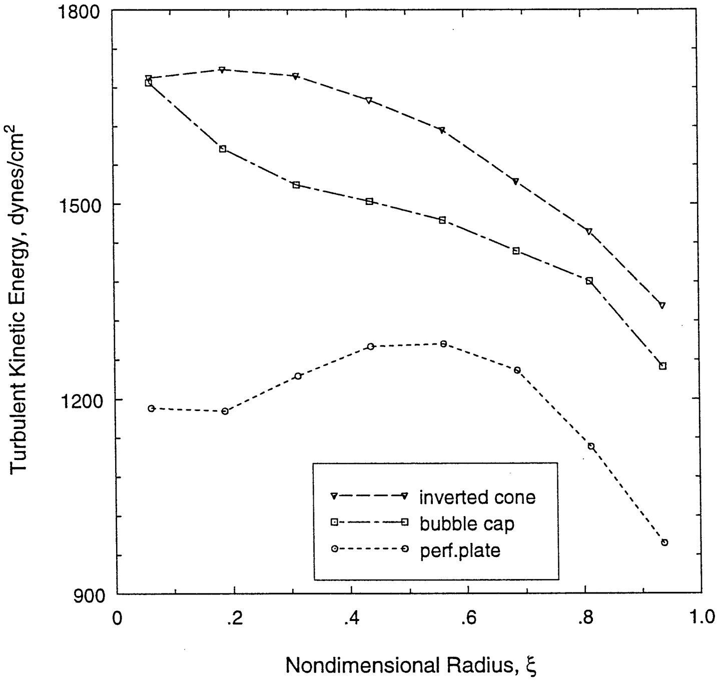

Figure 4.63: Effect of Distributor on the Turbulent Kinetic Energy in a Column of Diameter 19 cm, U_g = 12.0 cm/s

It is interesting, however, to note that there is no significant difference between the turbulent shear stresses for any of these cases (Figure 4.64). This implies that while the intensity of turbulence in the system changes from distributor to distributor for the given operating conditions, the correlation between the radial and axial instantaneous velocities is still roughly the same. In other words, a lower perturbation (or deviation) from the mean velocity in the axial direction results in a correspondingly lower deviation in the radial direction. Hence, the extent of cross-correlation is the same. For approximately the same Reynolds shear stress, a higher mixing length (or eddy viscosity) in the one dimensional model (Appendix A), would result in lower

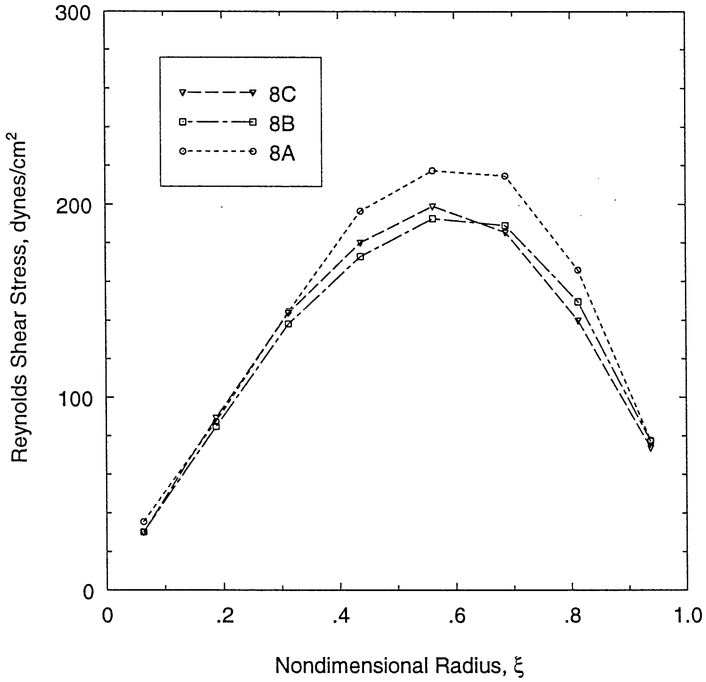

Figure 4.64: Effect of Distributor on the Reynolds Shear Stress in a Column of Diameter 19 cm, $U_g = 12.0$ cm/s

axial velocities and a lower mixing length would give higher liquid velocities. This can be understood by relating the bubble size to a mixing length. Large bubbles produce higher turbulent viscosity due to an increase in mixing length and a smaller velocity gradient (and lower velocities) because of their higher radial motion. A better (quantitative) understanding requires the simultaneous measurement of the bubble sizes along with the other fluid dynamic parameters, under various operating conditions.

4.5 Reproducibility of CARPT Experiments

In order to check for reproducibility, CARPT experiments in the 14 cm diameter column, using distributor **6A**, were conducted twice at a superficial gas velocity of U_g = 12.0 cm/s. This is shown in Table 4.1, in which the global gas holdups are reported to be almost the same for the two runs. The CARPT results for the above two runs (same operating conditions) are compared for the one dimensional time averaged velocity profile, the turbulent Reynold shear stress and the turbulent kinetic energy. The comparison is shown in Figure 4.65 for the operating conditions specified above. The results for the fluid dynamic parameters are clearly very close to each other, well within experimental variation. Therefore under a given operating condition, for the same characteristics in the flow, e.g., the overall gas holdup which is dictated by the bubble size distribution, measurements from CARPT are reproducible.

4.6 Comparison of CARPT Results with Independent Experimental Measurements

The objective of this section is to compare the results from CARPT measurements with independent experimental data, and thereby provide a validation for the CARPT technique. In order to validate the CARPT results, the data for the time averaged liquid velocities and the turbulent (shear and normal) stresses have been compared against other measurements. For the mean velocities, Heat Pulse Anemometry (HPA) experiments were conducted as part of this work to measure the time averaged liquid velocities in a 19 cm diameter column under operating conditions similar to that used for CARPT experiments.

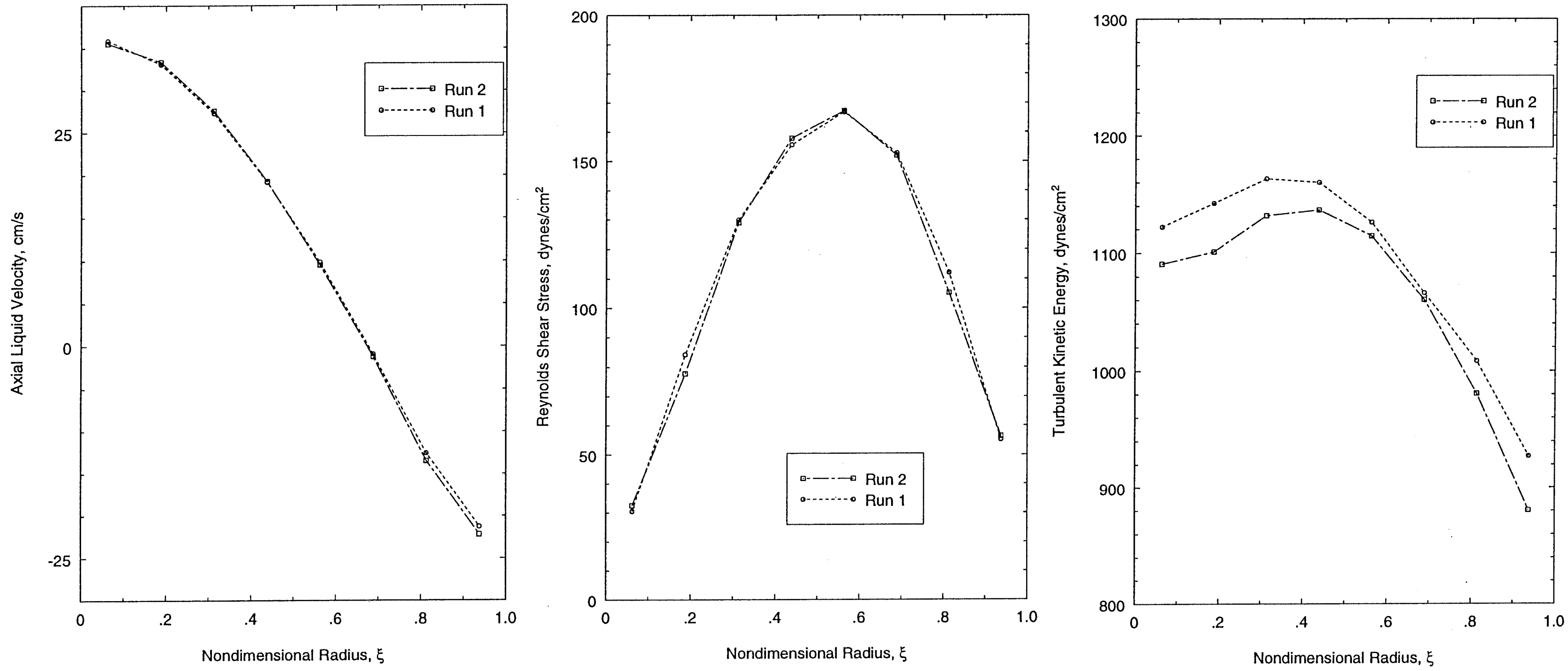

(a) (b) (c)

Figure 4.65: Repeatability of CARPT Experiments, D_c 14 cm, $U_g = 12.0$ cm/s, **6A** (a) Axial Liquid Velocity (b) Turbulent Shear Stress (c) turbulent Kinetic Energy

Measurement of the turbulence parameters, such as the Reynolds stresses requires instantaneous measurements of the liquid velocity. In two phase flows such as in bubble columns techniques traditionally used in single phase flow have to be suitably modified to accommodate the existence of the gas or bubble phase, which is both cumbersome and expensive. Therefore, for the purpose of validation of the turbulence parameters, CARPT results have been compared with experimental measurements in the literature.

4.6.1 CARPT versus HPA Data for the Time Averaged Liquid Velocity

The Heat Pulse Anemometer (HPA) is a time-of-flow measurement technique used to measure the mean liquid velocity between two points in the flow field. It essentially measures the distribution of the passage time of fluid elements that start at one point in the flow and happen to meet at another point downstream. Heat is used as a tracer to tag the fluid elements or particles. This technique, in a sense, measures the residence time distribution of fluid elements between the emitter and sensor. By fitting the response measured by the sensor using a suitable model, the mean time of passage (or mean residence time) of the fluid elements can be deduced, from which the average velocity of the fluid between the sensor and emitter is calculated. This technique, therefore, only provides an indirect measurement of the time averaged liquid velocity between two points, and is based on the assumption that in a time averaged sense, the emitter and sensor probes are positioned along the streamline of liquid motion. The software, hardware and probes have been developed and built by Prof. Lubbert's group (Lubbert and Larson 1990), who originally used HPA to measure liquid velocities in fermenters. Details of the HPA technique along with the variables of measurements, model for data interpretation and analysis of the results are presented in Appendix C.

The HPA experiments were conducted in the 19 cm diameter column using distributor **8A**, for three gas velocities, 2 cm/s, 5 cm/s and 12 cm/s, and static heights corresponding to those for the CARPT experiments given in Table 4.1. For a given radial position, the probes were placed at different axial distances by fixing the position of the emitter and varying the position of the sensor downstream. The minimum distance between the emitter and sensor of 3.0 cm and a maximum of 19.0 cm were used. Care was taken to position the probes in the middle section of the column, where the flow is well developed. Several experiments were conducted for a given set of positions of the emitter and sensor probe. However, due to the sensitivity of the equipment to external disturbances (noise), a significant portion of the experiments had to be rejected, based on the nature of the measured detector response. For a given radial location, the resulting mean residence times were used to calculate the mean velocity of the liquid between the emitter and sensor, the average of which has been considered for comparison with CARPT data. The experiments were conducted for four such radial locations of the probes for a given gas velocity.

A comparison of the one dimensional axial liquid velocities from CARPT with those obtained from the HPA time-of-flow measurements is shown in Figure 4.66. The trends for the time average axial liquid velocity are the same for all the gas velocities considered. Velocities from HPA are consistently lower than those measured by CARPT towards the center of the column, i.e., $r \leq 4$ cm. In the outer annular region of the column, $r \geq 4$ cm, the comparison between the two techniques is better, with slightly higher magnitudes of the liquid velocity shown by the HPA measurements, especially at the highest gas velocity. In general, it seems that results from HPA show flatter profiles for the axial liquid velocity than that of CARPT. Considering the nature of the HPA measurements, in terms of deducing the velocity from the time-of-flow data, rather than obtaining direct velocity measurements, the present agreement between the two techniques is considered satisfactory.

Using the HPA technique, in principle, it is also possible to obtain some information about the local mixing of the liquid. The experimental results for this, however, are counter-intuitive, and do not agree with general observations. More details regarding this aspect are discussed in Appendix C.

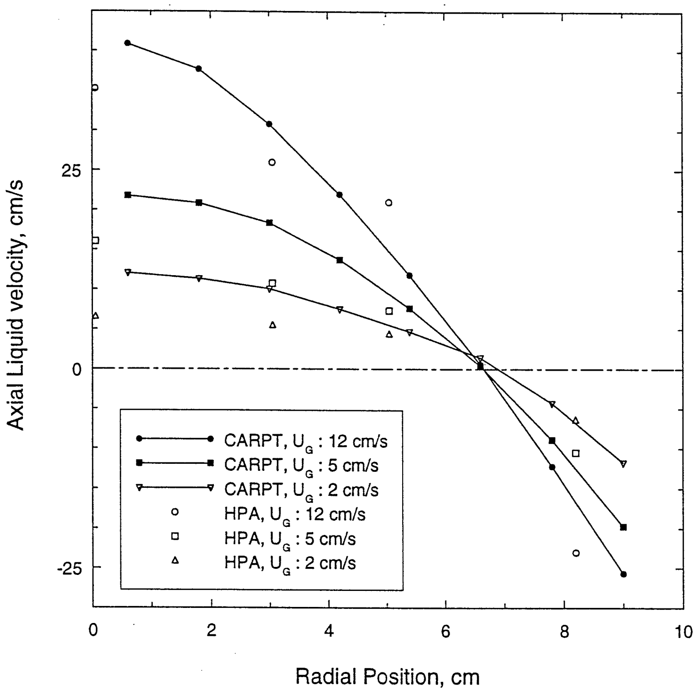

Figure 4.66: Comparison of CARPT and HPA results for the Time Averaged Axial Liquid Velocity, Col. Dia. : 19 cm, Distributor: **8A**

4.6.2 Reynolds Stress Measurements

Reynolds stress measurements from CARPT have been compared with experimental data of Menzel et al (1990) and Mudde et al. (1997).

Comparison of Reynolds Shear Stresses

Menzel et al. (1990) were among the first to successfully measure the Reynolds shear stress, τ_{rz}, in bubble columns. Their experiments were conducted in two column sizes, 15 cm and 60 cm, using two systems: air-water and air-alcohol/water. They used a Hot Film Anemometer (HFA) with triple split probes, in order to determine the sign of the two components (r, z) of the instantaneous velocity simultaneously. In order to compare the present CARPT data with the results of Menzel, the 14 cm diameter column was chosen with distributor **6B**, which is similar to that used by Menzel's group. The superficial gas velocities were also chosen to match that of Menzel et al. (1990).

A comparison of the shear stress measurements from CARPT with data of Menzel et al. (1990) is shown in Figure 4.67. As reported by Menzel, the definition of the shear stress is

$$\tau_{rz}^{Menzel} = (1 - \epsilon_g(r))\rho_l \overline{u_r' u_z'} \tag{4.10}$$

The above definition of the Reynolds stress was chosen by them for convenience, for one dimensional modeling purposes. For comparison with CARPT data, the results of Menzel for the turbulent shear stress profiles have been divided by their measured liquid holdup profile, to yield the shear stress, as defined in the present work.

Comparison of τ_{rz} shown in Figure 4.67 is encouraging. For two measurement techniques that are based on different principles of operation, the magnitudes of the correlation between the fluctuating velocities are rather close to each other. This provides a valuable substantiation of the CARPT technique for measurement of turbulence parameters. The largest discrepancy between the two sets of data is observed close to the wall of the column, where results from HFA are higher than those from CARPT. A possible reason for this difference could be due to the fact that closer to the wall the CARPT particle tracer is not able to capture the higher frequencies of the liquid movement, which may dominate the flow in this region. On the other hand, it is also known that intrusive probes such as the HFA result in higher measurement error close to the wall due to wall effects that interfere with the signal. Therefore, the larger discrepancy near the wall could be due to errors in both CARPT measurements as well as HFA. The overall results suggest a modest to good comparison between the two techniques and hence provide a validation of CARPT in measurement of the turbulent shear stresses.

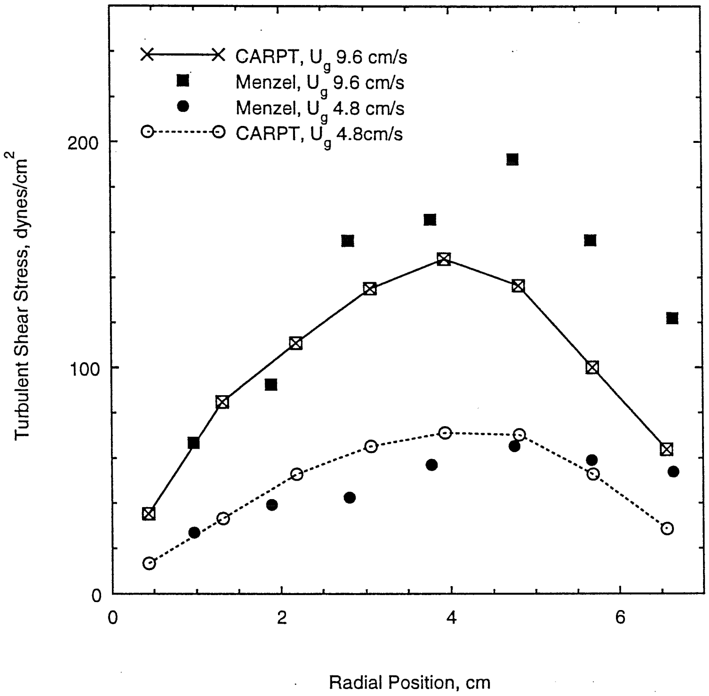

Figure 4.67: Comparison of the Turbulent Reynolds Shear Stress between CARPT and HFA Data of Menzel et al. (1990).

Comparison of CARPT with LDA Measurements

Groen et al. (1996) have developed and conducted Laser Doppler Anemometry (LDA) experiments in bubble columns to measure the axial and tangential components of the liquid velocities (Groen et al. 1996; Mudde et al. 1997). Comparison of CARPT results for some of the turbulent stresses can be made with their data in a 15 cm diameter column, although the superficial gas velocities are not exactly the same and the distributors (sintered plate, 40 μm pore size) used for the two cases are different. The objective here is to look for a qualitative comparison between the data from the two techniques.

Comparisons of the turbulent stresses (axial normal, azimuthal normal and axial-azimuthal shear) for two sets of operating conditions are shown in Figures 4.68 and 4.69. The results show that there is good order of magnitude comparison between

CARPT and LDA. However, the profiles from the two techniques are quite different. This has been noted by Mudde et al. (1997), from which the LDA data for the comparison has been obtained. They suppose that since the LDA can measure very high frequencies up to about 1000 Hz, with the LDA they are able to pick up all the high frequency fluctuations as well, which is not possible with CARPT. This may result in the types of profiles that they observe with LDA, which have not been reported so far in the literature, for measurements in bubble columns.

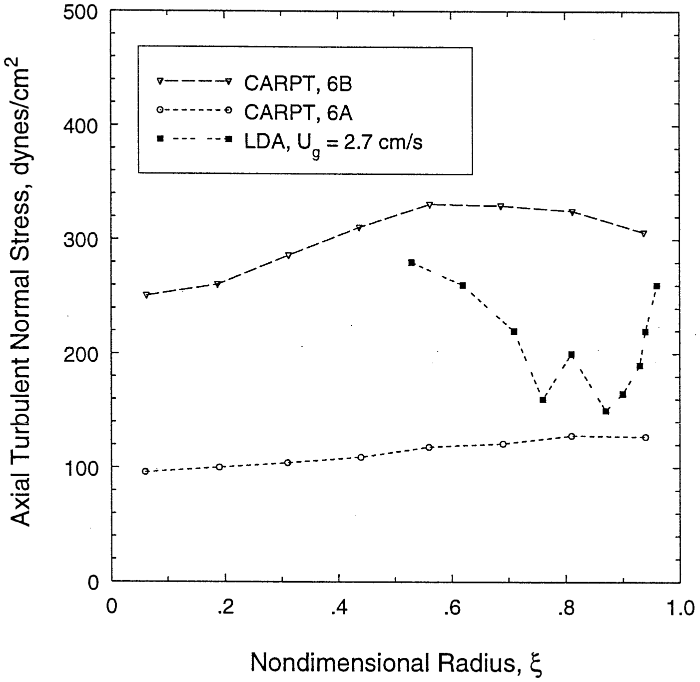

Figure 4.68: Comparison of CARPT (D_c: 14 cm; U_g: 2.4 cm/s) and LDA (D_c: 15 cm; U_g: 2.7 cm/s) Data for the Turbulent Axial Normal Stress

The order of magnitude comparison between the results for CARPT and LDA is rather good, especially for the shear stress, $\tau_{\theta z}$ and the azimuthal normal stress. As is obvious from the figures, the effect of the distributor on the data resulting from CARPT measurements is quite significant.

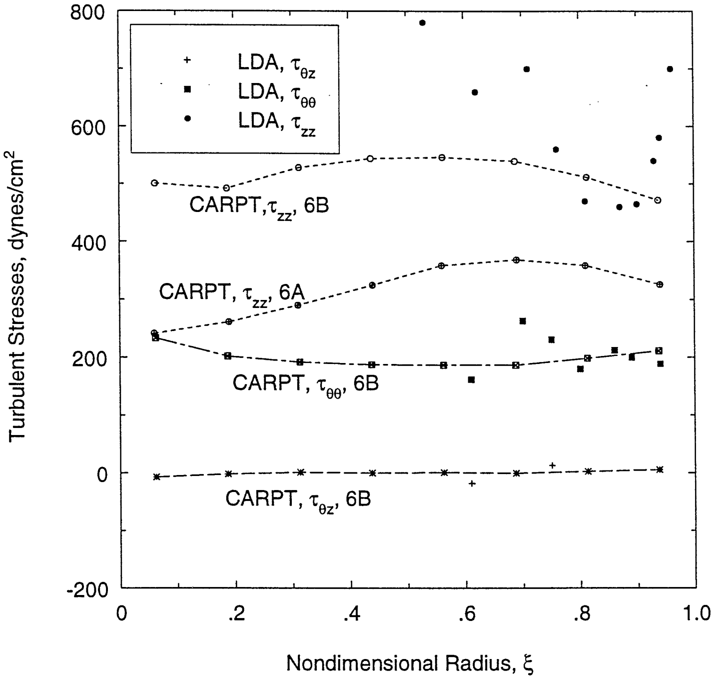

Figure 4.69: Comparison of CARPT (D_c: 14 cm; U_g: 4.8 cm/s) and LDA (D_c: 15 cm; U_g: 4.5 cm/s) Data for the Turbulent Stresses

4.6.3 Summary

Experimental data from CARPT has been successfully verified against independent experimental measurements. Heat Pulse Anemometer (HPA) experiments were conducted as part of this investigation to measure the time averaged liquid velocities in a 19 cm diameter column, with a perforated plate distributor, **8A**. Results from HPA measurements for the liquid velocities show reasonable agreement with CARPT results in the same column under identical conditions. CARPT data for the turbulent stresses have been verified against experimental data in the literature. The experiments in the 14 cm diameter column (distributor **6B**) were specifically designed to match, as close as possible, the experimental conditions of Menzel et al. (1990), in order to compare CARPT measured Reynolds shear stress profiles with Hot Film Anemometry (HFA) results of Menzel. Reasonable comparisons are noted for both the magnitude and radial profiles for the turbulent shear stress, τ_{rz}. CARPT results for the axial and azimuthal normal stresses, and $\tau_{\theta z}$ shear stress were compared with

LDA measurements of Mudde et al. (1997) in a 15 cm column. Results show good order of magnitude comparison between the data, although the profiles are different.

CARPT measurements for both the time averaged velocities and turbulent stresses have therefore been successfully verified against independent experimental data for the mean liquid velocities and Reynolds stresses. This serves in the validation of the CARPT technique.

4.7 Turbulent Eddy Diffusivities

The key property of turbulent motion is its ability to transport or mix momentum, energy, scalar quantities, etc. The rates of transfer and mixing in the presence of turbulence are orders of magnitude larger than the rates due to molecular transport. The most common method of dealing with equations governing turbulent flow is by treating the diffusive nature of turbulence via the introduction of a turbulent diffusivity or viscosity for a given quantity (momentum, heat, mass, etc.). This is done using the popular gradient model (following Boussinesq's hypothesis) for the correlations between fluctuating quantities, (e.g., Equation 4.7 for the velocity correlations appearing in the averaged momentum balance equation) with a suitable eddy viscosity or diffusivity. However, the eddy viscosity or diffusivity that appears in the resulting equations is itself unknown and is usually arbitrarily assigned or further modeled.

In the present section, the turbulent eddy diffusivities are defined as measured in a Lagrangian framework. Measurements of this type reported in the literature, usually pertain to studying the behavior of particulate suspensions in ideal homogeneous, isotropic turbulent flows. For example, Snyder and Lumley (1971) measured the Lagrangian statistical properties of different particles in a turbulent flow using a flow visualization technique. They showed that the Lagrangian velocity correlations have a similar shape to the Eulerian space correlations in homogeneous isotropic turbulent fields. Meek (1972) performed experimental and modeling studies for the statistical characterization of particulate suspensions in turbulence fields, in order to study the effect of particle size and density on the dispersion of particles. Considerable work has also been done in modeling the motion of particles in a turbulent flow field, following the work of Tchen (1947) (Hjelmfelt and Mockros 1966; Maxey and Riley 1983; Pismen and Nir 1978; Mei et al. 1991). Most of the studies in the literature, however, have been focussed on the dispersion of small heavy particles, as applied to aerosol particles and particulate dispersion in the atmosphere. In atmospheric dispersion studies the characterization of dispersion predominantly relies on measuring and modeling the rate of spread of particles (for example, pollutants in the atmosphere) by studying the probability density function of the particle locations at various times (Richardson 1926; Tennekes and Lumley 1972; Seinfeld 1986; Monin and Yaglom 1971).

In the modeling of turbulent flows such as gas-liquid flows in bubble columns, in an Eulerian framework using the Navier-Stokes equations, a gradient diffusion model is traditionally used to close the velocity-velocity, velocity-concentration and velocity-holdup (in the case of multiphase flows based on volume averaging) correlations. This results in eddy viscosity or eddy diffusivity terms in the final equations, as mentioned before. However, there has been no generally established relationship that relates the eddy diffusivities and viscosities, arising from the gradient approximation, with the turbulent eddy diffusivities defined in the Lagrangian framework. In isotropic and homogeneous turbulence it has been shown, by using scale arguments and by comparing the pdf for the spread of particles with the solution of the turbulent convective diffusion equation, that the diffusivity appearing in the convection-diffusion equation can be approximated by the Lagrangian based turbulent eddy diffusivities (Tennekes and Lumley 1971; Seinfeld 1986). Recently Lapin and Lubbert (1994) used a Lagrange-Euler model to simulate gas-liquid flows in bubble columns, in the bubbly flow regime. The dispersion coefficient for the gas bubbles in the simulation was arbitrarily assigned.

The objective of the present work is to measure the Lagrangian eddy diffusivities in bubble columns using CARPT, and use the measured eddy diffusivities for modeling liquid mixing in bubble columns. In Chapter 6 a two dimensional convection-diffusion model is developed and solved, assuming that the eddy diffusivities arising from the gradient approximation of the $\overline{u'C'}$ terms are equivalent to the CARPT measured Lagrangian turbulent diffusivities. The validity of this assumption is verified by comparing model predictions with experimental data.

4.7.1 Isotropic and Homogeneous Turbulence

Attempts at predicting the dispersion in a homogeneous, isotropic turbulent flow field began with the pioneering work of Taylor (1921). By using the method of 'continuous movements' he was able to relate the 'diffusing power' of turbulence to its statistical property, the Lagrangian auto-correlation coefficient. Thus, for a one dimensional situation, he obtained a relationship between turbulent dispersion and the auto-correlation of a fluid particle in the turbulent field as

$$\overline{y^2}(t) = 2\overline{v'^2} \int_0^t \int_0^t R'_L(\tau) d\tau dt \tag{4.11}$$

In the above expression , R'_L is the Lagrangian auto-correlation coefficient, $\overline{y^2}(t)$ is the mean square displacement of the fluid particle due to the Lagrangian turbulent fluctuating velocity and $\overline{v'^2}$ is the mean square fluctuating velocity. The Lagrangian auto-correlation coefficient is defined by

$$R'_L(\vec{X}, t) = \frac{\overline{v'(t)v'(t+t')}}{\overline{v'(t)^2}} \tag{4.12}$$

Under these conditions an expression for eddy diffusivity can be obtained by considering turbulent diffusion to be analogous to molecular diffusion. The Fickian diffusion equation is satisfied and the concentration has a Gaussian distribution of variance $2Dt$ (Hida 1980). The eddy diffusivity is then given by

$$D(t) = \frac{\overline{y^2}(t)}{2t} \tag{4.13}$$

Substituting for $\overline{y^2}(t)$ and simplifying, we have for long diffusion times:

$$D = \overline{v'^2}\tau_L \tag{4.14}$$

where τ_L is the Lagrangian integral time scale, the average time over which the flow is correlated with itself.

$$\tau_L = \int_0^\infty R'_L(\tau)d\tau \tag{4.15}$$

For a general case, turbulent diffusion and the eddy dispersion coefficient are second order tensors. The turbulent eddy dispersion coefficient or eddy diffusivity **D** is defined in terms of its $(i,j)^{th}$ element as (Hinze 1975)

$$D_{ij}(t) = \frac{1}{2}\frac{d}{dt}\overline{y_i y_j} = \frac{1}{2}(\overline{v'_i y_j} + \overline{y_i v'_j}) \qquad i = 1-3, j = 1-3 \tag{4.16}$$

The above equation indicates that the eddy diffusivity is a function of time. Consider the possible simplifications of the above relation. The simplest form is isotropic turbulence, in which the statistical features show no directional preference. In other words they are independent of rotation, and exhibit spherical symmetry. Hence the properties in all directions are identical.

$$D_{ii} = D_{jj}; \quad D_{ij} = 0, \quad i \neq j \tag{4.17}$$

When the turbulence has quantitatively the same structure through out the field it is said to be homogeneous. This implies that the statistical properties are invariant to translation. In this case the Lagrangian characteristics are independent of initial position of measurement.

4.7.2 Turbulent Flow in Bubble Columns

In bubble columns, the turbulent field is anisotropic with radial non-homogeneity. The statistical properties vary radially, as is observed from the computed auto-correlation coefficients. The cross-correlation, R_{rz}, is non zero indicating anisotropy, and in addition, there is considerable difference in magnitudes of the auto-correlation coefficients along each direction. Therefore the simplified expression of Equation 4.14 does not hold, and it becomes necessary to account for the existing non-idealities.

Corrsin (1953) explored the effect of a constant gradient in the mean velocity on turbulent diffusion in single phase pipe flow, by considering a hypothetical field of infinite extent with a uniform velocity gradient but with the cross-correlation (Lagrangian velocity correlation) term being zero. This implies that the field is isotropic. Lee and Dukler (1976) subsequently modified Corrsin's work to account for the cross-correlation terms.

The following equations are developed, based on the studies of Corrsin (1953) and Lee (1976). The radial non homogeneity is considered by accounting for the effects of the velocity gradient in the radial direction, which is coupled with the cross-correlation term, R_{rz}. While the gradient itself is non-linear, for the sake of computation it is assumed that in each column compartment the gradient is constant and only differs from compartment to compartment. In addition, based on the experimental evidence from the previous sections, it is assumed that only the radial variation of the axial velocity exists in the middle section of the column, and that the other velocity derivatives are zero. In other words, $\frac{\partial u_z}{\partial r} \neq 0$, $\frac{\partial u_z}{\partial \theta} = \frac{\partial u_r}{\partial z} = \frac{\partial u_r}{\partial \theta} = \frac{\partial u_\theta}{\partial r} = \frac{\partial u_\theta}{\partial z} = 0$. In the end zones, although the velocity derivatives exist, the cross-correlation terms are zero. Therefore the only major change is in the axial displacement, y_z, due to the presence of the radial gradient. The following analysis results in a new set of equations for the eddy diffusivity.

4.7.3 Equations for Turbulent Diffusivities

Basically, since with the CARPT technique it is possible to measure all the three components of the particle velocity, it is possible to calculate all the six components of the turbulent eddy diffusivity tensor.

The displacements y_r and y_θ due to the corresponding fluctuating components of the velocities are given by

$$y_r(t) = \int_0^t v_r'(t')dt' \tag{4.18}$$

$$y_\theta(t) = \int_0^t v_\theta'(t')dt' \tag{4.19}$$

Due to the presence of the velocity gradient, (Figure 4.70), the displacement in the z direction is

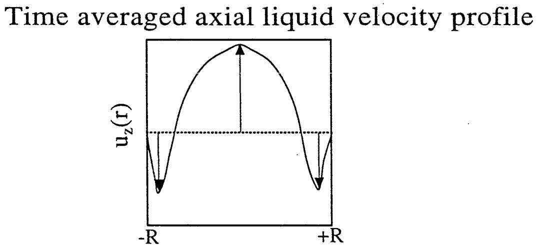

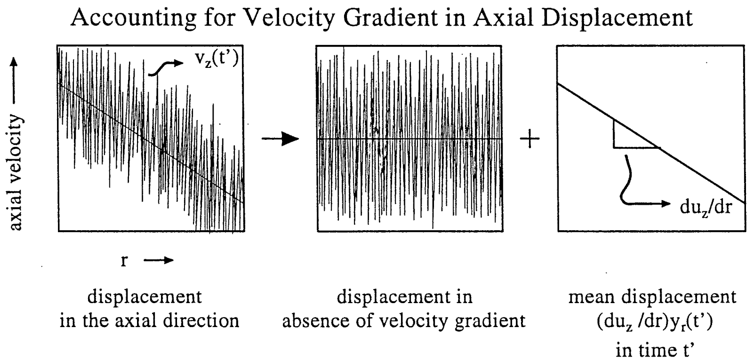

Figure 4.70: Flow Representation in Bubble Columns and Influence of Velocity Gradient on Fluctuating Velocity

$$y_z(t) = \int_0^t ((\frac{dU_z}{dr}\,|_{y_r(t')}\; y_r(t') + v'_z(t'))dt' \tag{4.20}$$

The velocity gradient is assigned the value corresponding to the compartment to which the particle belongs (depending on $y_r(t)$). Using the definition of the turbulent eddy diffusivity, D_{ij}, given by Equation 4.16, all the components of the eddy diffusivity are calculated.

The radial eddy diffusivity is:

$$D_{rr}(t) = \frac{1}{2}\frac{d}{dt}\overline{y_r^2}(t) = \int_0^t \overline{v'_r(t)v'_r(\tau)}d\tau \tag{4.21}$$

The azimuthal or tangential eddy diffusivity is:

$$D_{\theta\theta}(t) = \frac{1}{2}\frac{d}{dt}\overline{y_\theta^2}(t) = \int_0^t \overline{v'_\theta(t)v'_\theta(\tau)}d\tau \tag{4.22}$$

The axial eddy diffusivity is:

$$D_{zz}(t) = \frac{1}{2}\frac{d}{dt}\overline{y_z^2}(t) = \overline{y_z(t)v'_z(t)} \tag{4.23}$$

Using Equation 4.20, we get

$$D_{zz}(t) = \int_0^t \{\underbrace{\overline{\frac{\partial U_z}{\partial r}\,|_{y_r(t')}\,(\int_0^{t'} v'_z(t)v'_r(\tau)d\tau)}}_{term1} + \underbrace{\overline{v'_z(t)v'_z(t')}}_{term2}\}dt' \tag{4.24}$$

The above equations for the eddy diffusivities, are therefore related to the Lagrangian auto-correlation coefficient. In the present investigation the Lagrangian correlation coefficient is defined as

$$R_{ij}(\tau) = \overline{v'_i(t)v'_j(t+\tau)} \quad i,j \;=\; r,\ \theta,\ z \tag{4.25}$$

where i=j for the auto-correlation coefficient. The Lagrangian correlation coefficient, R_{ij}, defined above is related to the conventionally defined Lagrangian correlation coefficient, R'_{ij}, by the following equation:

$$R'_{ij}(\tau) = \frac{R_{ij}(\tau)}{\overline{v'_i(t)v'_j(t)}} \tag{4.26}$$

Therefore, from the classical standpoint the Lagrangian correlation coefficient is simply the non-dimensional representation of R_{ij}, with a maximum value of one. In order to understand the influence of the magnitude of the fluctuating velocities, the present analysis of CARPT data has been completely based on the Lagrangian correlation coefficient, R_{ij}, defined by Equation 4.25.

In a manner similar to that shown above, the other components of the eddy diffusivity, off the principle axis, D_{rz}, $D_{\theta r}$ and $D_{\theta z}$, can be calculated, which essentially involve the Lagrangian cross-correlation coefficients. The above equations are used along with Equations 3.17 and 3.18 (in Chapter 3), for evaluation of the various correlation coefficients from CARPT data, to compute the components of the eddy diffusivity tensor.

4.7.4 Lagrangian Correlation Coefficients

Results for the auto-correlation coefficients, R_{rr}, $R_{\theta\theta}$ and R_{zz}, and the cross-correlation coefficient R_{rz} in a 14 cm diameter column, using distributor **6A** at a superficial gas velocity of 12 cm/s are shown in Figures 4.71, 4.72, 4.73 and 4.74. The figures represent the data that have been averaged axially and azimuthally in the middle section of the column, since there is no significant variation of the data along the axial and azimuthal directions (within 10 to 15 %). The correlation coefficients are shown at various radial positions in the column.

Auto-correlation Coefficients

Figures 4.71, 4.72 and 4.73, for the auto-correlation coefficients, indicate that there is a significant radial variation of the auto-correlation coefficients, similar to the other fluid dynamic parameters. The auto-correlation at zero lag time, $\overline{v'^2}$, increases with increase in radial position, reaches a maximum close to the radial position of the flow inversion and then decreases once again, approaching the wall.

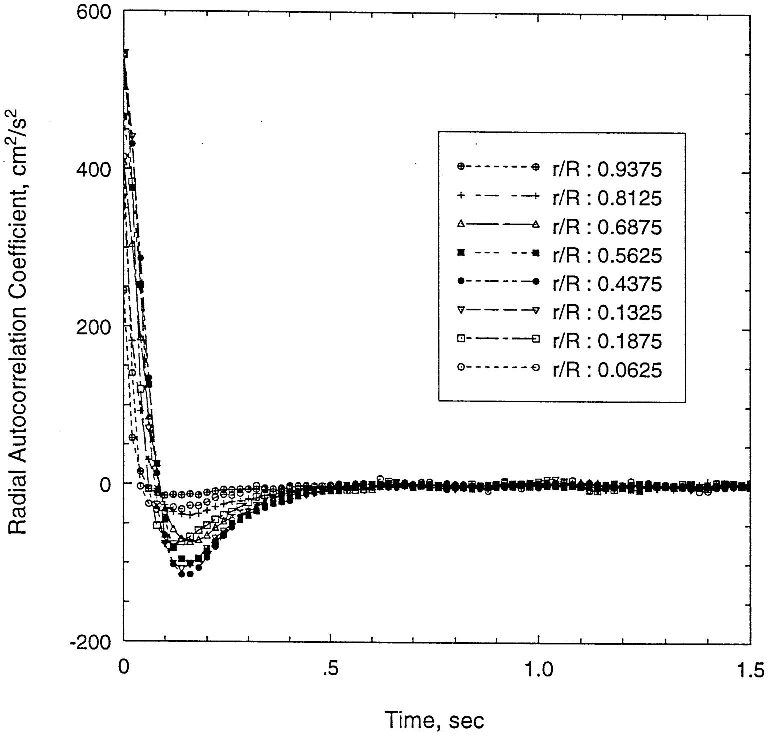

Figure 4.71: Radial Lagrangian Auto-correlation Coefficient at Various Radial Locations in the Middle Section of the Column, D_c: 14 cm, Distr.: **6A**, $U_g = 12$ cm/s

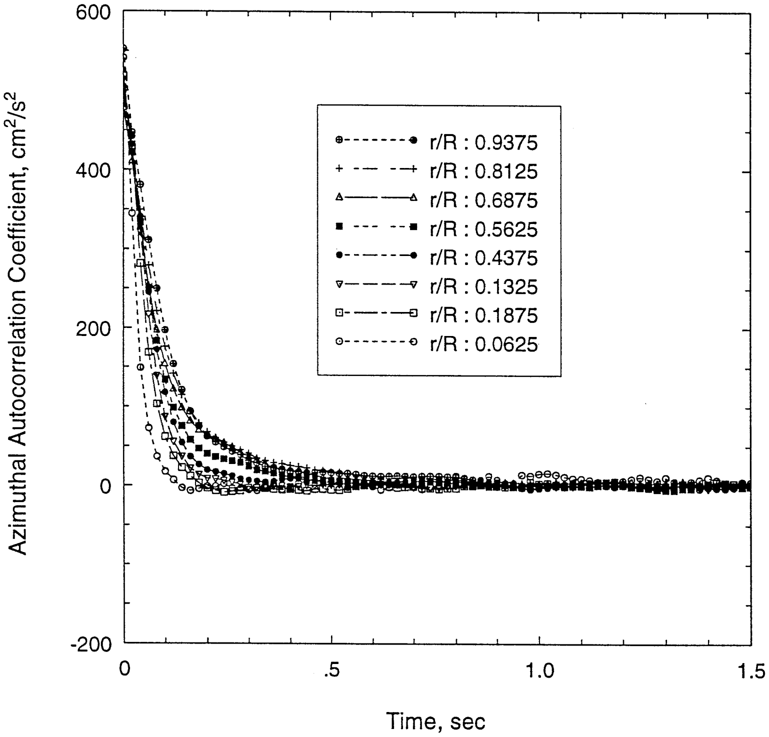

Figure 4.72: Azimuthal Lagrangian Auto-correlation Coefficient at Various Radial Locations in Middle Section of the Column, D_c: 14 cm, Distr.: **6A**, $U_g = 12$ cm/s

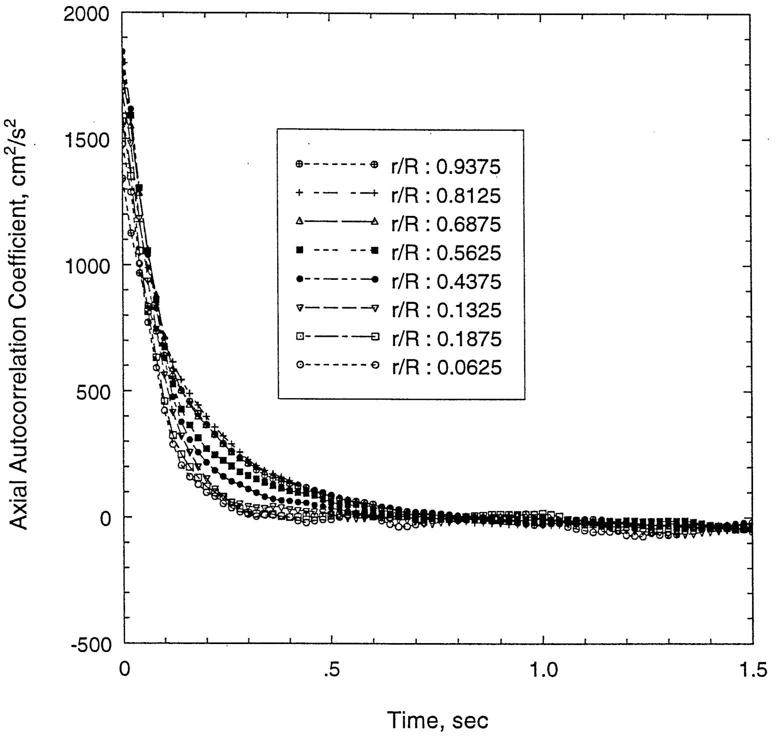

Figure 4.73: Axial Lagrangian Auto-correlation Coefficient at Various Radial Locations in the Middle Section of the Column, D_c: 14 cm, Distr.: **6A**, $U_g = 12$ cm/s

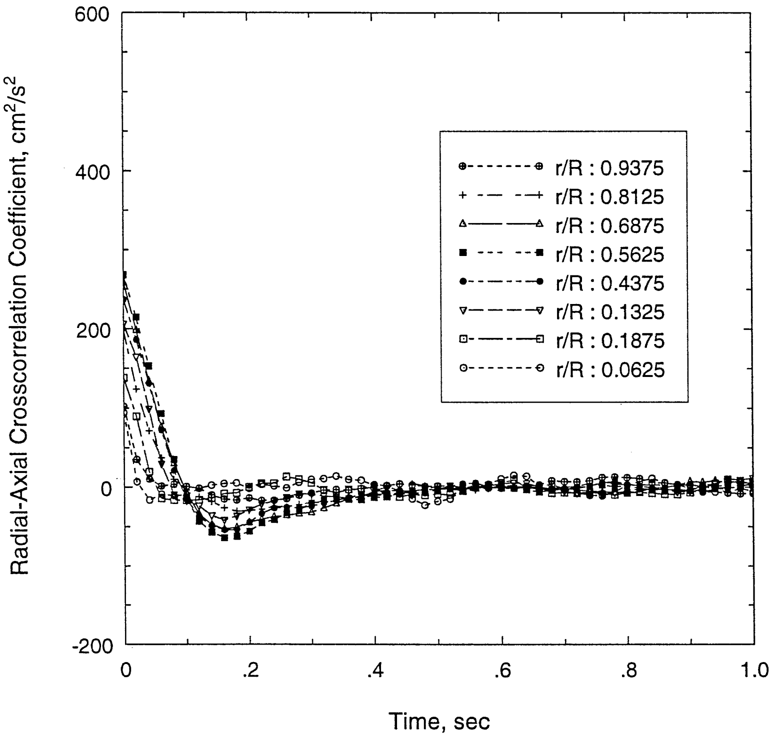

Figure 4.74: Radial-Axial Lagrangian Cross-correlation Coefficient at Various Radial Locations in Middle Section of the Column, D_c: 14 cm, Distr.: **6A**, $U_g = 12$ cm/s

This trend is most pronounced for the $\overline{v_z'^2}$. On the other hand, $\overline{v_\theta'^2}$ seems to have a maximum near the center and the wall, which coincides with the trends for the azimuthal normal stress measurements, $\overline{u_\theta'^2}$. Also, $\overline{v_z'^2}$ is much larger than both $\overline{v_r'^2}$ and $\overline{v_\theta'^2}$.

Another characteristic feature that can be calculated from the Lagrangian auto-correlation coefficient is the Lagrangian integral time scale, which is also referred to as the Lagrangian time macroscale. This parameter is defined as

$$\tau_{L,i} = \frac{\int_0^\infty \overline{v_i'(t)v_i'(t+t')}dt'}{\overline{v_i'^2}} \tag{4.27}$$

The Lagrangian integral time scale represents the time over which the fluid element is correlated with itself. In other words, it is the time in which the fluid element remains in an eddy, or the average time at the end of which it moves from one correlated region of flow to another. The earlier the auto-correlation drops to zero, the smaller is the Lagrangian integral time scale. The smaller the integral time scale, the sooner the fluid particle loses memory of its past, which reduces the extent of dispersion in the medium, since in the most simplified case (Equation 4.14) the eddy diffusivity is proportional to the product of the Lagrangian integral time scale and the mean square fluctuating velocity, $\overline{v'^2}$, or variance of the velocity fluctuation.

There are typically two types of functional forms that can be fitted to an auto-correlation coefficient. The first and most common type is the one which exhibits an exponential decay with time. In this case, the correlation coefficient gradually decreases, reaches zero and remains at zero. This is the type of correlation coefficient exhibited along the axial and azimuthal directions, $R_{zz}(t)$ and $R_{\theta\theta}(t)$. The other type is that which shows negative loops, before finally steadying at zero, similar to that observed from the present experiments for $R_{rr}(t)$. Such a functional form, with negative loops and oscillations, can be represented by the Frenkiel family of correlation functions defined as follows (Gouesbet et al. 1984):

$$R_L(\tau) = \exp[-\frac{\tau}{(m^2+1)\tau_L}]\cos[\frac{m\tau}{(m^2+1)\tau_L}] \qquad (4.28)$$

In the above expression, a value of m=0 leads to the first type of exponentially decaying correlation coefficients. The larger the value of m, the more pronounced are the overshoots and the greater the oscillations in the correlation coefficient.

The first type of correlation coefficients are commonly observed in homogeneous isotropic turbulence (Snyder and Lumley 1971) and represent a continuously increasing rate of dispersion with time. The second type of correlation functions have been commonly measured for heavy particles in turbulent gases (Mei et al. 1991). It is believed that heavy particles, due to their inertial effects tend to fall out of correlated flows or eddies quickly, since the inertia of the particle prevents it from following the high frequency fluctuations in the fluid (Yudine 1959; Csanady 1963). Therefore, an appreciable free fall velocity (settling velocity) causes the particle to fall successively from one correlated region to another. A thorough analysis of the effect of particle size and density on the behavior of particles in turbulent flows has been performed by Meek (1972). The relevant parts of his work were discussed in Chapter 3, while studying the ability of the CARPT tracer particle to follow the liquid. It was seen that the neutrally buoyant tracer closely follows the liquid motion for the large scale structures, i.e., high velocities and corresponding low frequencies, while for the small scale or high frequencies (low values of v_i') the particle will lose correlation and tend to fall out of an eddy faster than an actual fluid element.

In bubble column flows, especially at high gas velocities, there is intense turbulence due to interaction of the bubbles and the liquid, accompanied by liquid recirculation. Since there is no restriction in the column along the axial (longitudinal) direction, other than the dispersion height, the length scales of turbulence are much larger in the axial direction than along the radial direction. The particle fluctuating velocities are smaller in the radial direction than in the axial direction. In addition to the large axial scales, the gas bubbles as they rise up the column induce vortex like structures which result in large upward and downward liquid movement (gulf streaming). Since the radial and axial velocities are correlated (τ_{rz} and R_{rz}), a fluid particle, which is part of an eddy structure moving upward has the tendency to get caught in an adjacent down flowing structure, which causes the negative loops in the radial auto-correlation. The presence of the negative loops can hence be explained based on the flow pattern in bubble columns. Due to the relatively large size of the tracer particle being used, what is experienced by the tracer particle may be more pronounced than what is actually experienced by a fluid (water) element, since the particle cannot capture higher frequencies (greater than $\sim$ 30 Hz) of liquid motion. The negative loops are not observed in the axial auto-correlation since the axial eddy sizes are larger and dominate the radial scales and velocities. Interestingly enough, the azimuthal auto-correlation coefficient, $R_{\theta\theta}$, does not show any negative loops either. This can be reasoned since the tangential or azimuthal velocities are uncorrelated with the radial and axial velocities ($\tau_{r\theta}=\tau_{z\theta}=0$). Negative loops in R_{rr} have also been by Moslemian et al. (1992) in their measurements in a fluidized bed.

The integral time scale along the axial direction is therefore much larger than along the radial direction. While the time scales do vary with radial position, this variation is not very significant (20 %). Results for the time scales are therefore averaged radially and presented in Table 4.3. It is noted that the integral time scale decreases with increase in gas velocity, for a given column size, as shown in Table 4.3. This is expected and has been reported in single phase flow turbulence measurements (Snyder and Lumley 1971). As the gas velocity increases, the level of turbulence in the system also increases, which implies that the length scales increase. Larger eddies decay faster than smaller eddies, which are more persistent. This leads to the above mentioned dependence of the integral time scale on superficial gas velocity. However, the influence of column diameter on the integral time scales is not as significant (Table 4.3). Although, the time scale decreases with increase in gas velocity, the fluctuating velocity increases. Since the increase in the fluctuating velocity is much more pronounced, this yields ultimately in an increase in the eddy diffusivity, as shown in the following section.

Table 4.3: Column Averaged Lagrangian Integral Time Scales measured Using CARPT

D_c cm	Distr.	U_g cm/s	τ_{rL} sec	τ_{zL} sec
14.0	**6A**	2.4	0.0314	0.4140
		4.8	0.0173	0.1613
		9.6	0.0132	0.1224
		12.0 (Run 1)	0.0118	0.1166
		12.0 (Run 2)	0.0119	0.1156
14.0	**6B**	2.4	0.0171	0.2006
		4.8	0.0148	0.1668
		9.6	0.0125	0.1235
		12.0	0.0117	0.1118
19.0	**8B**	2.0	0.0375	0.3954
		5.0	0.0234	0.3362
		12.0	0.0134	0.1172
	8B	12.0	0.0118	0.1170
	8C	12.0	0.0125	0.1197
44.0	**18A**	2.0	0.0317	0.3948
		5.0	0.0181	0.2593
		10.0	0.0135	0.2026

Cross-correlation Coefficients

The cross-correlation coefficient R_{rz} in a 14 cm diameter column, using distributor **6A** at a superficial gas velocity of 12 cm/s is shown in Figure 4.74. In comparison with the auto-correlation coefficient, the cross-correlation is much smaller. However, when coupled with the mean radial gradient of the axial velocity, this term in Equation 4.24 will contribute to the overall axial eddy diffusivity. With regard to the D_{rz} term, however, the magnitude of R_{rz} results in small values of the eddy diffusivity, D_{rz}. The other two cross-correlation coefficients, $R_{r\theta}$ and $R_{z\theta}$ are found to be zero.

4.7.5 Turbulent Eddy Diffusivities

The turbulent eddy diffusivities are calculated according to Equations 4.21 to 4.24. As noted in these equations, in addition to being functions of position, the eddy diffusivities are functions of time as well. Depending on the nature of the auto-correlation coefficient the intermediate values of the eddy diffusivity may be greater or lower than the asymptotic value. For the case of the axial and azimuthal eddy diffusivities, due to an exponential decaying auto-correlation coefficient the intermediate values of the diffusivity are lower than the asymptotic value (Figure 4.76 and 4.77). On the other hand, since the radial auto-correlation coefficients show a negative loop, the radial eddy diffusivities at intermediate times are higher than their respective asymptotic values. This implies that along the radial direction the process of turbulent diffusion occurs in a transitory regime, i.e., it is predominant at intermediate times, rather than long times (Gouesbet et al. 1984). This is evident when examining Figure 4.75 for the radial eddy diffusivity as a function of time, as opposed to Figures 4.76 and 4.77 for the axial and azimuthal eddy diffusivity.

Analysis of such types of correlations have been made by Gouesbet et al. (1984) and others (Pismen and Nir 1978; Mei et al. 1991) in their work using Tchen's 1-D theory (Tchen 1947) of particle dispersion in the generalized modeling of the behavior of heavy particles in turbulent flows. In their analysis, Gouesbet et al. (1984) explain this phenomenon as the rate at which dispersion occurs depending on the cumulated 'memory' of the previous motions. The more the particles 'remember' in which direction they were previously moving, the faster they disperse. Negative correlations therefore lead to 'anti-memory' effects for the particles. Such a process would result in a 'pulsating' behavior of the probability density function of the fluid particle location in an isotropic and homogeneous turbulence field.

In bubble columns due to the highly complex nature of the flow field, and the large scale structures moving up and down the column, the existence of radial auto-correlations of the type shown in Figures 4.71, with negative loops, can be envisioned. As discussed in the previous section, the extent of these negative loops may be over pronounced due to the finite size of the particle. This implies that the asymptotic value of the radial eddy diffusivity as measured by the particle may be lower than that for an actual fluid element. However, for such complex flow fields as in bubble columns since the nature of the Lagrangian auto-correlation coefficients is not known, at this stage, this can not be conclusively verified.

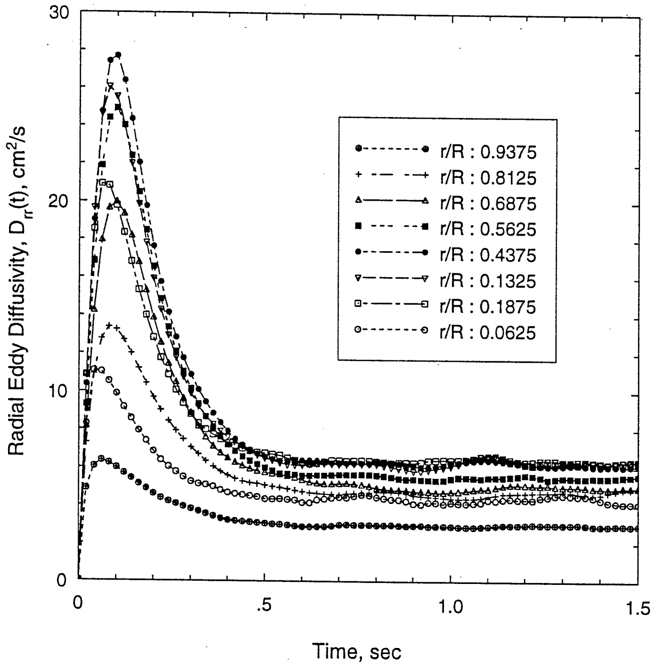

Figure 4.75: Radial Turbulent Diffusivity as a Function of Time at Various Radial Locations in Middle Section of the Column, D_c: 14 cm, Distr.: **6A**, U_g = 12 cm/s

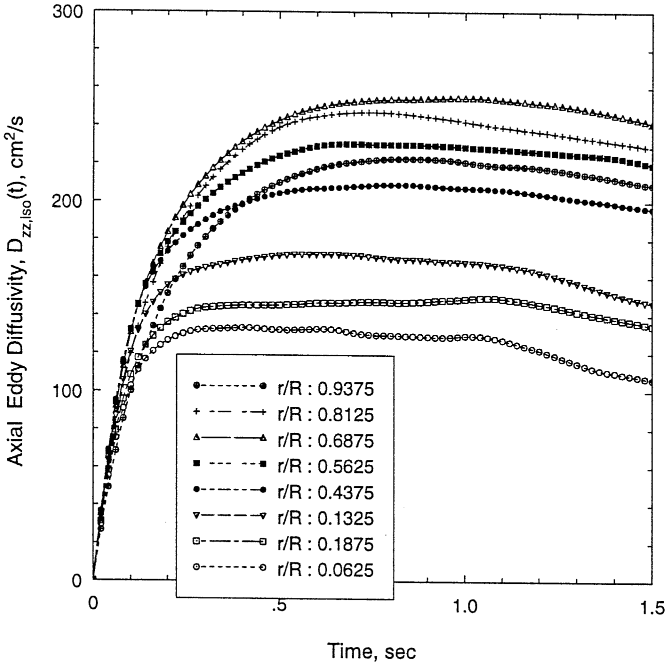

Figure 4.76: Axial Turbulent Diffusivity as a Function of Time at Various Radial Locations in Middle Section of the Column, D_c: 14 cm, Distr.: **6A**, U_g = 12 cm/s

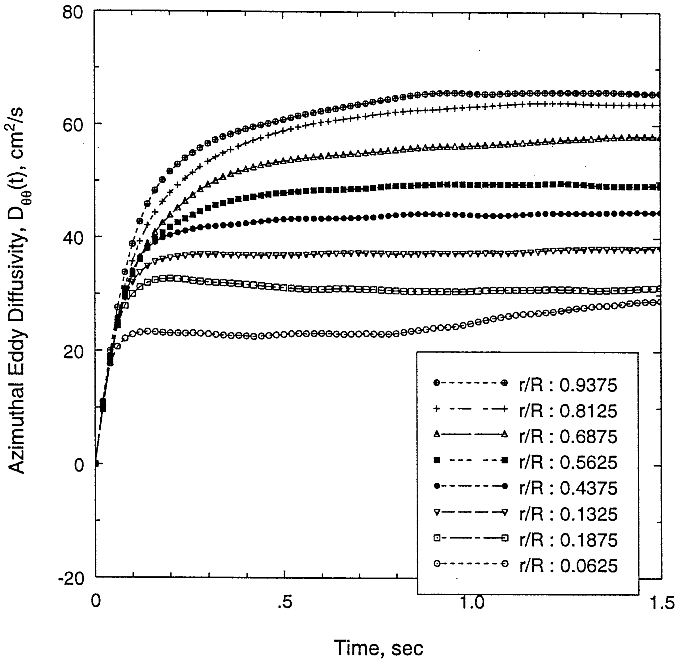

Figure 4.77: Azimuthal Turbulent Diffusivity as a Function of Time at Various Radial Locations in Middle Section of the Column, D_c: 14 cm, Distr.: **6A**, U_g = 12 cm/s

Although the eddy diffusivities are shown to be functions of time, for sake of analysis, a representative diffusivity is considered, along each direction. Along the axial and azimuthal directions, the maximum asymptotic value of the eddy diffusivities, which occur at large times, are considered. In the radial direction, the asymptotic value is smaller than the intermediate values of the eddy diffusivity (at small times). The maximum value is chosen to represent the radial eddy diffusivity (Gouesbet et al. 1984). Hereafter, for analysis of the effects of operating conditions as well as for the phenomenological modeling of liquid mixing, these values of the eddy diffusivities are considered.

The resulting radial, axial and azimuthal eddy diffusivities in a 14 cm diameter column at U_g = 12.0 cm/s, using distributor **6A**, are shown in Figures 4.78, 4.79 and 4.80. The bars denote the standard deviation of the local values (measured at a given (r,θ,z) compartment) from the azimuthally and axially averaged values. This variation is typical of most of the experimental conditions considered. Figure 4.79 for the axial eddy diffusivity shows that by including the effect caused by the presence of the mean velocity gradient and the cross-correlation R_{rz}, the resulting axial eddy diffusivity is about 20% lower than that evaluated using the assumptions of isotropic and homogeneous turbulence (term 2 of Equation 4.24). This is typical for all the cases, wherein the axial eddy diffusivity calculated by accounting for the existing flow conditions in bubble columns is anywhere between 10 to 25% lower than that calculated for isotropic homogeneous conditions. Therefore, it is important to account for the non-homogeneous conditions of the turbulence field, which becomes more pronounced at higher gas velocities and larger column diameters. This can be related to the observations made by Yang et al. (1992) who applied Hurst's analysis to CARPT data and showed persistent long-term effects along the axial direction, which was supposed to be caused by the recirculating behavior of the flow in bubble columns.

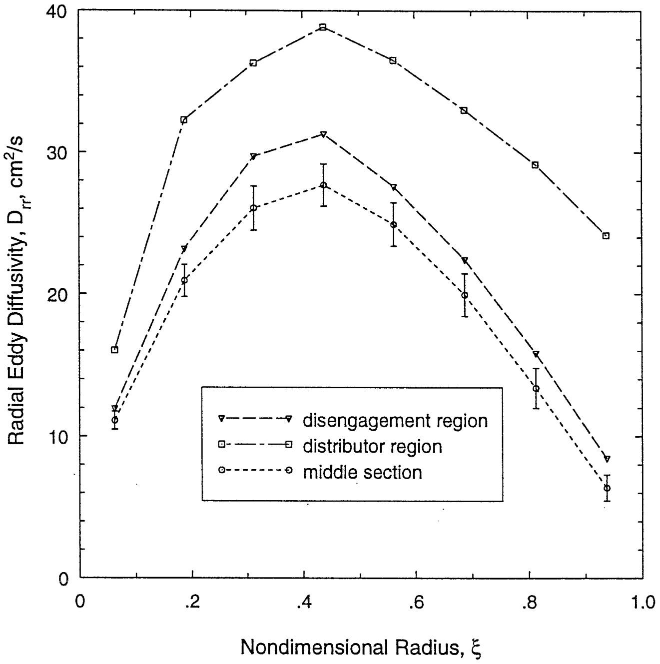

Figure 4.78: Radial Turbulent Eddy Diffusivity as a Function of Radial Position, D_c: 14 cm, Distr.: **6A**, U_g = 12 cm/s

The diffusivities are higher near the distributor region, where the level of turbulence is higher. The azimuthal eddy diffusivities are larger than the radial eddy diffusivities (by about two times) indicating that mixing in the angular direction is faster than in the radial direction. Both the radial and azimuthal eddy diffusivities are much lower than the axial eddy diffusivities (by almost an order of magnitude), which is similar to the results for the normal stress measurements.

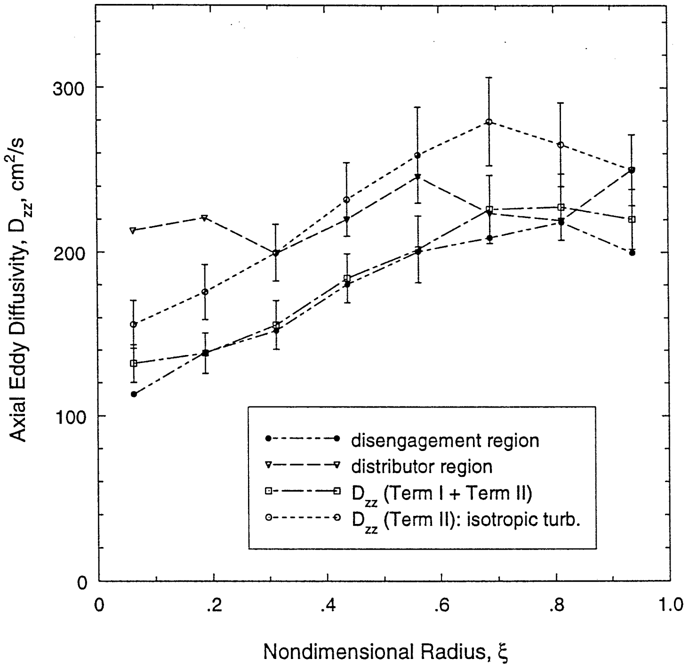

Figure 4.79: Axial Turbulent Eddy Diffusivity as a Function of Radial Position, D_c: 14 cm, Distr.: **6A**, U_g = 12 cm/s

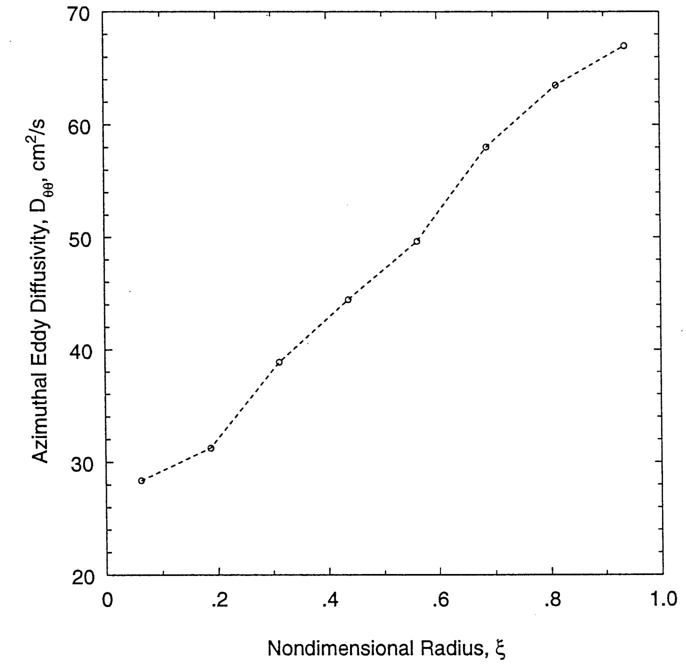

Figure 4.80: Azimuthal Turbulent Eddy Diffusivity as a Function of Radial Position, D_c: 14 cm, Distr.: **6A**, U_g = 12 cm/s

The diffusivity, D_{rz}, calculated using the cross-correlation coefficient is found to be very low, with an average value which is 5 % of D_{rr}. For the purpose of modeling (in Chapter 6) this term can be neglected. Of course, based on the other cross-correlation terms, $R_{\theta r}$ and $R_{\theta z}$, the two off-diagonal components of the diffusivity tensor, i.e., $D_{r\theta}$ and $D_{z\theta}$ are zero. A typical eddy diffusivity tensor for the cross sectional averaged eddy diffusivities in a 14 cm column (distributor **6A**, $U_g = 12$ cm/s) is

$$D_{ij} = \begin{pmatrix} D_{rr} & D_{\theta r} & D_{zr} \\ D_{r\theta} & D_{\theta\theta} & D_{z\theta} \\ D_{rz} & D_{\theta z} & D_{zz} \end{pmatrix} \tag{4.29}$$

$$= \begin{pmatrix} 18.1 & 0.0 & 1.2 \\ 0.0 & 54.1 & 0.0 \\ 1.2 & 0.0 & 204.7 \end{pmatrix} \qquad (\mathrm{cm}^2/\mathrm{s})$$

The main objective of evaluating the Lagrangian turbulent eddy diffusivities using the CARPT technique, is to determine whether these diffusivities can serve in the closure of the $\overline{u_i'C'}$ terms that appear in the tracer species balance equation for the liquid phase, for modeling liquid mixing in bubble columns, using the gradient diffusion model. While this type of model is a standard method of closure for the correlation of various fluctuating quantities, the evaluation of the diffusivity and viscosity terms is usually done by resorting to further modeling (one equation or two equations models) or some form of empiricism. Since with the CARPT technique it is possible to measure the Lagrangian eddy diffusivities, these measurements are used for closure modeling, as described in Chapter 6. From the point of view of modeling since the proposed model is two dimensional, only the radial and axial eddy diffusivities are further analyzed.

Figures 4.81 and 4.82 show the effect of gas velocity and column diameter on the axially averaged radial profiles of the radial and axial turbulent eddy diffusivities. Both the radial and axial eddy diffusivities increase with increase in column diameter and gas velocity. The effects of gas superficial velocity on eddy diffusivities is similar to that of the other turbulence parameters (e.g., turbulent kinetic energy), in that there is a pronounced increase in the diffusivities when moving from the bubbly flow regime to the churn-turbulent regime. This can be clearly seen in the 14 cm diameter column, when comparing the changes in the diffusivities with increasing gas velocity. It is expected that with further increase in gas velocity, the diffusivities will tend to level off, similar to the behavior of the other fluid dynamic parameters. Additional details regarding the dependency of the column averaged radial and axial eddy diffusivities are given in the next chapter, which discusses the effects of scale.

4.7.6 Turbulent Length Scales

Based on a simplified representation, it was seen in the previous sections that the turbulent eddy diffusivity can be approximately expressed in terms of the integral time scale and the mean square of the fluctuating Lagrangian velocity. Another form of expression that is sometimes adopted (e.g. Franz et al. 1984) is to approximate the eddy diffusivity as the product of a turbulent length scale and a fluctuating velocity (*rms* velocity). Both the eddy diffusivity and *rms* velocity are obtained as part of the present measurements. Hence it is possible to determine turbulent length scales from the following equations:

$$l_z = \frac{D_{zz}}{\sqrt{\overline{v_z'^2}}} \tag{4.30}$$

$$l_r = \frac{D_{rr}}{\sqrt{\overline{v_r'^2}}} \tag{4.31}$$

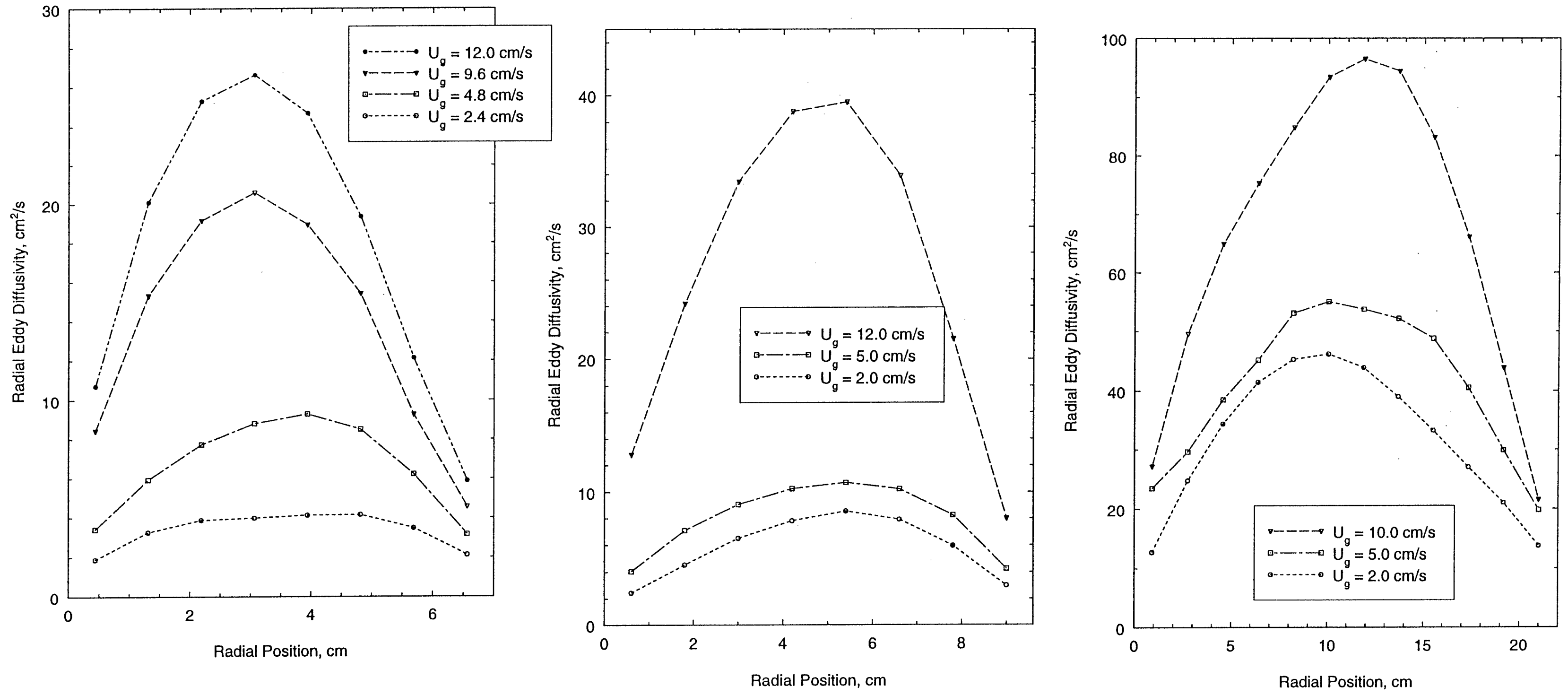

(a)

(b)

(c)

Figure 4.81: Effect of Superficial Gas Velocity on the One Dimensional Radial Eddy Diffusivities (a) Col. Dia. = 14 cm (**6A**) (b) Col. Dia. = 19 cm (**8A**) (c) Col. Dia. = 44 cm

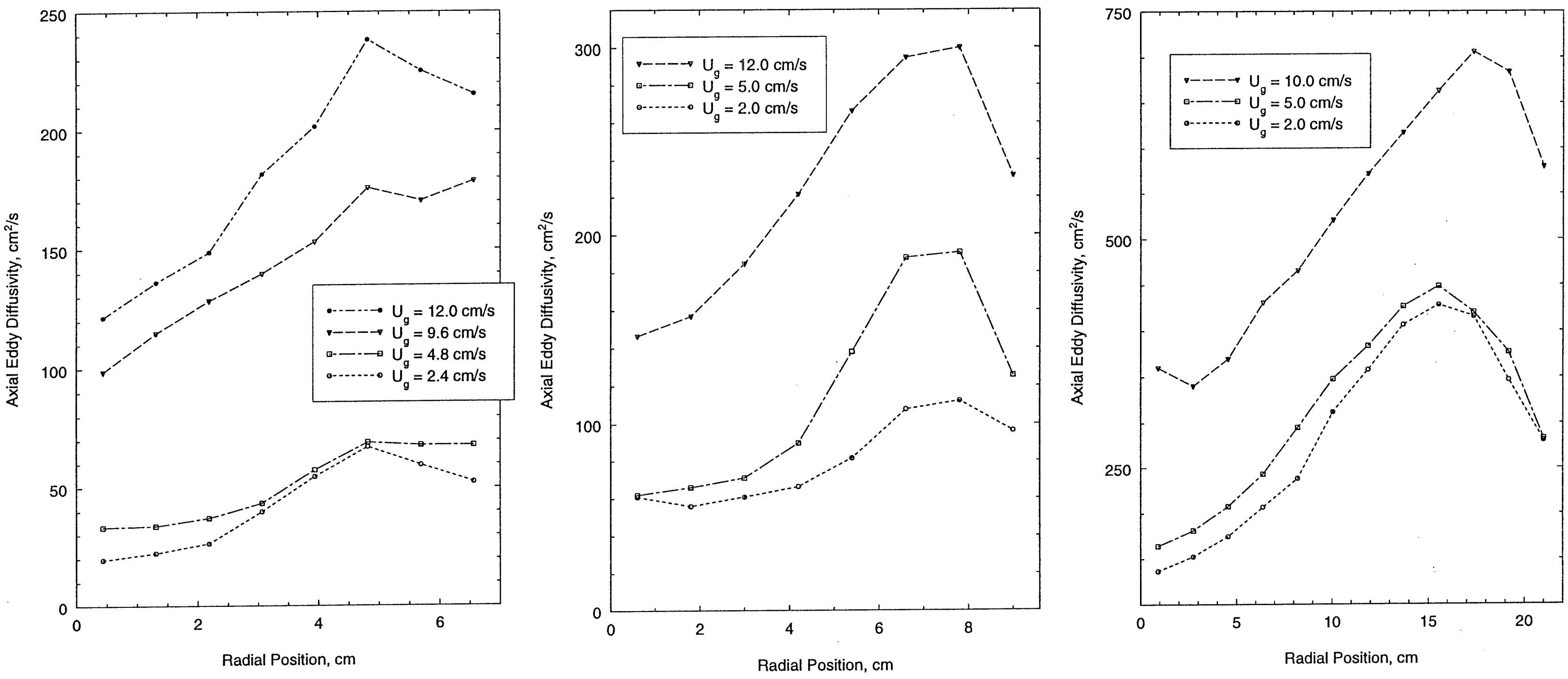

(a) (b) (c)

Figure 4.82: Effect of Superficial Gas Velocity on the One Dimensional Axial Eddy Diffusivities (a) Col. Dia. = 14 cm (**6A**) (b) Col. Dia. = 19 cm (**8A**) (c) Col. Dia. = 44 cm

The above expressions result in radial profiles for l_z and l_r. Using these equations along with CARPT data, the henceforth evaluated radial and axial turbulent length scales exhibit the same trends of radial dependency as the radial and axial turbulent eddy diffusivities, respectively. This is since the radial variation of the *rms* velocities relative to that for eddy diffusivities is low. The radial turbulent length scale is of the order of 1 cm for a 14 cm diameter column, while the axial length scale is of the order of the column radius, 7 cm. These length scales hence differ from the Prandtl's mixing length profiles that are calculated in the gradient closure model for describing the Reynolds shear stress terms, which show a maximum near the center of the column.

4.7.7 Summary

CARPT experimental data has been used to evaluate the Lagrangian statistics in bubble columns. The calculated Lagrangian auto-correlation coefficients show a strong dependency on radial position in the column, with a maximum near the position of flow inversion. The auto-correlation coefficient in the axial direction is much higher (2 to 3 times) than that in the radial and azimuthal directions. While the axial and azimuthal auto-correlation coefficients exhibit a steady decay with time finally reaching zero, the radial auto-correlation coefficient contains negative loops. This is explained as being due to the nature of the flow in bubble columns. The cross-correlation, R_{rz} is non-zero but much smaller than the auto-correlation coefficients. The other cross-correlations coefficients, $R_{\theta z}$ and $R_{\theta r}$ are zero.

The non-homogeneous nature of the flow has been properly accounted for in evaluating the turbulent eddy diffusivities. The existence of a non-zero gradient, $\frac{du_z}{dr}$ and cross-correlation coefficient R_{rz} results in a decrease of a maximum of 25 % in the axial eddy diffusivity when compared with that obtained under homogeneous conditions. The radial and azimuthal diffusivities are unaffected. The axial eddy diffusivities are an order of magnitude larger than the radial eddy diffusivities, pointing to the highly non-isotropic nature of the flow. The diffusivity, D_{rz}, is about 5 % of the radial eddy diffusivity, which is considered to be negligible. Furthermore $D_{\theta r}$ and $D_{\theta z}$ are zero (due to zero cross-correlation coefficients). The axial and radial diffusivities strongly vary with radial position. As with the other fluid dynamic parameters, their variation with axial and azimuthal position in the middle section of the column is negligible. The eddy diffusivities in the distributor region are higher than in the middle section of the column.

The eddy diffusivities increase with increase in gas velocity. The Lagrangian integral time scales are found to decrease with increase in gas velocity, which is expected, and are almost independent of column diameter. The integral time scales in the radial direction are an order of magnitude smaller than in the axial direction. The eddy diffusivities measured in this work using CARPT are used in the modeling of liquid mixing in bubble columns.